

AN ADAPTIVE MULTI-SCALE COMPUTATIONAL METHOD FOR MODELING
NONLINEAR DEFORMATION IN NANOSCALE MATERIALS

A Dissertation

Submitted to the Graduate Faculty of the
Louisiana State University and
Agriculture and Mechanical College
in partial fulfillment of the
requirements for the degree of
Doctor of Philosophy

in

The Department of Civil and Environmental Engineering

by
Wenming Wang
B.S., Zhejiang University, 1995
M.S., Tsinghua University, 1998
December 2006

Acknowledgments

First, I would like to thank my advisor Dr. Moorthy for his mentorship. I sincerely appreciate his encouragement, patience, and inspiration over the years which made this dissertation possible. I also would like to thank Dr. Voyiadjis, Dr. Boudin, and Dr. Meng for their guidance. I especially thank my parents for their continuing support throughout my studies away from home.

Table of Contents

| | |
|----------------------------------------------------------------------------------|-------------|
| Acknowledgments | ii |
| List of Tables | v |
| List of Figures | vii |
| Abstract | viii |
| Chapter 1 Introduction | 1 |
| 1.1 Atomistic Modeling | 3 |
| 1.2 Continuum Modeling | 4 |
| 1.3 Multi-scale Modeling | 5 |
| 1.4 Adaptive Finite Element Methods | 8 |
| 1.5 Interatomic Potentials | 9 |
| 1.6 Nanoindentation | 10 |
| Chapter 2 Adaptive Finite Element Method for Continuum Modeling | 12 |
| 2.1 Introduction | 12 |
| 2.2 Overview of the Finite Element Method for Structural Problems | 12 |
| 2.2.1 Strong Form of the Problem | 13 |
| 2.2.2 Weak or Variational Statement | 13 |
| 2.2.3 Galerkin Formulation | 14 |
| 2.3 Isoparametric Elements | 16 |
| 2.3.1 Bilinear Quadrilateral Element(Q4) | 16 |
| 2.3.2 Trilinear Hexahedral Element(H8) | 17 |
| 2.3.3 Numerical Integration Using Gaussian Quadrature | 19 |
| 2.4 Solution to the Finite Element Equations | 19 |
| 2.5 Recovery Based Aposteriori Error Estimate | 20 |
| 2.5.1 Global Smoothing | 20 |
| 2.5.2 ZZ Error Estimate | 21 |
| 2.5.3 Mesh Refinement Strategies | 22 |
| 2.6 Refinement | 22 |
| 2.6.1 2D Refining | 23 |
| 2.6.2 3D Refining | 31 |

| | |
|-------------------------------------------------------------------------------------|-----------|
| Chapter 3 Atomistic Calculation of Potentials for Coarse/Fine Scale Problems | 42 |
| 3.1 Introduction | 42 |
| 3.2 Inter-atomic Potentials | 43 |
| 3.2.1 Interpolation and Extrapolation of Interatomic Potentials for Al | 43 |
| 3.3 Continuum Mechanics/Local Quasi-Continuum | 46 |
| 3.3.1 Deformation Gradient and Large Deformation | 48 |
| 3.3.2 Energy Density Functional | 48 |
| 3.4 Fully Atomistic/Nonlocal QC | 51 |
| 3.4.1 Energy-based Formulation | 52 |
| 3.4.2 Force-based Formulation | 52 |
| 3.5 Coupled Atomistic/Continuum Methods | 54 |
| 3.5.1 Local QC and Energy-based Methods | 54 |
| 3.5.2 Local QC and Forced-based Methods | 57 |
| 3.6 The Effect of Finite Temperature | 59 |
| 3.6.1 Local Harmonic Approximation of Finite Temperature Effects | 59 |
| | |
| Chapter 4 Nanoindentation Problems at Finite Temperatures | 67 |
| 4.1 Introduction | 67 |
| 4.2 Contact Algorithm for Indentation Problem | 68 |
| 4.2.1 Perturbed Lagrange Formulation | 69 |
| 4.3 Applications to Nanoindentation Simulations | 71 |
| 4.3.1 Deformation in Out-of-plane Direction | 71 |
| 4.3.2 2D Cylindrical Indenter | 72 |
| 4.3.3 Effect of Temperature due to Nanoindentation of a 2D Flat Indenter | 76 |
| 4.3.4 Nanoindentation with a Spherical Indenter | 78 |
| | |
| Chapter 5 Conclusions and Future Work | 84 |
| | |
| Bibliography | 85 |
| | |
| Vita | 93 |

List of Tables

| | | |
|-----|-----------------------------------------------------------------|----|
| 2.1 | Array for sides used to describe $2d$ mesh refinement | 27 |
| 3.1 | Tabulated potential functions for Al and Ni from [62] | 46 |

List of Figures

| | | |
|------|------------------------------------------------------------------------------------------------------------------------------------------------------------------------------------------------------------------------------------------------------------------|----|
| 2.1 | Isoparametric mapping from physical to reference coordinates for a (a) $2d$ and (b) $3d$ finite element | 15 |
| 2.2 | A Q4 element refined to four Q4 elements | 23 |
| 2.3 | Refining of one level | 27 |
| 2.4 | Series of mesh refinements generated by adaptive strategy | 31 |
| 2.5 | Evolution of strain energy error indicator for a sample $2d$ problem | 32 |
| 2.6 | Convergence of first Piola-Kirchoff stress T_{22} (in Pa) for the sample $2D$ problem | 33 |
| 2.7 | Meshes of three levels refinement for different strain energy error indicator cutoff: 2%(left) and 0.5%(right) | 34 |
| 2.8 | First Piola-Kirchoff stress T_{22} (in Pa) for different strain energy error indicator cutoff: 2%(left) and 0.5%(right) | 34 |
| 2.9 | Series of mesh refinements generated by adaptive strategy with irregular initial mesh | 35 |
| 2.10 | Convergence of first Piola-Kirchoff stress T_{22} (in Pa) with irregular initial mesh | 36 |
| 2.11 | A H8 element refined to eight H8 elements | 37 |
| 2.12 | Automatic adaption process in three dimension refining | 38 |
| 2.13 | Convergence of first piola-Kirchoff stress T_{33} (in Pa) for the sample $3d$ problem | 39 |
| 2.14 | Automatic adaption process in three dimension refining with irregular initial mesh | 40 |
| 2.15 | Convergence of first Piola-Kirchoff stress T_{33} (in Pa) with irregular initial mesh | 41 |
| 3.1 | Pair potential functions for Al.(a) $V[\text{eV}]$ vs $r[\text{\AA}]$. (b) dV/dr [$\text{eV}/\text{\AA}$] vs $r[\text{\AA}]$. (c) d^2V/dr^2 [$\text{eV}/\text{\AA}^2$] vs $r[\text{\AA}]$ | 44 |
| 3.2 | Atomic density functions for Al.(a) $\rho[\text{unit}]$ vs $r[\text{\AA}]$. (b) $d\rho/dr$ [$\text{unit}/\text{\AA}$] vs $r[\text{\AA}]$. (c) $d^2\rho/dr^2$ [$\text{unit}/\text{\AA}^2$] vs $r[\text{\AA}]$ | 45 |
| 3.3 | Embedding energy functions for Al. (a) $F[\text{eV}]$ vs $\bar{\rho}[\text{unit}]$. (b) $dF/d\bar{\rho}$ [eV/unit] vs $\bar{\rho}[\text{unit}]$. (c) $d^2F/d\bar{\rho}^2$ [eV/unit] vs $\bar{\rho}[\text{unit}]$ | 47 |

| | | |
|------|---------------------------------------------------------------------------------------------------------------------------------------------------|----|
| 3.4 | Illustration of Cauchy-Born rule which maps \mathbf{A}_i into $\boldsymbol{\alpha}_i$ | 48 |
| 3.5 | The atomistic/continuum transition region for the QC method | 55 |
| 3.6 | Effect of temperature on the lattice parameter of single crystal aluminum | 63 |
| 4.1 | Schematic of the computational model used in a nanoindentation experiment | 67 |
| 4.2 | Nanoindentation in an aluminum single crystal with cylindrical indenter | 73 |
| 4.3 | Automatic multi-scale mesh refinement generated for nanoindentation problem in figure 4.2 | 74 |
| 4.4 | Atomic structure under indenter, just before nucleation of first defect, for nanoindentation problem in figure 4.2 | 74 |
| 4.5 | Atomic structure under indenter, just before nucleation of first defect, for nanoindentation problem in figure 4.2, a close look | 75 |
| 4.6 | Stress T_{yy} (in Pa) just before first dislocation for nanoindentation problem in figure 4.2 | 76 |
| 4.7 | Load vs indenter displacement for nanoindentation problem in figure 4.2 | 76 |
| 4.8 | Load vs contact half-width for nanoindentation problem in figure 4.2 | 77 |
| 4.9 | Nanoindentation in an aluminum single crystal | 77 |
| 4.10 | Automatic multi-scale mesh refinement generated for nanoindentation problem in figure 4.9 | 79 |
| 4.11 | Atomic structure under indenter, just before nucleation of first defect, for nanoindentation problem (temperature: 0 K) in figure 4.9 | 79 |
| 4.12 | Atomic structure under indenter, just before nucleation of first defect, for nanoindentation problem (temperature: 293 K) in figure 4.9 | 80 |
| 4.13 | Atomic structure under indenter, just before nucleation of first defect, for nanoindentation problem (temperature: 373 K) in figure 4.9 | 80 |
| 4.14 | Load vs indenter displacement at different temperature for nanoindentation problem in figure 4.9 | 81 |
| 4.15 | Stress T_{yy} (in Pa) just before first dislocation for nanoindentation problem in figure 4.9 at $T = 373K$ | 81 |
| 4.16 | Geometry of the computational cell and initial mesh | 82 |
| 4.17 | Cross section of the computational mesh at an indentation depth of 210.5 Å | 82 |
| 4.18 | Stress T_{zz} (in Pa) at an indentation depth of 210.5 Å | 83 |
| 4.19 | Force vs displacement curve for the 4700 Å-radius indenter | 83 |

Abstract

In this dissertation a coupled multi-scale computational model for simulating nonlinear deformation processes in crystalline metals at finite temperatures is developed. The computational model uses the finite element method to model the coarse scale response of the material. The constitutive response in the finite element will be modeled through interatomic potentials acting on the underlying homogeneous crystal lattice that characterizes its nanostructure. An adaptive remeshing technique is proposed to automatically delineate regions of severe deformation where homogeneity of the microstructure/deformation is violated. In these regions the finite element will be replaced by a set of deformed atoms which interact with each other through the interatomic potential. The resulting coupled multi-scale model will be used to study defect generation and growth, through a computational nanoindentation experiment, in practical $2D$ and $3D$ problems.

Chapter 1

Introduction

The traditional analytical framework in engineering mechanics has been that of a *continuum*. Materials are assumed to be comprised of a collection of infinitely divisible continuum elements. The continuum assumption therefore implies that the underlying material response remains unchanged regardless of the scale of action. However, the mechanical deformation and failure of many engineering materials are inherently multi-scale. The observed homogeneous macroscopic (continuum scale) behavior of the material is governed by physical processes that occur at a heterogeneous microscopic fine scale. For example, most metals at the macroscale ($\approx \mathcal{O}(mm)$) are composed of a polycrystalline aggregate of heterogeneous grains ($\approx \mathcal{O}(\mu m)$) at the fine scale. The resulting ductile macroscopic material behavior of the homogeneous metal is dependent upon heterogeneous physical interactions of dislocations in the microscale grain boundaries [5]. The generation of dislocations in the microscale single grain of the metal may itself be dependent upon the heterogeneous interactions between defects with a lattice of metal atoms at the finer nanoscale ($\approx \mathcal{O}(nm)$) [18]. With the advent of manufacturing processes for nano-structured materials, in the form of micro-electromechanical system (MEMS) devices, it has become extremely important to understand the physical processes that govern the interaction between these disparate length scales.

MEMS are devices containing extremely small mechanical components with integrated electrical circuitry. They are used to produce a range of products including micro sensors/actuators used to monitor mechanical properties such as pressure/motion in physical systems, microfluidic systems that can be used for the noninvasive drug delivery, and diagnosis in biological systems and low voltage switches/capacitors/inductors used in electrical/electronic systems. Sizes of MEMS can range anywhere from *mms-nms*. The extreme level of miniaturization used to design these systems requires a proper understanding of the physical behavior of materials used to produce them. An important class of materials used in the manufacture of MEMS are nanocomposites. They are composed of dissimilar materials that are mixed together in the atomistic scales to produce enhanced mechanical/electrical properties. Some of the mechanical properties that could be enhanced include improved hardness in microseals using metal/ceramic nanocomposites [73, 59] and increased strength using carbon nanotube enhanced polymer composites [50]. The process of mixing materials at the nanoscale requires the understanding of physical processes that link the deformation at the nanoscale to mechanical properties at the microscale. In these materials, damage/deformation at the crystalline mesoscale (size of a single grain) is directly affected by the underlying failure mechanisms of the heterogeneous metal atoms at the

atomistic scales. Of particular interest is the development of defects at the atomistic scale and their effect on the nonlinear mechanical properties of the crystalline mesoscale material.

Over the past three decades, many new tools and techniques have been created to synthesize nanoscale objects and to learn their incredible properties. Today's high-resolution electron microscopy can distinguish individual atoms, making manipulation of atoms, one at a time, possible. Such nanoscale materials find wide application in areas such as drug delivery, material reinforcement, field emission panel display, nanoelectronics and tailor-designed materials [73, 59, 40]. In most of these cases, nanoscale materials will be used in conjunction with components that have different length and time scales. At the smallest length scale of angstroms ($10\text{\AA} = 1\text{nm}$), quantum mechanical interaction and atomic structure provide an underlying framework for the formation of a wide variety of defects in crystalline solids. The deformation fields associated with nm -scale defects, such as dislocations, lead to defect interaction at even larger scales such as dislocation patterning. Single scale methods such as 'ab initio' quantum mechanical methods or molecular dynamics (MD) will have difficulty in analyzing such hybrid structures due to the inherent limitations in terms of the time and length scales assumptions of these methods. In order to study such nanoscale materials, it is therefore essential to model up to a scale of several microns (consisting of billions of atoms) which is too large for pure MD simulations. Thus fully atomistic simulation of the nucleation and flow of dislocations remains a computational challenge. It is apparent that with a large number of atoms in a fully atomistic model, substantial regions of the problem are essentially behaving like a continuum. It is therefore apparent that while fully atomistic calculations are essential to our understanding of the basic deformation processes, they can be replaced by continuum models along regions of smoother deformation behavior. Consequently, over the last few years, researchers in materials science, engineering mechanics and mathematical physics have also shown considerable interest in the computational multiple length-scale modeling of deformation/damage in such nanoscale materials [79, 63, 90]. The basic idea in coupled methods is to use a fully atomistic description in regions of the material undergoing severe deformation and to use a continuum description in less severe regions. The quasi-continuum method (QC) is one such mixed atomistic-continuum formulation. It is based on a finite element discretization of the continuum domain with coupled atomistic simulation of the microscale response. Thus the finite element method serves as the numerical engine for determining the energy minimizing mesoscale displacement fields, while the atomistic analysis is used to determine the onset of permanent deformation in the nanoscale configuration. This is in contrast to standard finite element approaches, where the constitutive input for deformation and damage is made via phenomenological models. As the material deforms under the action of external forces, the size of the finite element required to model material deformation becomes progressively smaller. As the element size approaches that of the underlying lattice dimension, there is a breakdown of the continuum assumption. In the QC method, an adaptive remeshing technique automatically delineates this region of severe deformation and replaces it with a full blown atomistic simulation of the deformation of the lattice sites that make up the nanostructure. Such computational models provide an efficient and accurate methodology that can be used to gain invaluable insights into physical phenomena involved in the design of such materials.

In the dissertation, the underlying ductile material behavior of metals will be studied through a multi-scale computational model. The proposed model will be used to study defect forma-

tion and growth through a computational nano-indentation experiment in the material at finite temperatures. The resulting computational model will provide an effective framework to analyze deformation in more complex materials such as heterogeneous nanocomposites undergoing complex loading processes.

1.1 Atomistic Modeling

In an atomistic model, the crystalline solid is described explicitly as a collection of atoms occupying lattice sites in space. The initial undeformed coordinates of the atoms is transformed so as to maintain equilibrium in the final deformed configuration under the application of external forces, specified through boundary conditions. Depending on the kind of equilibrium achieved, atomistic simulations fall into two broad classifications, namely static and dynamic models. In the former, lattice statics (*LS*) is usually carried out at zero temperature and any loads are assumed to be quasistatic and the atomic level response is obtained by the minimization of total potential energy of the system. In the latter dynamic case, atomic motion is governed by direct integration of Newton’s second law and is referred to as molecular dynamics (*MD*). The resulting equilibrium configurations include atom vibration about lattice sites and can therefore be thought of as descriptive of a thermodynamic continuum scale temperature in the material.

MD was first used in physical chemistry and thermodynamics. MD was used to obtain the average thermochemical properties of various physical systems such as gases, liquids, and solids. It has been applied to simulate the instantaneous behavior of different material systems [77, 76, 39]. The two basic assumptions in standard *MD* simulations are [76]:

1. The system is modeled as a collection of interacting molecules or atoms, which dynamically move with a vector of instantaneous positions and velocities. The atomic interaction has a strong dependence on the spatial orientation and distribution of separate atoms.
2. The number of atoms and the mass of each atom do not change during the modeling process.

The MD system is usually modeled as an isolated system whose energy remains conserved during the computational experiment. Non-conservative techniques are also available which model the dissipation of the kinetic energy into the surrounding media. The governing equations for *MD* simulations is a straightforward second-order ODE.

$$m_i \ddot{\mathbf{r}}_i = - \frac{\partial U(\mathbf{r}_1, \mathbf{r}_2, \dots)}{\partial \mathbf{r}_i} \equiv \mathbf{F}_i, i = 1, 2 \dots N \quad (1.1)$$

Here, \mathbf{r}_i is the position vector of atom i , N is the total number of simulated atoms, m_i is the mass of atom i , U is the potential function of the atomic coordinates. The force \mathbf{F}_i , acting on atom i , is usually referred to as the *internal* force. The equation (1.1) are solved for a given set of initial conditions to get trajectories of the atomic motion in the simulated system. The alternative Hamiltonian formulation, in terms of generalized coordinates and momentum, is also available to study the response of a collection of atoms [76]. The resulting Lagrangian formulation provides a series of advantages related to the mathematical stability of the resulting computational model, but in all cases is theoretically equivalent to the system generated by

Newton’s laws of motion. Consequently the stable Hamiltonian formulation is typically used in describing the state and evolution of many-particle systems in *MD* simulations. In either formulations, the major task of the *MD* simulation is to predict the time-dependent trajectories in a system of interacting particles. For this purpose, time-integration algorithms were devised to solve the equations of motion (1.1) based upon truncated Taylor’s expansions with respect to time [76].

MD simulations provide the position of every atom in the simulation at every time during the evolution, and consequently it is possible to identify and elucidate atomic-level processes at a level generally impossible in experiment. The advances in the understanding and modeling of the energetics and interatomic interactions in materials, coupled with advances in computational techniques, make atomistic methods a powerful tool for the analysis of complex materials phenomena [48]. For example, the most detailed information beneath the indenter used in a nanoindentation experiment is revealed by direct *MD* simulations [110, 42]. *MD* simulations of fracture have been used in a number of studies [104, 1] to model the toughness of a material. Coupled with the availability of accurate interatomic potentials for a range of materials, classical *MD* [76] simulations have become a prominent mathematical tool for elucidating complex physical phenomena. However, the length and time scales that can be probed using *MD* are still limited. In current state of the art simulations, *MD* on massively parallel supercomputer can handle about 10^9 atoms using a simple empirical potential, amounting to a volume of less than 1 cubic micron. A typical grain size in metals may be as high as $10 \mu m^3$, so clearly the length scale amenable to atomistic modeling is well below the range required for modeling realistic microstructure. Furthermore, much of the information obtained from the direct large-scale atomistic simulations is excessive and unnecessary. The goal of an atomistic simulation is to focus on regions of the material containing critical physical processes at the nano scale. Large scale atomistic simulations show that the high-energy atoms are clustered around microstructural defects such as grain boundaries or cracks or dislocation lines [2, 53]. The percentage of such high-energy atoms is however a very small fraction of the material specimen. The energies of the majority of atoms are around the average, i.e. these atoms experience slowly changing deformation. Therefore, they are amenable to a larger scale continuum description.

1.2 Continuum Modeling

In the continuum modeling, the solid is described as a continuous medium with average macroscopic properties including internal energy, temperatures, stress and strain [96]. In the average description every mathematical point in the domain of the solid is regarded as a material particle which represents a finite-sized region on the microscale. The material behavior is introduced into the model through a phenomenological constitutive law which relates the pointwise response of the continuum to the local deformation. Although continuum theories of this type are generally regarded as having no internal length scale, the constitutive model is usually developed by assuming a characteristic length inherent the physical constituents of the material particle. For an isotropic Hookean material, the characteristic length would be of the order of several grain sizes that make up the polycrystalline aggregate. For anisotropic elasticity applied to a perfect single crystal, the internal length may be the order of the lattice size[89].

Continuum mechanics has provided a very good empirical description of complex macroscopic phenomena including plasticity and fatigue. In these models, several approaches are used to model the microstructural evolution which is the primary cause of the irreversible macroscopic material response. In the first, appropriate effective material parameters are introduced into the constitutive relation to account for the change in macroscopic response due to microstructural evolution [41]. In the second, a computational model such as the finite element method (*FEM*), is used to directly analyze the microstructural deformation. In yet another approach a nonlocal continuum model is used to describe evolution of microscale parameters. A typical example is Toupin’s couple stress theory where the strain energy is a function of the strain and the curl of the strain instead of strain alone [95]. Recently, Zhu et al. [105] presented a continuum model to predict nanoindentation-induced homogeneous dislocation nucleation. The constitutive relation is obtained from interatomic potentials and a localization criterion based on bifurcation analysis with atomistic interaction was employed to predict dislocation nucleation. While many problems have been well addressed by the above methods, they have some limitations. All continuum models possess inherent length and time scales below which their applicability is questionable. Nonlocal theories often exhibit an added complexity that makes their application difficult. The inherent length scale in these models may also require a separate microscale analysis. For these reasons a single scale continuum model is not always suitable for the modeling of irreversible material response at the lower scale.

1.3 Multi-scale Modeling

The limitations of purely atomistic or purely continuum simulations, has motivated research in multi-scale simulations that bridge atomistic simulation and continuum modeling [14, 63, 80]. In order to make the computations effective, multi-scale models usually decomposes the domain into coarse/fine subregions. The key issue is therefore the coupling between the coarse and fine scales. Depending on the method of information exchange between different scales, multi-scale methods usually fall into two categories: hierarchical approach and concurrent approach.

In hierarchical approach, physical phenomena occurring at different scales are modeled separately and critical information obtained from atomic-scale models are passed to mesoscale or continuum models. At the simplest level, thermal expansion coefficients, elastic constants, and other properties of defect-free crystal can be obtained from atomic models. Then these information were input into continuum models as constitutive material properties. This approach is typified in discrete dislocation techniques [106], wherein dislocations are treated as continuum entities moving in fields determined by elasticity. The approach of passing information from smaller to larger scale model is powerful because no direct coupling of computational methods at different scale is needed. However, this method suffers its own limitations. The small scale phenomena are parametrized via studies of simple defect geometries that may not capture the full complexity of deformation that would emerge from a fully atomistic treatment. Therefore, researchers have developed concurrent methods to avoid information loss when passing information from one length scale to another.

In the concurrent approach, the coarse scale response uses a geometrically approximate description of the underlying microscale to derive its material property. In a small subregion of

the domain, where the geometric microscale description used by the coarse scale breaks down, an atomistic simulation method is used to describe the material response. The microscale description used by the coarse scale and its inherent coupling to the fine scale in regions severe deformation make the resulting method a true two way coupling of length scales. Thus, in concurrent methods, simulations at different length scales are performed *simultaneously* and a smooth coupling is introduced between the different scales. Specifically, full atomistic detail is retained in some critical regions of the material and continuum models (with a built in approximate fine scale description) are used to describe deformation in the material. Concurrent approaches are thus more relevant for studying complicated problems where interaction between fine and coarse scales uses different physical processes in the different regions of the computational domain.

One concurrent method, developed by Abraham, Broughton and co-workers[14], is named after the computation at three different length scales: *Macroscopic*, *Atomistic*, and *Ab initio Dynamics (MAAD)*. In this model, three different computational methods, namely tight-binding(TB), molecular dynamics(MD) and finite element(FE) are concurrently coupled together to simulate crack propagation in a brittle solid. In *MAAD*, the coupling of different regions is achieved by assuming that in the transition region each simulation contribute an equal amount of energy to the total energy. However, there are no rigorous studies performed to verify the effectiveness of this assumption in eliminating spurious wave reflection at the simulation boundaries [53].

The Finite-Element and Atomistic model(FEAt) of Kohlhoff et al. [46] address the problem of a local/non-local mismatch directly through a non-local continuum formulation near the atomistic/continuum interface. Nonlinear elastic finite elements are implemented in continuum region and nonlocal finite elements are used in pad regions. The FEAt model does not use a unified energy function for the entire system, but rather use interface atoms as the boundary condition for finite element model. The main limitation of the model is that it can not easily adapt the size of the atomistic region during the simulation.

The quasicontinuum(QC)[79, 63, 90] method has been used to study many fundamental problems of deformation in crystalline solids such as fracture[63], grain boundary structure and deformation [80, 79], nano-indentation [92, 81] and three-dimension dislocation junctions [77]. In this method, the continuum framework and continuum particle concept are retained, while the phenomenological macroscopic constitutive law is replaced by one derived from direct atomistic calculations. Each continuum particle is replaced by a lattice of a single crystal surrounded by its representative neighbor atom. It defines two types of atoms, 'local representative atoms' and 'non-local representative atoms'. In practice, the regions containing non-local representative atoms are essentially equivalent to the fully atomistic regions of other methods. Similarly, a local representative atom is co-incident with either a continuum *FE* node or an atomic position near a gauss integration point in the element. The energy associated with the local representative atom can be computed by summing up the interatomic potential of the crystallite following the Cauchy-Born rule[18].

In coupled methods, the detailed treatment of the material in the 'transition region' or boundary between the atomistic and continuum regions is a key issue of the computational

model. An approximation is unavoidable because of the fundamental incompatibility between the non-local atomistic description and the local continuum description. This disparity, which is presented in all concurrent methods [18], is accounted for in the *QC* model by adding a *ghost* force [79] which maintains equilibrium of the continuum-atom description of the material under zero load conditions. The total potential energy of *QC* model is obtained by summing the energies of all atoms in the atomistic region & at the interface and all elements in the continuum domains. The *QC* potential energy leads to some non-physical effects. Specifically, taking derivatives of the energy functional, under zero load conditions, to obtain forces on atoms and FE nodes leads to the so-called *ghost* forces in the transition region [64]. The resulting *QC* formulation with ghost force correction is one of the methods where there is no direct coupling in the combined energy functional. Instead the coupling is effected indirectly through the ghost forces with simultaneous solution of two separate but overlapping domains. The overriding rule in such methods is that atoms should 'see', from an energetic point of view, only atoms while continuum nodes should 'see' only continuum nodes[18]. An intermediate approach to handling the ghost forces was taken by some developers of the *QC* model [79]. The exact ghost forces, in this model, were calculated from the initial reference state of the material system, \mathbf{g}^0 , and the negatives of these forces were used as constant 'dead loads' applied on the relevant degrees of freedom(atoms and nodes) throughout the entire course of the simulation.

An alternative approach to eliminate ghost forces is to give up the requirement of a unified energy functional and instead drive the system to equilibrium by seeking a configuration for which the force on all the representative atoms is zero. By using this starting point, the forces need not be obtained strictly as derivatives of a single energy functional, and can instead be approximate expression for a physically motivated set of forces [65]. Knap and Ortiz [44] have proposed a *QC* formulation that is entirely 'non-local' (*QC – FNL*), in that the locality implicit in an FE calculation is eliminated. The basic idea is to use *FE* shape functions to kinematically constrain some atomic positions to nodal positions, and to determine forces from a fully non-local atomistic description at all times and in all regions of the domain. The Cauchy-Born rule is replaced by force calculation from clusters of representative atoms centered at these atomic *FE* nodes. The *QC – FNL* formulation works directly from an approximate expression for the force, rather than from the explicit differentiation of an energy functional. In the *QC – FNL* method, there is simply no transition between continuum region and atomic region, and the only error is introduced by the reduction of degrees of freedom in the regions that are sparsely populated with representative atoms. The main disadvantage of the *QC – FNL* method is that it is computationally expensive in regions of slowly varying deformation gradient as compared to simple elastic constitutive law or even the Cauchy-Born approximation in the *QC* method [18].

The coupled atomistic and discrete dislocation (*CADD*) of [84] has been developed to support the existence of discrete dislocations in the continuum region. The *CADD* method is capable of automatically detecting dislocations as they move across the atomic/continuum interface. *CAAD* is multiscale at the level of defects in that the dislocations are treated differently depending on the region in which they reside. Further, *CADD* allows for the transfer of dislocations between the atomistic and continuum regions with sustained deformation in the material. Though this method was developed independently, it has been shown [18] to be identical to the *QC* method with ghost force correction with a well-defined potential energy.

In order to overcome the requirement of graduating finite-element mesh down to the lattice size, a concurrent coupling method has been recently proposed by Liu and co-workers [99]. One feature of this method is that it is formally assumed that the FE and MD solutions exist simultaneously in the entire computational domain and MD calculations are performed only in the regions that are necessary. The overall concept is to decompose the total displacement field into coarse and fine scales. The coarse scale solution can be interpolated by basic finite element shape functions. The advantages of the bridge scale method are the following. Firstly, it's computational cost is low because it does not require the calculation of any high-order tensors. Secondly, there is no need to mesh the finite element to the lattice size. Finally, the bridging scale method can be extended to finite temperature dynamic problems. The bridging scale method has been successfully used in modeling buckling of multi-walled carbon nanotubes[47]. The main disadvantage of this method is that it does not strictly address regions in which both coarse and fine levels cannot exist simultaneously (for example when FE simulations require element sizes at the fine scale level) and therefore cannot be expected to model such deformations accurately.

In this dissertation a multiscale QC method, in which forces are not derived from an exact potential energy will be used to model defect generation and growth in nanoscale metals at finite temperatures. Such a method would require (a) an efficient/accurate mesh refining strategy to delineate continuum/atomistic regions and (b) accurate interatomic potentials to model internal forces and strain energy density of continuum element. The state of the art w.r.t. to these topics are taken up next.

1.4 Adaptive Finite Element Methods

In order to *efficiently* use the proposed multi-scale model, the atomistic mesh should cover only regions having steep change in the deformation gradient \mathbf{F} . Away from the atomistic regions, the finite element mesh should accurately and efficiently (with minimum DOF) model the deformation in the continuum scale mesostructure. Thus, at any stage of the deformation process, the model should be able to judge the efficacy of FE mesh in interpolating the actual deformation in the material. A broad range of error estimators have been proposed in the computational mechanics literature to access the efficacy of the FE interpolation scheme. Of these the most successful are the a posteriori error estimates [3, 109, 6, 32] which are valid for a very general class of elliptic problems. In these methods, error estimates in the FE solution are generated using the finite element solution of the current FE mesh. Such error estimators can be broken down into two broad categories. They are

1. *Recovery based error estimators*: The FE solution does not produce smooth deformation gradients across element boundaries. In recovery based methods [109, 79] the current finite element solution for deformation gradient \mathbf{F} are smoothed across element boundaries to estimate a more accurate solution to the problem. Smoothing schemes are usually based on continuity of the deformation gradient \mathbf{F} or on a 'superconvergent' \mathbf{F} values in the current finite element solution. The latter strategy has been used to accurately model nanoindentation problems of homogeneous materials [79].

2. *Element residual method* Recovery based error estimators do not always accurately predict errors in the numerical solution [6]. This is especially true for problems involving large gradients/singularities in deformation. Broadly speaking recovery based methods cannot directly predict the so called pollution error, which arises from the difference between current solution and the projection of the actual solution on the current interpolation space. Consequently they over-predict errors in regions where the solution may actually be smooth. Further, recovery based methods cannot predict the relative efficiency of mesh refinement (h) vs polynomial (p) refinement strategies. In this element residual method, local error in a single element is predicted by using higher order interpolation schemes within the element [3, 10, 6, 75] Since they use higher order interpolation schemes, these methods can effectively predict local errors and can also be used for effective mesh adaptation strategies. The main drawback with the method arises from the fact that they use current solution to predict gradient information on element boundaries. Since these current gradients are discontinuous an approximation needs to be made for the local problem and this can either overestimate local errors [3, 10] or prove costly [6, 75].

While the nanoindentation problem does produce regions of steep deformation gradient, the proposed QC model will be using a full blown atomistic description in regions of severe deformation. Bearing in mind that the additional cost involved in using element residual method, the recovery based error estimator will be used in this dissertation to delineate atomistic-continuum regions of the computational model.

1.5 Interatomic Potentials

In both atomistic and multi-scale simulations, potential functions for atoms are used to describe the underlying energetics. The atomistic interaction results from complicated quantum effects taking place at the subatomic level that are responsible for chemical bonds which govern the spatial arrangement of the atoms and breakage of such bonds under external forces [53]. The general structure of the function is represented as [53]:

$$U(\mathbf{r}_1, \mathbf{r}_2, \dots) = \sum_i V_1(\mathbf{r}_i) + \sum_{i,j>i} V_2(\mathbf{r}_i, \mathbf{r}_j) + \sum_{i,j>i,k>j} V_3(\mathbf{r}_i, \mathbf{r}_j, \mathbf{r}_k) + \dots \quad (1.2)$$

Where \mathbf{r}_n is the position vector of the n th particle, and function V_m is the m -body potential. The first term of (1.2) represents the energy due to electrostatic fields in which the system is immersed. The second term is the pair-wise interactions of the particles, the third shows the three body contributions, etc. Jones [39] proposed the following function to describe pair-wise atomic interactions:

$$V(\mathbf{r}_i, \mathbf{r}_j) = V(\mathbf{r}) = 4\epsilon \left[\left(\frac{\sigma}{r} \right)^{12} - \left(\frac{\sigma}{r} \right)^6 \right], r = \|\mathbf{r}_{ij}\| \quad (1.3)$$

This pair-wise potential is simple but does not give adequate description of all properties of metals. The higher-order terms of the potential function (1.2) are typically employed in simulation of solids and complex molecular structures. Essentially, the three-body potential V_3 is intended to provide contribution to the potential energy due to the change of angle between radius vectors $r_{ij} = r_i - r_j$.

One special form of the multi-body potential is the *embedded atom method*(EAM) for metallic systems [20]. The embedded atom method has been applied successfully to studying defects, fracture in grain boundaries on liquid metals and other metallic systems and associated processes [20]. It uses 1st and 2nd order potentials of the kind V_1, V_2 to study the interactions between metal-metal atoms and has been successfully used to model nanoindentation in homogeneous metallic systems [79, 80, 83, 84, 85]. Recently [9, 78], these potentials have been used in metal-metal nanocomposites to model interaction between dissimilar metal atoms. These potentials will form the basis for this dissertation. For more complicated metal-metal (or metal-ceramic) nanocomposites, 3rd order terms V_3 will need to be included. A general methodology for deriving these potential from ab-initio calculations has been proposed in [101, 102].

1.6 Nanoindentation

The indentation test is widely used in nearly all areas of materials science and engineering to predict the onset of plasticity in metallic systems. Typically, in an indentation test, an indenter of a given geometry (such as a cone or a sphere) and material (such as steel or diamond) is pushed into the solid face of a material. If the indenter produces a dislocation in the materials, upon unloading a permanent depression is visible on the surface of the material. An alternate way of describing the onset of plasticity in the material is to experimentally measure the hardness of the surface. The hardness value is usually defined as the ratio of indentation load and the projected area of residual indents. Since the generation of dislocations in the material makes it easier to drive the indenter through the material, the onset of plasticity in the material is reflected through a drop in the hardness of the material. Thus nanoindentation is a powerful way to investigate the mechanical properties of material at the nanoscale [69]. Elastic moduli, hardness, flow strength can be obtained in nanoindentation [68]. An understanding of those properties is therefore an important part of the material design.

A number of nanoindentation experiments have been conducted [43, 97, 58] on metallic systems. Because interaction between atoms breaks down during the formation of the first dislocation, it also signals the transition from elastic to plastic deformation. Currently, it is still difficult to obtain in situ observations of the atoms movement from nanoindentation experiments. Computer simulations have been very useful for a clear understanding of the physical processes taking place during the test. Recently there have been many studies on nanoindentation by using molecular dynamics(*MD*) simulation [110]. Those studies provided good understanding of atomistic mechanisms in nanoindentation response. However, the *MD* simulation faces some serious challenges. The first is the extremely small time steps ($\mathcal{O}(ps)$) used in these simulations. The second one is the small model size. In this dissertation, quasi-static simulation of the *QC* method is used to simulate nanoindentation in metals at finite temperatures. The nanoindentation experiment is chosen in the simulations since it provides an excellent class of problems with two-way interactions between the length scale [79]

The structure of the dissertation is organized as follows. As a background to the dissertation, chapter 2 provides the computational model used in the adaptive continuum scale finite element model. Chapter 3 presents the atomistic calculation of potentials and coupled atomistic/continuum methods to be used in the nanoindentation simulations. Chapter 4 discusses

computational issues related to the implementation of the nanoindentation experiment and suitable examples to elucidate the effectiveness of the method. Conclusions and future applications of the computational model are presented in chapter 5.

Chapter 2

Adaptive Finite Element Method for Continuum Modeling

2.1 Introduction

Finite element method(FEM) is a numerical method used to solve partial differential equations with associated boundary conditions [35]. Individual finite elements can be visualized as small pieces of a structure connected at points called as *nodes*. The primary field of interest (deformation) is qualitatively interpolated (as linear, quadratic etc) within the finite element in terms of nodal values. The assemblage of elements into a finite element mesh is used to simulate the deformation in a structure acted upon by external loads. Even though the the interpolated displacement field is continuous within an element, the resulting deformation in the structure is only piecewise continuous. The quantitative characterization of the deformation in the structure is accomplished by minimizing the resulting potential energy associated with the interpolated displacement field.

Numerically, the minimization of the potential energy of a system of finite elements is represented by a system of algebraic equations to solved for unknown deformation at the nodes. The solution for nodal quantities, when combined with the assumed field in any given element, completely determines the spatial variation of the primary/secondary fields in the element. Since the *assumed* displacement field within the finite elements are restricted to qualitative representations, the resulting numerical solution is approximate. In other words, the actual variation in the region spanned by an element is usually more complicated than the assumed displacement field. Consequently the *FE* solution is only an approximation to the actual solution of the partial differential equations.

2.2 Overview of the Finite Element Method for Structural Problems

The underlying differential equations and associated boundary conditions for a continuum occupying an initial configuration Ω_0 [57], is given as

2.2.1 Strong Form of the Problem

1)Equilibrium equations

$$T_{ij,j} + f_i = 0 \text{ (in } \Omega_0) \quad (2.1)$$

2)Displacement boundary condition

$$u_i = g_i \text{ (on } \partial\Omega_{0u}) \quad (2.2)$$

3)Traction boundary condition

$$T_{ij}n_j = h_i \text{ (on } \partial\Omega_{0t}) \quad (2.3)$$

where T_{ij} denote the Cartesian components of the 1st Piola-Kirchoff *stress tensor*, u_i denote the *displacement vector* and f_i is the *prescribed body force per unit volume*. The boundary $\partial\Omega_0$ consists of two disjoint portions, namely $\partial\Omega_{0u}$ where displacements are specified and $\partial\Omega_{0t}$ where tractions are applied with $\partial\Omega_{0u} \cup \partial\Omega_{0t} = \partial\Omega_0$. The functions g_i and h_i are respectively called the *prescribed boundary displacements* and *prescribed tractions*. The above three equations are a formal statement of the strong form of the boundary-value problem. If the position of continuum level *material* points in the original configuration Ω_0 are denoted by X_i , then the deformation gradient can be written as

$$F_{ij} = \frac{\partial u_i}{\partial X_j} + I(\text{strain-displacement equation}) \quad (2.4)$$

In order to combine the traction boundary conditions with the displacement boundary conditions, we need to define a relationship between the 1st Piola- Kirchoff stress tensor and the deformation gradient. For a conservative elastic body, the first Piola-Kirchoff stress tensor T_{ij} is related to the deformation gradient F_{ij} through the strain energy density $W(F_{ij})$ through the equation

$$T_{ij} = \frac{\partial W}{\partial F_{ij}} \quad (2.5)$$

2.2.2 Weak or Variational Statement

The solution to the partial differential equations (2.1, 2.2&2.3) subject to the constitutive equation (2.5) defines the resulting deformation (and hence the stress) inside the body. However in many problems of practical interest an exact solution is not readily available, and consequently the system needs to be converted into a more tractable form called the weak (or variational) form of the underlying *PDEs*. In order to derive the weak form of the *PDEs* consider a trial solution space $\delta_i = \delta_i(X_j)$ and a variation space $v_i = v_i(X_j)$ such that

$$\begin{aligned} u_i &\in \delta_i \text{ if } u_i = g_i \text{ on } \partial\Omega_{0u} \\ w_i &\in v_i \text{ if } w_i = 0 \text{ on } \partial\Omega_{0u} \end{aligned} \quad (2.6)$$

Then the actual solution u_i to the *PDEs* in eqns. (2.1,2.2&2.3) is such that

$$\int_{\Omega_0} \frac{\partial w_i}{\partial X_j} T_{ij} d\Omega = \int_{\Omega_0} w_i f_i d\Omega + \int_{\partial\Omega_{0t}} w_i h_i dS \quad \forall w_i \in v_i \quad (2.7)$$

where T_{ij} is defined in terms of u_i through the constitutive equation (2.5). Equation (2.7) is referred to as the *principle of virtual work* or *principle of virtual displacement* or the *weak form* associated with the primary variables u_i and its associated *virtual displacement* w_i .

2.2.3 Galerkin Formulation

The finite element method is generated by using a Galerkin formulation of the weak form. In this method the solution to the weak form in equation (2.7) is sought subject to the approximation to the trial and solution space. Specifically, the solution space u_i is assumed to have the same the interpolation character (piecewise linear/quadratic etc) of the virtual displacements w_i . In

matrix-vector notation, if the trial solution $\{\mathbf{u}\} = \begin{Bmatrix} u_1(X_1, X_2, X_3) \\ u_2(X_1, X_2, X_3) \\ u_3(X_1, X_2, X_3) \end{Bmatrix}$ is interpolated within a finite element e as

$$u_j(X_1, X_2, X_3) \approx \hat{u}_j(X_1, X_2, X_3) = \sum_i^n N_i(X_1, X_2, X_3) d_{ji} \text{ for } j = 1 \cdots 3$$

$$\text{or } \{\mathbf{u}\} \approx \{\hat{\mathbf{u}}\} = \begin{Bmatrix} \sum_i^n N_i d_{1i} \\ \sum_i^n N_i d_{2i} \\ \sum_i^n N_i d_{3i} \end{Bmatrix} = [\mathbf{N}]\{\mathbf{d}\} \text{ for } (X_1, X_2, X_3) \in \Omega_{0e} \quad (2.8)$$

where $N_i = N_i(X_k)$ are the shape functions ($[\mathbf{N}]$ is the shape function matrix) within the finite element and d_{ji} are the unknown displacement along the j th coordinate direction of the i th element node ($\{\mathbf{d}\}$ is the element displacement vector). The virtual displacements can now be written using the same shape function matrix $[\mathbf{N}]$ as

$$\{\mathbf{w}\} \approx \{\hat{\mathbf{w}}\} = [\mathbf{N}]\{\delta\mathbf{d}\} \forall \mathbf{X} \in \Omega_{0e} \quad (2.9)$$

where $\{\delta\mathbf{d}\}$ is the virtual element displacement vector. The deformation gradient of the virtual displacement field can now be written as

$$\frac{\partial w_i}{\partial X_j} = \sum_j \sum_i \frac{\partial N_i}{\partial X_j} \delta d_{ji} \Rightarrow$$

$$\{\delta\mathbf{F}\} = [\mathbf{B}]\{\delta\mathbf{d}\} \quad (2.10)$$

where the virtual deformation gradient vector $\{\delta\mathbf{F}\} = \begin{Bmatrix} \delta F_{11} = \frac{\partial w_1}{\partial X_1} \\ \delta F_{12} = \frac{\partial w_1}{\partial X_2} \\ \vdots \end{Bmatrix}$ and $[\mathbf{B}]$ is referred to

as the strain-displacement matrix. The unknown element displacement vector $\{\mathbf{d}\}$ are usually assembled into a global displacement vector $\{\mathbf{D}\}$ corresponding the unknown displacements at the nodes of the finite element mesh with $\{\mathbf{d}\} = [\mathbf{\Gamma}_e]\{\mathbf{D}\}$ where $[\mathbf{\Gamma}_e]$ is the transformation matrix for the FE . The resulting numerical system generated by the Galerkin method can now be written as

$$\begin{aligned} & \text{Determine } \{\mathbf{D}\} \text{ such that} \\ & \{\delta\mathbf{D}\}^T \sum_e [\mathbf{\Gamma}_e]^T \int_{\Omega_{0e}} [\mathbf{B}]^T \{\mathbf{T}\} d\Omega = \{\delta\mathbf{D}\}^T \{\mathbf{F}_{nodal}\} + \{\delta\mathbf{D}\}^T \sum_e [\mathbf{\Gamma}_e]^T \int_{\Omega_{0e}} [\mathbf{N}]^T \{\mathbf{f}\} \Omega_e + \\ & \quad \{\delta\mathbf{D}\}^T \sum_e [\mathbf{\Gamma}_e]^T \int_{\partial\Omega_{0et}} [\mathbf{N}] \{\mathbf{h}\} dS_e \quad \forall \{\delta\mathbf{D}\} \Rightarrow \\ & \sum_e [\mathbf{\Gamma}_e]^T \int_{\Omega_{0e}} [\mathbf{B}]^T \{\mathbf{T}\} d\Omega = \{\mathbf{F}_{nodal}\} + \sum_e \int_{\Omega_{0e}} [\mathbf{N}]^T \{\mathbf{f}\} \Omega_e + \sum_e \int_{\partial\Omega_{0et}} [\mathbf{N}] \{\mathbf{h}\} dS_e \quad (2.11) \end{aligned}$$

where the 1st Piola-Kirchoff stress vector $\{\mathbf{T}\} = \begin{Bmatrix} T_{11} \\ T_{12} \\ \vdots \end{Bmatrix}$. Since a specific approximation is made to the shape function $[\mathbf{N}]$, the resulting solution to the FE equation (2.11) is an approximation to the actual solution of the weak form in equation (2.7). Also, since the strain energy density $W(F_{ij})$ (and therefore the 1st Piola-Kirchoff stress T_{ij}) is a nonlinear function of the deformation gradient F_{ij} , the FE equation (2.11) needs to be solved iteratively using a Newton type nonlinear method.

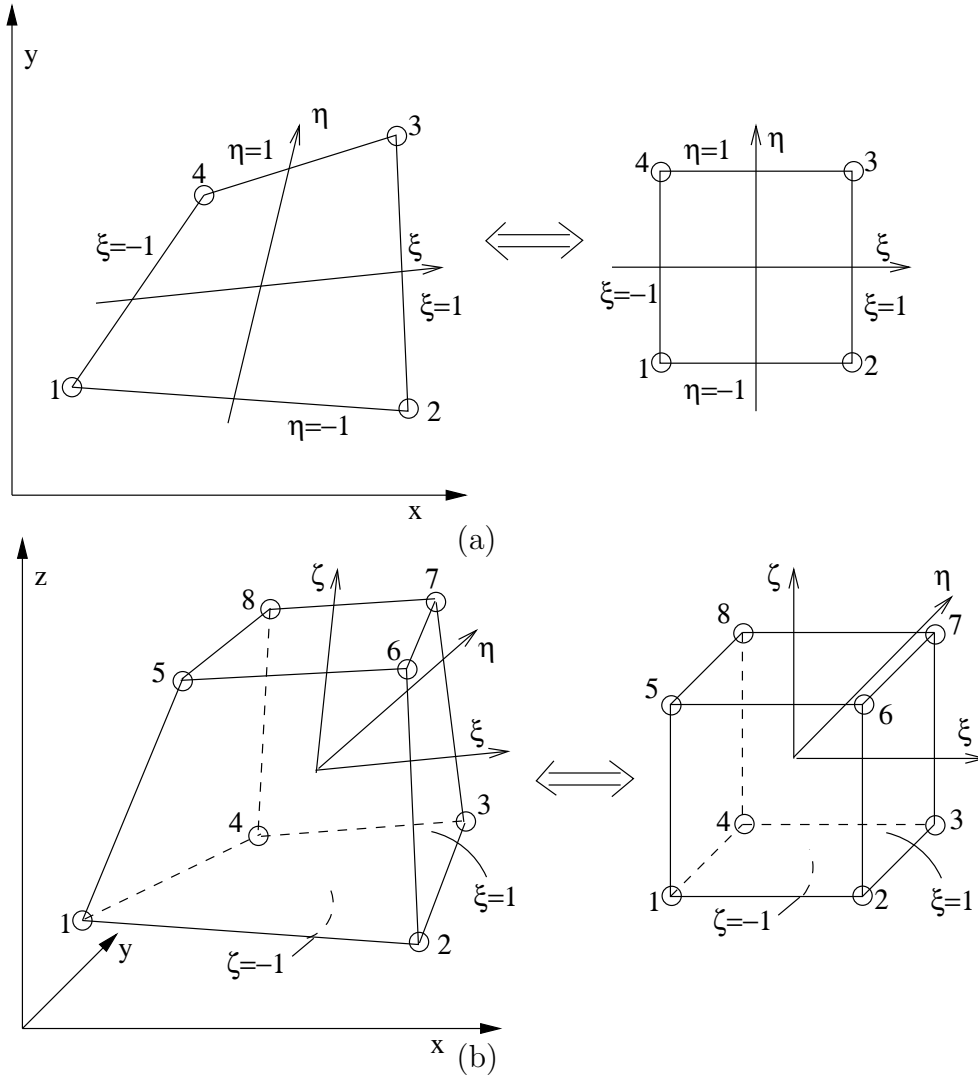


Figure 2.1: Isoparametric mapping from physical to reference coordinates for a (a) 2d and (b) 3d finite element

2.3 Isoparametric Elements

The continuum description of deformation in the body does not allow for the formation or destruction of infinitesimal mass elements. Consequently the deformation $u_j(X_k)$ must satisfy C^0 continuity conditions across the element boundaries. In order to interpolate such displacement fields the isoparametric description of the FE is often used. As shown in figure (2.1), isoparametric elements use reference coordinates ξ, η (& ζ in 3d) to map the physical element space X_k into a reference element that is a square (in $2d$) or a cube (in $3d$). The bijective mapping is such that the physical coordinates for a point in the reference system can be obtained as $X_k = X_k(\xi, \eta, \zeta) = \sum_{i=1}^n N_i(\xi, \eta, \zeta) X_k^{(i)}$, where $X_k^{(i)}$ represents the k th coordinate of the i th node in the finite element. The isoparametric shape functions $N_i(\xi, \eta, \zeta)$ are such that along element boundary $\partial\Omega_{0e}$ they are nonzero only for $i \in \partial\Omega_{0e}$. Consequently adjacent finite elements have the same interpolation along the common element boundary, ensuring C^0 continuity of the physical coordinates. The deformation inside the element uses the same shape functions used for the physical coordinates, i.e. $\hat{u}_k(\xi, \eta, \zeta) = \sum_{i=1}^n N_i(\xi, \eta, \zeta) d_{ki}$ and consequently the deformation field is also continuous within the element. In this thesis, two such isoparametric elements will be used. They are

2.3.1 Bilinear Quadrilateral Element(Q4)

In this $2d$ linear quadrilateral element attributed to Taig[93], the physical coordinates are written as

$$\begin{Bmatrix} X_1 \\ X_2 \end{Bmatrix} = \begin{Bmatrix} \sum_{i=1}^4 N_i X_1^{(i)} \\ \sum_{i=1}^4 N_i X_2^{(i)} \end{Bmatrix} = [\mathbf{N}] \{\mathbf{X}\} \quad (2.12)$$

and

$$\begin{Bmatrix} u_1 \\ u_2 \end{Bmatrix} = \begin{Bmatrix} \sum N_i d_{1i} \\ \sum N_i d_{2i} \end{Bmatrix} = [\mathbf{N}] \{\mathbf{d}\} \quad (2.13)$$

with

$$\begin{aligned} \{X\} &= [X_1^{(1)} \ X_2^{(1)} \ X_1^{(2)} \ X_2^{(2)} \ X_1^{(3)} \ X_2^{(3)} \ X_1^{(4)} \ X_2^{(4)}]^T \\ \{d\} &= [d_{11} \ d_{21} \ d_{12} \ d_{22} \ d_{13} \ d_{23} \ d_{14} \ d_{24}]^T \\ [\mathbf{N}] &= \begin{bmatrix} N_1 & 0 & N_2 & 0 & N_3 & 0 & N_4 & 0 \\ 0 & N_1 & 0 & N_2 & 0 & N_3 & 0 & N_4 \end{bmatrix} \end{aligned} \quad (2.14)$$

The shape functions can be obtained in terms of the isoparametric coordinates ξ, η [35] as

$$N_i = N_i(\xi, \eta) = \frac{1}{4}(1 + \xi_i \xi)(1 + \eta_i \eta) \quad (2.15)$$

where (ξ_i, η_i) are the isoparametric coordinates of the i th local node. The *Jacobian Matrix* $[\mathbf{J}]$ defining the coordinate transformation can be written as

$$[\mathbf{J}] = \begin{bmatrix} \frac{\partial X_1}{\partial \xi} & \frac{\partial X_2}{\partial \xi} \\ \frac{\partial X_1}{\partial \eta} & \frac{\partial X_2}{\partial \eta} \end{bmatrix} = \begin{bmatrix} \sum N_{i,\xi} X_1^{(i)} & \sum N_{i,\xi} X_2^{(i)} \\ \sum N_{i,\eta} X_1^{(i)} & \sum N_{i,\eta} X_2^{(i)} \end{bmatrix} \quad (2.16)$$

We can now write

$$\begin{aligned}
\begin{Bmatrix} \frac{\partial u_1}{\partial X_1} \\ \frac{\partial u_1}{\partial X_2} \end{Bmatrix} &= [\mathbf{J}]^{-1} \begin{bmatrix} N_{1,\xi} & 0 & N_{2,\xi} & 0 & N_{3,\xi} & 0 & N_{4,\xi} & 0 \\ N_{1,\eta} & 0 & N_{2,\eta} & 0 & N_{3,\eta} & 0 & N_{4,\eta} & 0 \end{bmatrix} \{\mathbf{d}\} \\
&= [\mathbf{B1}]\{\mathbf{d}\} \\
\begin{Bmatrix} \frac{\partial u_2}{\partial X_1} \\ \frac{\partial u_2}{\partial X_2} \end{Bmatrix} &= [\mathbf{J}]^{-1} \begin{bmatrix} 0 & N_{1,\xi} & 0 & N_{2,\xi} & 0 & N_{3,\xi} & 0 & N_{4,\xi} \\ 0 & N_{1,\eta} & 0 & N_{2,\eta} & 0 & N_{3,\eta} & 0 & N_{4,\eta} \end{bmatrix} \{\mathbf{d}\} \\
&= [\mathbf{B2}]\{\mathbf{d}\} \\
\text{or } \{\mathbf{F}\} &= \begin{Bmatrix} \frac{\partial u_1}{\partial X_1} \\ \frac{\partial u_1}{\partial X_2} \\ \frac{\partial u_2}{\partial X_1} \\ \frac{\partial u_2}{\partial X_2} \end{Bmatrix} = \begin{bmatrix} B_{111} & B_{112} & B_{113} & B_{114} & B_{115} & B_{116} & B_{117} & B_{118} \\ B_{121} & B_{122} & B_{123} & B_{124} & B_{125} & B_{126} & B_{127} & B_{128} \\ B_{211} & B_{212} & B_{213} & B_{214} & B_{215} & B_{216} & B_{217} & B_{218} \\ B_{221} & B_{222} & B_{223} & B_{224} & B_{225} & B_{226} & B_{227} & B_{228} \end{bmatrix} \{\mathbf{d}\} \\
&= [\mathbf{B}]\{\mathbf{d}\} \tag{2.17}
\end{aligned}$$

where the strain displacement matrix $[\mathbf{B}]$ was obtained using equation (2.10). Since the virtual displacement field w_i is obtained using the same shape functions as the solution displacement field u_i (i.e. $w_j = \sum_{i=1}^4 N_i(\xi, \eta)\delta d_{ji}$), the virtual deformation gradient $\{\delta\mathbf{F}\}$ can be written as

$$\{\delta\mathbf{F}\} = [\mathbf{B}]\{\delta\mathbf{d}\}$$

The *FE* equations (2.11) are now written as

$$\begin{aligned}
&\text{Determine } \{\mathbf{D}\} \text{ such that} \\
\sum_e [\mathbf{\Gamma}_e]^T \int_{-1}^1 \int_{-1}^1 [\mathbf{B}]^T \{\mathbf{T}\} J d\xi d\eta &= \{\mathbf{F}_{nodal}\} + \sum_e \int_{-1}^1 \int_{-1}^1 [\mathbf{N}]^T \{\mathbf{f}\} J d\xi d\eta + \\
&\sum_e \int_{\partial\Omega_{out}} [\mathbf{N}]\{\mathbf{h}\} dS_e \tag{2.18}
\end{aligned}$$

where $J = |[\mathbf{J}]|$ is the Jacobian of the transformation and the stress vector is a function of the unknown nodal displacements, i.e. $\{\mathbf{T}\} = \{\mathbf{T}(\{\mathbf{D}\})\}$.

2.3.2 Trilinear Hexahedral Element(H8)

The trilinear hexahedral element is the basic element for three-dimensional analysis. The eight-node solid element is analogous to the previous four-node plane Q4 element. Geometry and displacements are given by

$$\begin{Bmatrix} X_1 \\ X_2 \\ X_3 \end{Bmatrix} = \begin{Bmatrix} \sum_{i=1}^8 N_{1i} X_1^{(i)} \\ \sum_{i=1}^8 N_{2i} X_2^{(i)} \\ \sum_{i=1}^8 N_{3i} X_3^{(i)} \end{Bmatrix} \tag{2.19}$$

and

$$\begin{Bmatrix} u_1 \\ u_2 \\ u_3 \end{Bmatrix} = \begin{Bmatrix} \sum_{i=1}^8 N_{1i} d_{1i} \\ \sum_{i=1}^8 N_{2i} d_{2i} \\ \sum_{i=1}^8 N_{3i} d_{3i} \end{Bmatrix} \tag{2.20}$$

The shape functions can be obtained in terms of the transformed isoparametric coordinate (ξ, η, ζ) as

$$N_{ji} = N_i(\xi, \eta, \zeta) = \frac{1}{8}(1 + \xi_i\xi)(1 + \eta_i\eta)(1 + \zeta_i\zeta) \quad (2.21)$$

where (ξ_i, η_i, ζ_i) are the isoparametric coordinates of the i th local node. The *JacobianMatrix* is

$$[J] = \begin{bmatrix} X_{1,\xi} & X_{2,\xi} & X_{3,\xi} \\ X_{1,\eta} & X_{2,\eta} & X_{3,\eta} \\ X_{1,\zeta} & X_{2,\zeta} & X_{3,\zeta} \end{bmatrix} = \begin{bmatrix} \sum N_{i,\xi} X_1^{(i)} & \sum N_{i,\xi} X_2^{(i)} & \sum N_{i,\xi} X_3^{(i)} \\ \sum N_{i,\eta} X_1^{(i)} & \sum N_{i,\eta} X_2^{(i)} & \sum N_{i,\eta} X_3^{(i)} \\ \sum N_{i,\zeta} X_1^{(i)} & \sum N_{i,\zeta} X_2^{(i)} & \sum N_{i,\zeta} X_3^{(i)} \end{bmatrix} \quad (2.22)$$

We can now write

$$\begin{aligned} \begin{Bmatrix} \frac{\partial u_1}{\partial X_1} \\ \frac{\partial u_1}{\partial X_2} \\ \frac{\partial u_1}{\partial X_3} \end{Bmatrix} &= [\mathbf{J}]^{-1} \begin{bmatrix} N_{1,\xi} & 0 & 0 & N_{2,\xi} & 0 & 0 & \cdots & N_{8,\xi} & 0 & 0 \\ N_{1,\eta} & 0 & 0 & N_{2,\eta} & 0 & 0 & \cdots & N_{8,\eta} & 0 & 0 \\ N_{1,\zeta} & 0 & 0 & N_{2,\zeta} & 0 & 0 & \cdots & N_{8,\zeta} & 0 & 0 \end{bmatrix} \{\mathbf{d}\} \\ &= [\mathbf{B1}]\{\mathbf{d}\} \\ \begin{Bmatrix} \frac{\partial u_2}{\partial X_1} \\ \frac{\partial u_2}{\partial X_2} \\ \frac{\partial u_2}{\partial X_3} \end{Bmatrix} &= [\mathbf{J}]^{-1} \begin{bmatrix} 0 & N_{1,\xi} & 0 & 0 & N_{2,\xi} & 0 & 0 & \cdots & N_{8,\xi} & 0 \\ 0 & N_{1,\eta} & 0 & 0 & N_{2,\eta} & 0 & 0 & \cdots & N_{8,\eta} & 0 \\ 0 & N_{1,\zeta} & 0 & 0 & N_{2,\zeta} & 0 & 0 & \cdots & N_{8,\zeta} & 0 \end{bmatrix} \{\mathbf{d}\} \\ &= [\mathbf{B2}]\{\mathbf{d}\} \\ \begin{Bmatrix} \frac{\partial u_3}{\partial X_1} \\ \frac{\partial u_3}{\partial X_2} \\ \frac{\partial u_3}{\partial X_3} \end{Bmatrix} &= [\mathbf{J}]^{-1} \begin{bmatrix} 0 & 0 & N_{1,\xi} & 0 & 0 & N_{2,\xi} & 0 & 0 & \cdots & N_{8,\xi} \\ 0 & 0 & N_{1,\eta} & 0 & 0 & N_{2,\eta} & 0 & 0 & \cdots & N_{8,\eta} \\ 0 & 0 & N_{1,\zeta} & 0 & 0 & N_{2,\zeta} & 0 & 0 & \cdots & N_{8,\zeta} \end{bmatrix} \{\mathbf{d}\} \\ &= [\mathbf{B3}]\{\mathbf{d}\} \\ \{\mathbf{F}\} &= \begin{Bmatrix} \frac{\partial u_1}{\partial X_1} \\ \frac{\partial u_1}{\partial X_2} \\ \frac{\partial u_1}{\partial X_3} \\ \frac{\partial u_2}{\partial X_1} \\ \frac{\partial u_2}{\partial X_2} \\ \frac{\partial u_2}{\partial X_3} \\ \frac{\partial u_3}{\partial X_1} \\ \frac{\partial u_3}{\partial X_2} \\ \frac{\partial u_3}{\partial X_3} \end{Bmatrix} = \begin{bmatrix} B1_{11} & B1_{12} & \cdots & \cdots & \cdots \\ B1_{21} & B1_{22} & \cdots & \cdots & \cdots \\ B2_{11} & B2_{12} & \cdots & \cdots & \cdots \\ B2_{21} & B2_{22} & \cdots & \cdots & \cdots \\ B3_{11} & B3_{12} & \cdots & \cdots & \cdots \\ B3_{21} & B3_{22} & \cdots & \cdots & \cdots \end{bmatrix} \{\mathbf{d}\} \\ &= [\mathbf{B}]\{\mathbf{d}\} \end{aligned} \quad (2.23)$$

where the strain displacement matrix $[\mathbf{B}]$ was obtained using equation (2.10). Since the virtual displacement field w_i is obtained using the same shape functions as the solution displacement field u_i (i.e. $w_j = \sum_{i=1}^4 N_i(\xi, \eta)\delta d_{ji}$), the virtual deformation gradient $\{\delta\mathbf{F}\}$ can be written as

$$\{\delta\mathbf{F}\} = [\mathbf{B}]\{\delta\mathbf{d}\}$$

The *FE* equations (2.11) are now written as

$$\text{Determine } \{\mathbf{D}\} \text{ such that}$$

$$\begin{aligned} \sum_e [\mathbf{\Gamma}_e]^T \int_{-1}^1 \int_{-1}^1 \int_{-1}^1 [\mathbf{B}]^T \{\mathbf{T}\} J d\xi d\eta d\zeta &= \{\mathbf{F}_{nodal}\} + \sum_e \int_{-1}^1 \int_{-1}^1 \int_{-1}^1 [\mathbf{N}]^T \{\mathbf{f}\} J d\xi d\eta d\zeta + \\ &\sum_e \int_{\partial\Omega_{0et}} [\mathbf{N}] \{\mathbf{h}\} dS_e \end{aligned} \quad (2.24)$$

where $J = |[\mathbf{J}]|$ is the Jacobian of the transformation and the stress vector is a function of the unknown nodal displacements, i.e. $\{\mathbf{T}\} = \{\mathbf{T}(\{\mathbf{D}\})\}$. It can be shown [109] that the above two isoparametric elements satisfy the convergence requirements when $|\mathbf{J}| > 0$.

2.3.3 Numerical Integration Using Gaussian Quadrature

Integration of expressions in equations (2.18&2.24) are performed numerically using gauss quadrature [35]. For example, the function $\phi = \phi(\xi, \eta)$ in 2d, the gauss quadrature rule is of the form

$$I = \int_{-1}^1 \int_{-1}^1 \phi(\xi, \eta) d\xi d\eta = \sum_i \sum_j W_i W_j \phi(\xi_i, \eta_j) \quad (2.25)$$

We implement 2×2 gauss rule in Q4 elements and $2 \times 2 \times 2$ gauss rule in the H8 element. On element boundaries we perform 2×1 and 2×2 gauss quadrature for the Q4 and H8 elements. The required weight/gauss points can be found in [35].

2.4 Solution to the Finite Element Equations

Given the global solution vector $\{\mathbf{D}\}$ at the nodes of the finite element mesh, the local element displacement vector can be obtained as $\{\mathbf{d}\} = [\mathbf{\Gamma}_e] \{\mathbf{D}\}$. This in turn can be used along with equations (2.17 or 2.23) to determine deformation gradient $\{\mathbf{F}\} = [\mathbf{B}] \{\mathbf{d}\}$ within the finite element. Using the constitutive equation (2.5), the stress vector $\{\mathbf{T}\}$ in a finite element can now be written as

$$\begin{aligned} \{\mathbf{T}\} &= \frac{\partial W}{\partial \{\mathbf{F}\}} \\ &= \{\mathbf{T}\}(\{\mathbf{d}\}) = \{\mathbf{T}\}(\{\mathbf{D}\}) \end{aligned} \quad (2.26)$$

Since the strain energy density W is nonlinear function of its arguments, the stress vector $\{\mathbf{T}\}(\{\mathbf{D}\})$ is also a nonlinear function of its arguments. Thus the finite element equations (2.18&2.24) needs to be solved using Newton type iterative methods. In these methods the $p + 1$ th trial solution $\{\mathbf{D}\}^{p+1}$ is obtained as $\{\mathbf{D}\}^{p+1} = \{\mathbf{D}\}^p + \{\Delta\mathbf{D}\}^p$ so that

$$\{\mathbf{T}\}^{p+1} \approx \{\mathbf{T}\}^p + \left. \frac{\partial \{\mathbf{T}\}^p}{\partial \{\mathbf{F}\}} \right|_{\{\mathbf{F}\}^p} \frac{\partial \{\mathbf{F}\}}{\partial \{\mathbf{d}\}^p} \{\Delta\mathbf{d}\}^p = \{\mathbf{T}\}^p + [\mathbf{E}]_{tan} [\mathbf{B}] [\mathbf{\Gamma}_e] \{\Delta\mathbf{D}\}^p \quad (2.27)$$

where the tangent modulus $[\mathbf{E}]_{tan} = \frac{\partial^2 U}{\partial \{\mathbf{F}\}^2}$. If we write element internal force vector $\{\mathbf{f}_e\}^p$ at the p -th iterate as

$$\begin{aligned} \{\mathbf{f}_e\}^p &= [\mathbf{\Gamma}_e]^T \int_{-1}^1 \int_{-1}^1 [\mathbf{B}]^T \{\mathbf{T}\}^p J d\xi d\eta \quad (2d) \\ &= [\mathbf{\Gamma}_e]^T \int_{-1}^1 \int_{-1}^1 \int_{-1}^1 [\mathbf{B}]^T \{\mathbf{T}\} J d\xi d\eta d\zeta \quad (3d) \end{aligned} \quad (2.28)$$

and the correspond element stiffness matrix $[\mathbf{k}_e]^p$ as

$$\begin{aligned} [\mathbf{k}_e]^p &= [\mathbf{\Gamma}_e]^T \int_{-1}^1 \int_{-1}^1 [\mathbf{B}]^T [\mathbf{E}]_{tan} [\mathbf{B}] [\mathbf{\Gamma}_e] J d\xi d\eta \quad (2d) \\ &= [\mathbf{\Gamma}_e]^T \int_{-1}^1 \int_{-1}^1 \int_{-1}^1 [\mathbf{B}]^T [\mathbf{E}]_{tan} [\mathbf{B}] [\mathbf{\Gamma}_e] J d\xi d\eta d\zeta \quad (3d) \end{aligned} \quad (2.29)$$

the FE equations (2.18 or 2.24) can be written at the p th Newton iteration as

$$\begin{aligned} \left(\sum_e [\mathbf{k}_e]^p \right) \{\Delta \mathbf{D}\}^p &= \{\mathbf{F}_{nodal}\} + \sum_e \int_{-1}^1 \int_{-1}^1 \int_{-1}^1 [\mathbf{N}]^T \{\mathbf{f}\} J d\xi d\eta d\zeta + \\ &\quad \sum_e \int_{\partial\Omega_{0et}} [\mathbf{N}] \{\mathbf{h}\} dS_e - \sum_e \{\mathbf{f}_e\}^p \Rightarrow \\ [\mathbf{K}]^p \{\Delta \mathbf{D}\}^p &= \{\mathbf{F}_{res}\}^p \end{aligned} \quad (2.30)$$

where $\{\mathbf{F}_{res}\}^p$ is the global residual vector and $[\mathbf{K}]^p$ is the global stiffness matrix at the p -th iteration. In this dissertation the secant based quasi-Newton method [56] will be used to approximate the the global stiffness matrix $[\mathbf{K}]^p$ based on a Broyden update of $[\mathbf{K}]^1$. Such a method avoids repeated recalculation and inversion of the global stiffness matrix at each iteration and is predicted to converge superlinearly [21] for elliptic $PDEs$. Also, the method does not require accurate gradients of the integral expressions in equations (2.18&2.24) and the secant update is known to perform very efficiently for QC methods [79]. Each iteration in the nonlinear quasi-Newton solver requires the solution to an unsymmetrical system of linear equations of the form $[\mathbf{K}]^o \{\Delta \mathbf{D}\}^p = \{\mathbf{F}\}^p$. In this dissertation, each iterate will be solved using the *Biconjugate gradient method* (BCM) with a *SSOR* preconditioner[28].

2.5 Recovery Based Aposteriori Error Estimate

A finite element solution has enough information to estimate its own error. The estimate is based on the difference between an element-by-element field and an alternative field, presumably more accurate and usually obtained by a smoothing operation.

2.5.1 Global Smoothing

C^0 type elements used in the FE analysis do not display inter-element continuity of strain (or stress). In such cases, one usually resorts to nodal averaging of element stress(or strain) as is frequently done in FE practice. However, it is possible to *recover* a better stress distribution by a *projection* or *smoothing operation*. The smoothed results are continuous across elements and usually more accurate. One way of smoothing is to determine nodal values of a smoothed field by a least-squares fit, minimizing the square of the difference between the smoothed field and the element-by-element filed. We write the function

$$F_G = \sum \int_{\Omega_e} (T_{ij}^* - T_{ij})^2 d\Omega_e \quad (2.31)$$

where T_{ij} denotes FEM solution for stress, T_{ij}^* denotes projected stress. T_{ij}^* is such a C^0 continuous field interpolated by the same shape functions used for the displacement field.

$$\{\mathbf{T}^*\} = [\mathbf{N}]\{\bar{\mathbf{T}}^*\} \quad (2.32)$$

where nodal stress $\{\bar{\mathbf{T}}^*\}$ are unknowns to be solved for numerically. To minimize the square of the difference we need to solve

$$\frac{\partial F_G}{\partial \mathbf{T}^*} = \{0\} \quad (2.33)$$

which yield a linear system of the form

$$\left(\sum \int_{\Omega_{0e}} [\mathbf{N}]^T [\mathbf{N}] d\Omega_e \right) \{\bar{\mathbf{T}}^*\} = \sum \int_{\Omega_{0e}} [\mathbf{N}]^T \{\mathbf{T}\} d\Omega_e \quad (2.34)$$

which is to be solved using the *BCM* solver discussed in the previous section.

2.5.2 ZZ Error Estimate

The specification of local error in the manner given in equations

$$\begin{aligned} e_u &= u - u^* \\ \mathbf{T}_u &= \mathbf{T} - \mathbf{T}^* \end{aligned} \quad (2.35)$$

is generally not convenient and occasionally misleading. For example, under a point load both errors in displacements and stresses will be locally infinite but the overall solution may still be acceptable. Similar situation will exist near reentrant corners. For this reason various 'norms' representing some integral scalar quantity are often introduced to measure the error or indeed the function itself. For linear elasticity problems, the global energy error norm written as [108]

$$\|e\| = \left[\int_{\Omega} (\mathbf{F} - \mathbf{F}^*)^T (\mathbf{T} - \mathbf{T}^*) d\Omega \right]^{1/2} \quad (2.36)$$

is most often used. Alternatively one can work with L_2 norm of stress error

$$\|e_\omega\|_{L_2} = \left[\int_{\Omega} (\mathbf{T} - \mathbf{T}^*)^T (\mathbf{T} - \mathbf{T}^*) d\Omega \right]^{1/2} \quad (2.37)$$

Although all the norms written above are defined on the whole domain, we note that the corresponding element wise norms can be obtained by performing the integral over element domains, i.e.

$$\|e\|^2 = \sum_{i=1}^m \|e\|_e^2 \quad (2.38)$$

where e refers to individual elements and m the total element number. Relative errors can also be defined as

$$\eta = \left[\frac{\|e\|^2}{\|u\|^2 + \|e\|^2} \right]^{1/2} \times 100\% \quad (2.39)$$

The percentage error η can be used over a single or patch of elements to locally determine the efficacy of the interpolation scheme.

Belytschko et.al. [11] examined various types of error criteria, such as *ZZ* L_2 -projection on stresses strains and energies, for a broad class of *PDEs* with steep gradients of deformation. They found that criteria based on energy or strain errors are quite effective in predicting local refinement. In fact, the stress field in and adjacent to a localization band which is triggered by strain softening is nearly constant, so that the *ZZ* criterion (over stress) never initiates refinement in the area of localization. Consequently they proposed an L_2 strain-projection(SP) criterion of the form

$$e_i^{sp} = \left[\frac{1}{\Omega_i} \int_{\Omega_i} (\mathbf{F} - \mathbf{F}^*)^T (\mathbf{F} - \mathbf{F}^*) d\Omega \right]^{1/2} \quad (2.40)$$

where \mathbf{F}^* is evaluated by an L_2 projection which is identical to the L_2 projection of \mathbf{T}^* . This measure represents the RMS strain error in an element and is convenient to use because it is non-dimensional. It is shown that this technique effectively captures the region where *FE* mesh refinements are required. In this thesis the corresponding energy projection norm in conjunction with a *ZZ* error estimator will be used . Thus, the discretization error in element e can be defined as

$$\epsilon_e = \left[\frac{1}{\Omega_e} \int_{\Omega_e} (\bar{\mathbf{F}} - \mathbf{F}_e)^T (\bar{\mathbf{T}} - \mathbf{T}_e) d\Omega \right]^{1/2} \quad (2.41)$$

where \mathbf{F}_e is the finite element solution for the deformation gradient in element e , \mathbf{T}_e is the finite element solution for the 1st Piola-Kirchoff stress in element e , and $\bar{\mathbf{F}}$ is the L_2 -projection of the finite element solution for \mathbf{F}_e , and $\bar{\mathbf{T}}$ is the L_2 -projection of the finite element solution \mathbf{T}_e . Elements for which the error ϵ_e is greater than some prescribed error tolerance ϵ_A are targeted for refinement.

2.5.3 Mesh Refinement Strategies

There are several ways in which a *FE* mesh may be refined so as to enhance the quality of the interpolation in regions of large discretization error. They include (a) *h-refinement* which introduces new elements of with the interpolation order but of smaller size, with h referring to a linear dimension that characterizes the size of an element. (b) *p-refinement*. which introduces a higher degree interpolation for an element of the same size, with p referring to the polynomial order of the element and (c) *hp-refinement* which refers to a combination of the previous two adaptive strategies. In our study, *h-refinement*, which is known to have superior performance near a singularity [6], will be implemented.

2.6 Refinement

After identifying elements that require interpolation enhancement, refinement is carried out by subdividing the element to one-half the original size. This results in 4 elements for a *2D* problem or 8 elements for a *3D* problem. Such a refinement methodology results in (a) incompatibility of displacement field across element boundaries with different levels of mesh refinement and (b) multiple levels of h refinement for elements in critical regions requiring enhanced deformation fields. The issues are considered next.

2.6.1 2D Refining

When we use an h -adaptive technique, we shall refer to the refinement of an element as fission. This processes are illustrated in figure 2.2. When an element is refined next to an unrefined

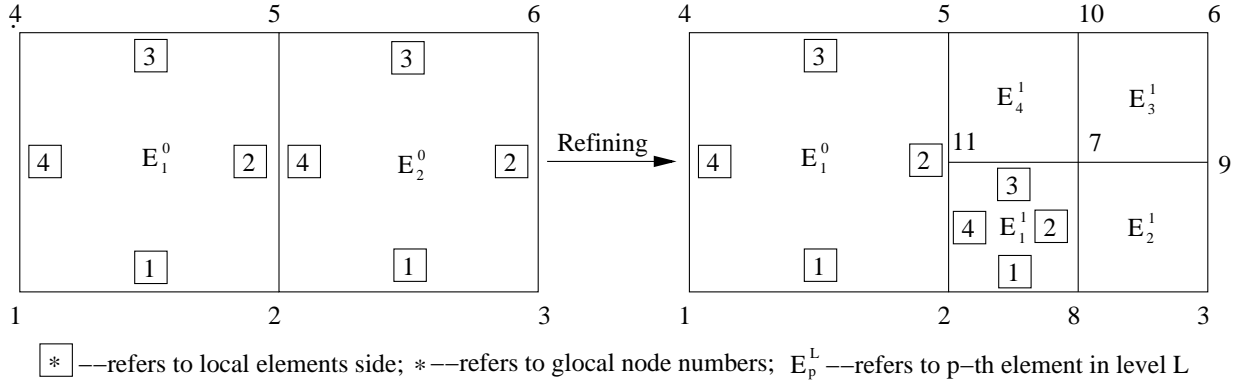


Figure 2.2: A Q4 element refined to four Q4 elements

element, the resulting interpolation is dissimilar across the element boundary. For example, the displacement field along the for h refined element to the right in figure 2.2 is piecewise linear between the corner nodes (1 and 4) and the mid-node (8) at the center of the element side. On the other hand, for the element to the left the displacement field is linear between the corner nodes. In order to ensure a smooth displacement field along such boundaries, the motion of a slave node 8 is governed by the constraint of compatibility written as:

$$\begin{Bmatrix} u_1^8 \\ u_2^8 \end{Bmatrix} = \begin{bmatrix} \frac{1}{2} & 0 & \frac{1}{2} & 0 \\ 0 & \frac{1}{2} & 0 & \frac{1}{2} \end{bmatrix} \begin{Bmatrix} u_1^1 \\ u_2^1 \\ u_1^2 \\ u_2^2 \end{Bmatrix} \quad (2.42)$$

For a FE mesh with multiple levels of refinement, such a scenario is possible along sides at the boundary of any level L (with element sizes $h_L = 2^{-L}h_0$) if they are not part of the domain boundary $\partial\Omega_0$. In these cases the general compatibility constraint of degrees of freedom $\{\mathbf{u}_S\}$ associated with dependent slave nodes are written in terms of those associated with independent master nodes as

$$\{\mathbf{u}_S\} = [\mathbf{T}]\{\mathbf{u}_M\} \quad (2.43)$$

The equations of motion are not evaluated at slave node but instead the nodal forces at slave nodes are added to force at the corresponding master nodes, i.e.

$$\{\mathbf{f}_M\} = \{\mathbf{f}_M\} + [\mathbf{T}]^T\{\mathbf{f}_S\} \quad (2.44)$$

where $\{\mathbf{f}_M\}$ are the nodal forces at slave node and $\{\mathbf{f}_S\}$ are the nodal forces at nodes at the master nodes. This is a standard technique for treating constraints in explicit methods[74]. In order to automatically effect such a process, in a computer program the following *two – level* algorithm is employed:

1. Identify the boundaries associated with elements $E_i^L, i = 1..N_L$ in a particular level L . This is accomplished by noting that an element side is not on an element boundary if

there exists two elements E_1^L, E_2^L in level L with local sides $\boxed{s_1}, \boxed{s_2}$ if

$$\begin{aligned} \text{Global nodes on local side } \boxed{s_1} \text{ of element } E_1^L &= \text{Global nodes on local side } \boxed{s_2} \\ &\text{of element } E_2^L \end{aligned}$$

For example in figure 2.2, local sides $\boxed{1}$ in element E_1^1 is on the boundary of level 1, since the global nodes 2, 8 corresponding to this side are not present in any other element at level 1. Such boundary sides at level L , defined by the pair (s_j, E_i^L) , shall be referred to as bs_k^L .

2. Identify local side, in level $L - 1$, from which the a boundary side bs_k^L was generated in the h -refinement process. For example in figure 2.2, boundary side $bs_1^1 = (s_1, E_1^1)$ in level 1 is derived from side $\boxed{s_1}$ of element E_2^0 in level 0. In the more general case, the boundary side bs_k^L at level L is said to be derived from a boundary side $bs_0_k^L = (s_p, E_q^{L-1})$ in level $L - 1$.
3. If the derived boundary side $bs_0_k^L$ is not on the domain boundary $\partial\Omega_0$, the global nodes M_i corresponding local side $\boxed{s_p}$ in element E_q^{L-1} are the master nodes and all other nodes on the boundary side bs_k^L are the slave nodes S_j with the compatibility constraint for the slave nodes S_i written using equation (2.43).

For multiple levels of refinement (i.e $L = 1, \dots, P$) the h -refinement strategy can be formulated as

1. Assume all global nodes up to level $L - 1$ are either independent or are dependent nodes with compatibility constraint of the form

$$\{\mathbf{u}_{S_j^{L-1}}\} = [\mathbf{T}_j^{L-1}] \{\mathbf{u}_{M_j}\} \quad (2.45)$$

where $[\mathbf{T}_j^{L-1}]$ is the constraint matrix and $\{\mathbf{u}_{M_j^{L-1}}\}$ are the global master nodes for the j -th boundary node in level $L - 1$. Note that all nodes in level 0 are assumed to be independent.

2. Starting from level $L = 1 \dots P$, use the *two-level* algorithm to identify slave node S_j^L at level L with compatibility constraints (w.r.t level $L - 1$) written as

$$\{\mathbf{u}_{S_j^L}\} = [\mathbf{T}_L^{L-1}] \{\mathbf{u}_{M_j^{L-1}}\} \quad (2.46)$$

3. Each of the master nodes, at level $L - 1$, in the set $\{\mathbf{u}_{M_j^{L-1}}\}$ are either (a) independent nodes denoted by q_1, q_2, \dots or (b) dependent nodes denoted by r_1, r_2, \dots with known compatibility constraint matrices $[\mathbf{T}_{r_i}^{L-1}]$. Consequently the previous equation can be rewritten as

$$\begin{aligned} \{\mathbf{u}_{S_j^L}\}_p &= \sum_i [\mathbf{T}_L^{L-1}]_{pq_i} \{\mathbf{u}_{M_j^{L-1}}\}_{q_i} + \sum_i [\mathbf{T}_L^{L-1}]_{pr_i} \{\mathbf{u}_{M_j^{L-1}}\}_{r_i} \\ &= \sum_i [\mathbf{T}_L^{L-1}]_{pq_i} \{\mathbf{u}_{M_j^{L-1}}\}_{q_i} + \sum_i [\mathbf{T}_L^{L-1}]_{pr_i} [\mathbf{T}_{r_i}^{L-1}]_{r_i s} \{\mathbf{u}_{M_{r_i}}\}_s \\ \text{i.e. } \{\mathbf{u}_{S_j^L}\} &= [\mathbf{T}_j^L] \{\mathbf{u}_{M_j}\} \end{aligned} \quad (2.47)$$

where elements of the set $\{\mathbf{u}_{M_j}\}$ comprises of the union of independent and dependent nodes at level $L - 1$, i.e. $\{\mathbf{u}_{M_j}\} = \{\mathbf{u}_{M_j}\}_{q_i} \cup \{\mathbf{u}_{M_j}\}_{r_i}$. If any of the master nodes (at level $L - 1$) $\{\mathbf{u}_{M_j^{L-1}}\}_q$ are themselves slave nodes (with compatibility constraint matrix $[\mathbf{T}]_q^{L-1}$ then rewrite the previous equation as

4. The end result of this algorithm, at level L , is a set of (a) independent nodes (corresponding to non boundary nodes) at level L and (b) dependent slave nodes at level L with known constraint matrix and master nodes. This set can now be recursively used into levels $P > L$.

The following data structures are used to implement the multi-level h -refinement algorithm. If NE and NN are the number of elements and nodes in the system, the nodal and element data for the adaptive process is handled by the following arrays:

1. NOC(J=1..4,NEL=1..NE): the global node number of node J of element NEL;
2. X(K=1..2,NODG=1..NN): the coordinates of global node NODG;
3. ID_ELE(NEL=1..NE)=IDE: the status of element NEL, IDE=1 means the element is active, IDE=0 means the element is inactive(i.e. refined);
4. MAP_GLB(NODG=1..NN)=MAP: Map of global node NODG. MAP>0 means this node is an independent(or master) node and ; MAP<0 means this node is an dependent (or slave) node. The corresponding dependency is stored in array N2N_DEPEND(-MAP,NDP+1) and FACT_DEPEND(-MAP,NDP);
5. N2N_DEPEND(I,1)=NDP: the number of master(or independent) nodes on which Ith slave(or dependent)node depend. This corresponds to the size of the master node vector $\{\mathbf{u}_{M_j^{L-1}}\}$. N2N_DEPEND (I,J=2..NDP+1) and FACT_DEPEND (I,JJ=1..NDP): master node number and corresponding coefficient for the constraint matrix

For the Ith slave node in a $2d$ problem,the constraint matrix can now be regenerated as

$$\begin{Bmatrix} u_1^I \\ u_2^I \end{Bmatrix} = \begin{bmatrix} \alpha_I^1 & 0 & \alpha_I^2 & 0 & \dots & \alpha_I^{NDP} & 0 \\ 0 & \alpha_I^1 & 0 & \alpha_I^2 & \dots & 0 & \alpha_I^{NDP} \end{bmatrix} \begin{Bmatrix} u_1^{M_I^1} \\ u_2^{M_I^1} \\ u_1^{M_I^2} \\ u_2^{M_I^2} \\ \vdots \\ u_1^{M_I^{NDP}} \\ u_2^{M_I^{NDP}} \end{Bmatrix} \quad (2.48)$$

$$\text{i.e. } \{\mathbf{u}_I\} = [\mathbf{T}_I]\{\mathbf{u}_{M_I}\}$$

where $\alpha_I^J = FACT_DEPEND(I, J), M_I^J = N2N_DEPEND(I, J + 1)$. The resulting two-level algorithm for NEN elements in level L shall be referred to as REFINE_L_QC_2D(NEN, L...)

Two-level Refining Level L

Assuming all information at level $L - 1$ is available, the resulting *two - level* algorithm can now be rewritten at level L as

1. Generate side numbers at level $L - 1$ from $NOC(\dots)$ of elements to be refined at level $L - 1$. The sides are stored as $NOC_SIDE(NSI=1..N_SIDES, J=1..2)$ where the node number of end-node J of side NSI is stored in the array $NOC_SIDE(\dots)$.
2. Identify side type using the array $NOC_SIDE(NSI=1..N_SIDES, 3)=NSIDETP$, where (i) $NSIDETP \geq 1$ means side is on original boundary, (ii) $NSIDETP \leq -1$ means side is independent node at level L and (iii) $NSIDETP=0$ means side is dependent (contained in only unique element to be refined)
3. Generate nodes at the center of elements to be refined. Assign $X(J, NODE_ALL)$ and $MAP_GLB(NODE_ALL)$. These nodes are master (or independent) nodes;
4. Generate midway nodes of sides. Assign $X(J, NODE_ALL)$ and $MAP_GLB(NODE_ALL)$. Midway nodes of independent sides are slave nodes; midway nodes of inner sides or sides on original boundary are independent;
5. Generate new elements on level L , generate the element-node-connection array $NOC(J, NEL)$ for these new elements. Initialize $ID_ELE(NEL)$ to zero.

Remarks:

1. In order to identify if a side in element NEL is a new side or an adjacent sides or a boundary side (steps 1&2) the following algorithm is used
 - Define an array $NOC_SIDE_ELE(NSI=1..4, J=1, 2)$ to store two end-nodes numbers of each of the four sides of the element to be refined. Each of these local sides ($NSI = 1 \dots 4$) is identified as an adjacent side if and only if the two end-nodes can be found in some predefined side $LSIDE$, i.e if $NOC_SIDE_ELE(NSI, \dots) = NOC_SIDE(LSIDE, \dots)$ for some $LSIDE = 1 \dots NSIDE$. If such a $LSIDE$ can be found set $NOC_SIDE(LSIDE, J = 3) = -1$.
 - If local side NSI is not an adjacent side increment $NSIDE$ by 1 and store $NOC_SIDE(NSIDE, \dots) = NOC_SIDE_ELE(NSI, \dots)$. Next identify if the new side is on the original boundary at level $L - 1$. If so $NOC_SIDE(N_SIDES, J = 3) = 1$ otherwise $NOC_SIDE(N_SIDES, J = 3) = 0$
2. In step 4), the midway node number of side NSI are stored in array $NOC_SIDE(NSI, 4)$. If the side is on the original boundary, this midway node needs to be identified as a displacement boundary node or a traction boundary node.

In order to clarify the above refining algorithm, let us consider a simple tension case in figure(2.3) with four elements and nine nodes at original (level 0) mesh. Assume we need refine elements two and four in original mesh. The arrays for sides is given in table(2.1). The first thing to note is eight boundary sides in original mesh ($NSIDE_BD=8$).This is stored in the array

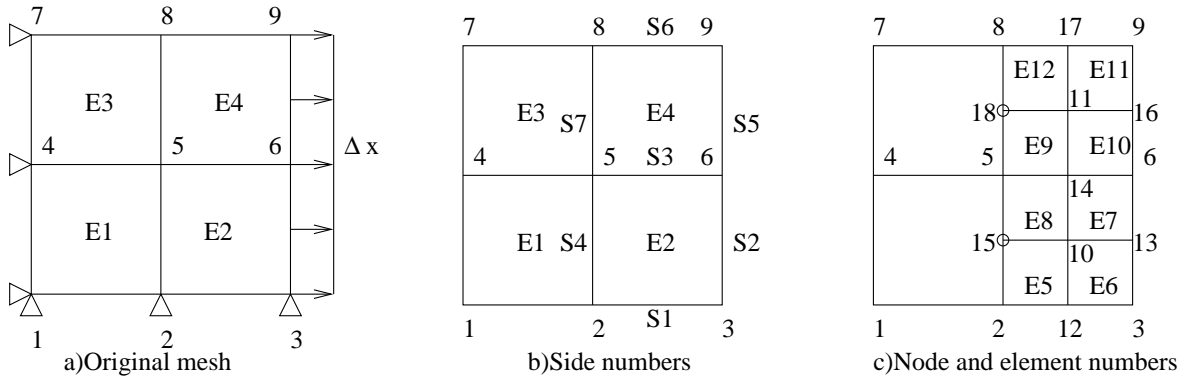


Figure 2.3: Refining of one level

$LIST_BD_SIDE(1..8)$ is $\{1, 4, 5, 6, 11, 12, 14, 15\}$. It is obvious that side $S1$, $S2$, $S5$ and $S6$ (corresponding global side numbers 5, 6, 14, 15 respectively) are on the original boundary. Side $S3$ is a common side because it shows up in both $NUM_SIDE(1, 1..4) = 1, 2, 3, 4$ and $NUM_SIDE(2, 1..4) = 3, 5, 6, 7$. On the other hand, sides $S4$ and $S7$ are dependent sides. The new $LIST_BD_SIDE(1..8)$ becomes $\{17, 21, 22, 26, 38, 42, 43, 47\}$. After numbering the centers of element two and four as node ten and eleven, respectively, we assign number to midway nodes of sides and corresponding $MAP_GLB()$. With the above information at hand, we can generate the eight new elements(5 12) on level 1 for which nodes 15 and 18 are slave (dependent) nodes. Their dependency are $N2N_DEPEND(1, 1..3) = 1, 2, 5$, $FACT_DEPEND(1, 1..2) = 0.5, 0.5$ and $N2N_DEPEND(2, 1..3) = 1, 5, 8$ and $FACT_DEPEND(2, 1..2) = 0.5, 0.5$ respectively.

In the original mesh, there are nine displacement boundary conditions (DBC) and corresponding degree of freedom (DOF) and displacement are $\{2, 4, 6, 1, 7, 13, 5, 11, 17\}$. After refinement, there are twelve DBC and corresponding DOF are $\{2, 4, 6, 1, 7, 13, 5, 11, 17, 24, 25, 29\}$.

Table 2.1: Array for sides used to describe $2d$ mesh refinement

| | | | | | | | |
|---------------------------|----|----|----|----|----|----|----|
| <i>Side number</i> | 1 | 2 | 3 | 4 | 5 | 6 | 7 |
| <i>Side type</i> | 1 | 1 | -1 | 0 | 1 | 1 | 0 |
| <i>Midway node number</i> | 12 | 13 | 14 | 15 | 16 | 17 | 18 |
| <i>MAP_GLB()</i> | 12 | 13 | 14 | -1 | 15 | 16 | -2 |

Multi-level Refinement Algorithm

An essential part of the refinement strategy is that, in order to satisfy continuity over the boundaries of elements, some nodes to be constrained(dependent on other nodes). The methodology used to describe this dependency and the generation of the resulting element nodal force vector and stiffness matrices that reflect these constraints is discussed next.

When the level of a neighbor of an element is different from the level of the element, then the element has a dependent node on that side. In $2d$ refining, a midway node of a side is dependent when the side is neither on original boundary nor shared by two elements to be refined, i.e. if

$NOC_SIDE(LSIDE, 3) = -1$. As mentioned previously, a slave midway node of a dependent side can be generated as a uniform partitioning of slave-node effect between the two end-nodes in the previous level. If the end-node at the previous level is itself a slave node, then its dependency needs to be substituted into set of independent nodes and corresponding dependency at the current level. For instance, in figure 2.3, if the two end-nodes are 15 and 10, then the dependency of midway node I is $N2N_DEPEND(I, 1..4) = 1, 2, 5, 10$, $FACT_DEPEND(1, 1..3) = 0.25, 0.25, 0.5$.

As noted before the multi-level refining process starts from the lowest level to and proceeds to the highest level. Some of the data structures used to handle the multiple levels include

1. $NE_LVL(P, 1)$ the total number of all elements (active and inactive) elements on Level P
 $NE_LVL(P, 2)=NE2REF$ is the the number of elements to be refined on Level P.
2. $NO_LVL_REF(P, J=1..NE2REF)$ denotes the Jth element number (locally for a given level P) to be refined in level P.
3. $JDIAG_ELE(P)$ denotes the 1st element number (global) on level P.
4. $JDIAG_NALL(P)$ denotes the 1st node(including dependent and independent)number on level P.
5. $JDIAG_NGLB(P)$ denotes the 1st independent node number on level P.
6. $JDIAG_NDP(P)$ denotes the 1st dependent node number on level P.

With the two-level h -refinement algorithm at hand, the multi-level refining algorithm proceeds as follows

```
DO L=1, LVL_MAX-1
CALL REFINE_L_QC_2D(NEN, L...)
ENDDO
```

Multi-step Algorithm

In a nonlinear setting, mesh refinements may be required at different stages of the loading process. After error estimation at a particular stage (or step) of the loading process, new elements to be refined at various levels of the current mesh are identified. The new FE mesh can now be obtained by including these new elements to array $NO_LVL_REF(P, J = 1..NE2REF)$. The new array $NO_LVL_REF(P, J = 1..NE2REF)$ in conjunction with the multi-level algorithm in the previous step generates the new FE mesh at the current step. It should also be noted that any new refinement at an intermediate step will require the require an update of the global displacement vector $\{\mathbf{D}\}$ at the beginning of the current step. This is accomplished by noting that new independent nodes generated at the current step were part of unrefined elements at the end of the previous step. The corresponding displacement values (of new independent nodes) can be obtained by interpolating the values (from unrefined elements) at the end of the last step.

Nodal Force Vector and Element Stiff Matrix

At the end of the refinement process, the geometry of the active elements, their connectivity and therefore their geometry are known. Given a global displacement vector $\{\mathbf{D}\}$, the corresponding element values of the displacement vector $\{\mathbf{d}\}$ can be calculated through (i) equation (2.48) for dependent nodes or (ii) directly from $\{\mathbf{D}\}$ for independent nodes. Given the element geometry and element displacement vectors, the residual element force vectors and element stiffness matrices can now be obtained in the usual way. These vectors/matrices correspond to non-constrained conditions. In order to reflect the dependency, these vectors/matrices need to be rewritten in terms of independent degrees of freedom. If each DOF in the element displacement vector is subdivided into independent nodes q_i and dependent nodes r_i (with associated master *DOF* $\{\mathbf{u}_{M_{r_i}}\}$ and constraint matrices $[\mathbf{T}_{r_i}]$), then the element displacement vector itself can be rewritten as

$$\begin{aligned} \{\mathbf{d}\} &= \begin{Bmatrix} u_1^{q1} \\ u_2^{q2} \\ \dots \\ u_1^{r1} \\ u_2^{r1} \\ \vdots \end{Bmatrix} = \begin{Bmatrix} u_1^{q1} \\ u_2^{q2} \\ \vdots \\ \sum_i \{\mathbf{T}_{r_1}\}_{1i} \{\mathbf{u}_{M_{r_1}}\}_i \\ \sum_i \{\mathbf{T}_{r_1}\}_{1i} \{\mathbf{u}_{M_{r_1}}\}_i \\ \vdots \end{Bmatrix} \\ &= [\mathbf{\Gamma}_e^*] \begin{Bmatrix} u_1^{q1} \\ u_2^{q2} \\ \vdots \\ \{\mathbf{u}_{M_{r_1}}\}_1 \\ \{\mathbf{u}_{M_{r_1}}\}_2 \\ \vdots \end{Bmatrix} = [\mathbf{\Gamma}_e^*] [\mathbf{\Gamma}_e] \{\mathbf{d}^*\} = [\mathbf{\Gamma}_e] \{\mathbf{D}\} \end{aligned} \quad (2.49)$$

where $[\mathbf{\Gamma}_e^*]$ is the transformation matrix associated with local independent *DOF* $\{\mathbf{d}^*\}$ in element e . The resulting transformation matrix $[\mathbf{\Gamma}_e]$, w.r.t global DOF $\{\mathbf{D}\}$ can now be used in conjunction with the the solution scheme outline in section 2.4 to proceed to the next iteration.

For example, consider element $E5$ in figure 2.3. Quite clearly the slave node 15 (local node 4) is equally dependent on master nodes 2 and 5 which will be deduced through the multi-level h -refinement algorithm outlined in the previous section. Thus the local element transformation matrix $[\mathbf{\Gamma}_e^*]$ and local independent displacement vector $\{\mathbf{d}^*\}$ for $E5$ can be written as

$$[\mathbf{\Gamma}_e^*] = \begin{bmatrix} 1 & 0 & 0 & 0 & 0 & 0 & 0 & 0 \\ 0 & 1 & 0 & 0 & 0 & 0 & 0 & 0 \\ 0 & 0 & 1 & 0 & 0 & 0 & 0 & 0 \\ 0 & 0 & 0 & 1 & 0 & 0 & 0 & 0 \\ 0 & 0 & 0 & 0 & 1 & 0 & 0 & 0 \\ 0 & 0 & 0 & 0 & 0 & 1 & 0 & 0 \\ 0.5 & 0 & 0 & 0 & 0 & 0 & 0.5 & 0 \\ 0 & 0.5 & 0 & 0 & 0 & 0 & 0 & 0.5 \end{bmatrix}, \{\mathbf{d}^*\} = \begin{Bmatrix} u_1^2 \\ u_2^2 \\ u_1^{12} \\ u_1^{12} \\ u_2^{12} \\ u_1^{10} \\ u_2^{10} \\ u_1^5 \\ u_2^5 \end{Bmatrix} \quad (2.50)$$

The resulting global element transformation matrix $[\mathbf{\Gamma}_e]$ can be obtained by noting that

$$\begin{aligned} \{\mathbf{d}^*\} &= [\boldsymbol{\gamma}]\{\mathbf{D}\} \text{ with } \gamma_{ij} = \begin{cases} 1 & \text{if } \{\mathbf{d}^*\}_i = \{\mathbf{D}\}_j \\ 0 & \text{otherwise} \end{cases} \Rightarrow \\ [\mathbf{\Gamma}_e] &= [\mathbf{\Gamma}_e^*][\boldsymbol{\gamma}] \end{aligned} \quad (2.51)$$

Frame of the h -refinement Algorithm

1. Starting from step=1 \cdots Total # of steps
2. Call a nonlinear solver(Quasi-Newton) to get the equilibrium configuration of the system subject to the new load step
3. Automatic adaption—all elements in the mesh satisfying the refinement criterion are refined, i.e. divided into smaller elements
4. If elements have been in the adaption phase, recover the state of these new elements till the end of previous step. In this case return to (2) to obtain new solution
5. Output—update total displacement of elements and write down step-incremental displacement of elements
6. Proceed to (1) for next load step

Numerical Example

To demonstrate the steps involved in the adaptive methodology consider the problem depicted in figure 2.4. Here a virtual point indenter, infinite in the out-of-plane direction, is pressed into the free surface of a thin film described as a linear elastic material. The Young's Modulus is $1000Pa$ and the Poisson ratio is 0.3. The strain energy error indicator is defined as relative strain energy error density, i.e. strain energy error density divided by system average energy density. The evolution of strain energy error is given in figure 2.5. The convergence of first Piola-Kirchhoff stress is given in figure 2.6. The strain energy error indicator cutoff is 1% for this adaptive refinement. In other words, elements with strain energy error indicator larger than 1% are refining targets.

To study the effect of different energy error indicator cutoff, 2% and 0.5% are taken for the same problem. The meshes after three times refining and corresponding stress distribution are presented in figure 2.7 and 2.8, respectively. From the above figures, we can see that 1% energy error indicator cutoff is appropriate for this problem. To test the adaptive refinement algorithm for irregular meshes, an irregular initial mesh (figure 2.9) was taken as the starting point of the computational model. The corresponding mesh and stress distribution, after the adaptive refinement process, are given in figure 2.9 and 2.10. The results are very close to those with regular initial mesh and establish the efficacy of the adaptive strategy used in this dissertation.

From the above example it can be concluded that the adaptive refining methodology works as expected with the mesh refinement algorithm automatically delineating regions of severe deformation. The adaptive methodology also produces a near continuous stress field as the level of mesh refinement is enhanced.

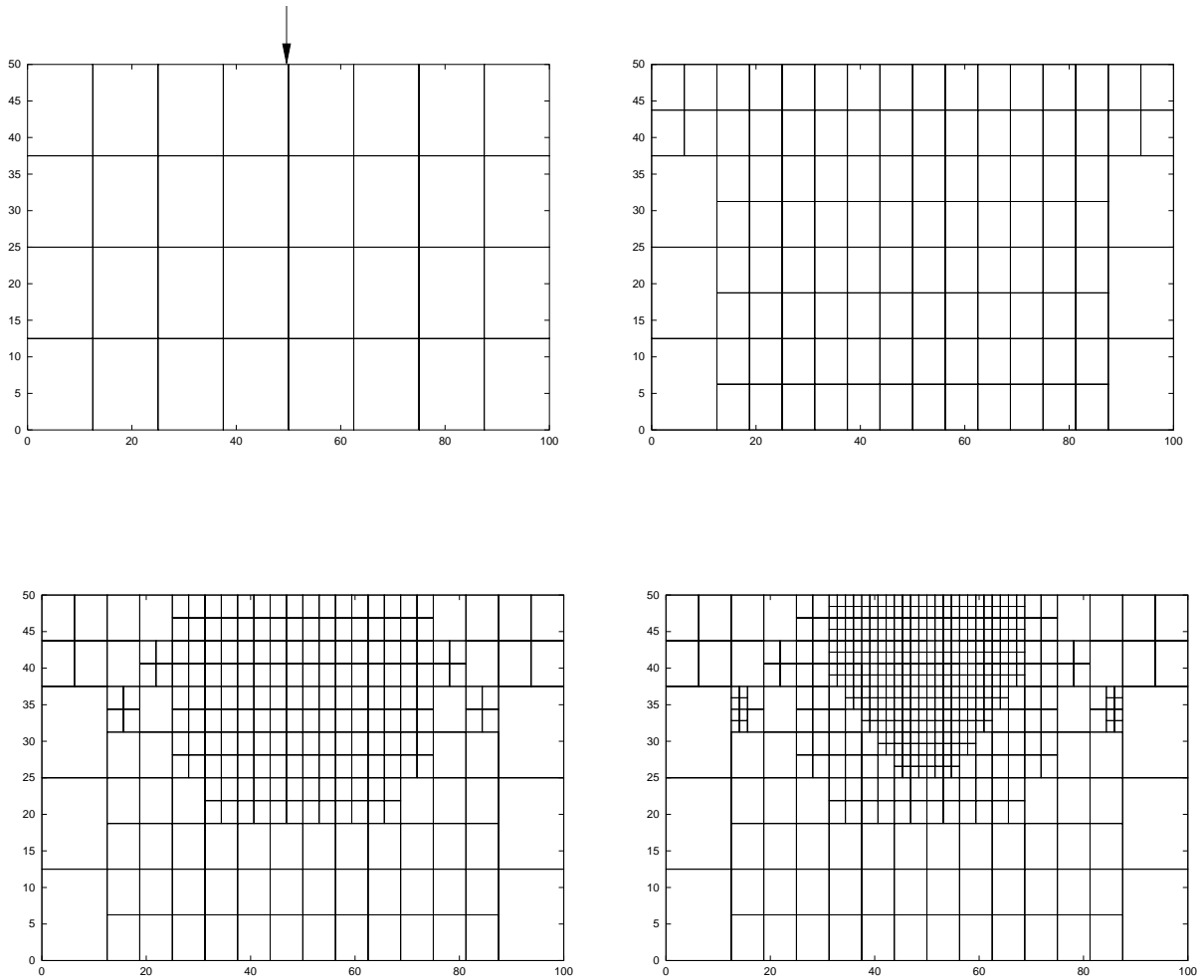


Figure 2.4: Series of mesh refinements generated by adaptive strategy

2.6.2 3D Refining

The process used for 3D refining is illustrated in figure 2.11.

The algorithm for three dimensional refining is similar to that for 2D case outlined in the previous section. Some of the new features in 3D refining include (i) the number of DOFs and coordinates per node changes to three (from two) and (ii) number of nodes per element becomes eight (from four). Some other changes come from the fact that three dimension elements share not only common sides but also common surfaces.

Multi Level Refining in 3D

In three dimensions, an element consists of six surfaces and each surface consists of four side. The processing of three dimension refinement is accomplished in the following steps

1. Generate side numbers and surface numbers. These sides and surfaces come from elements to be refined.

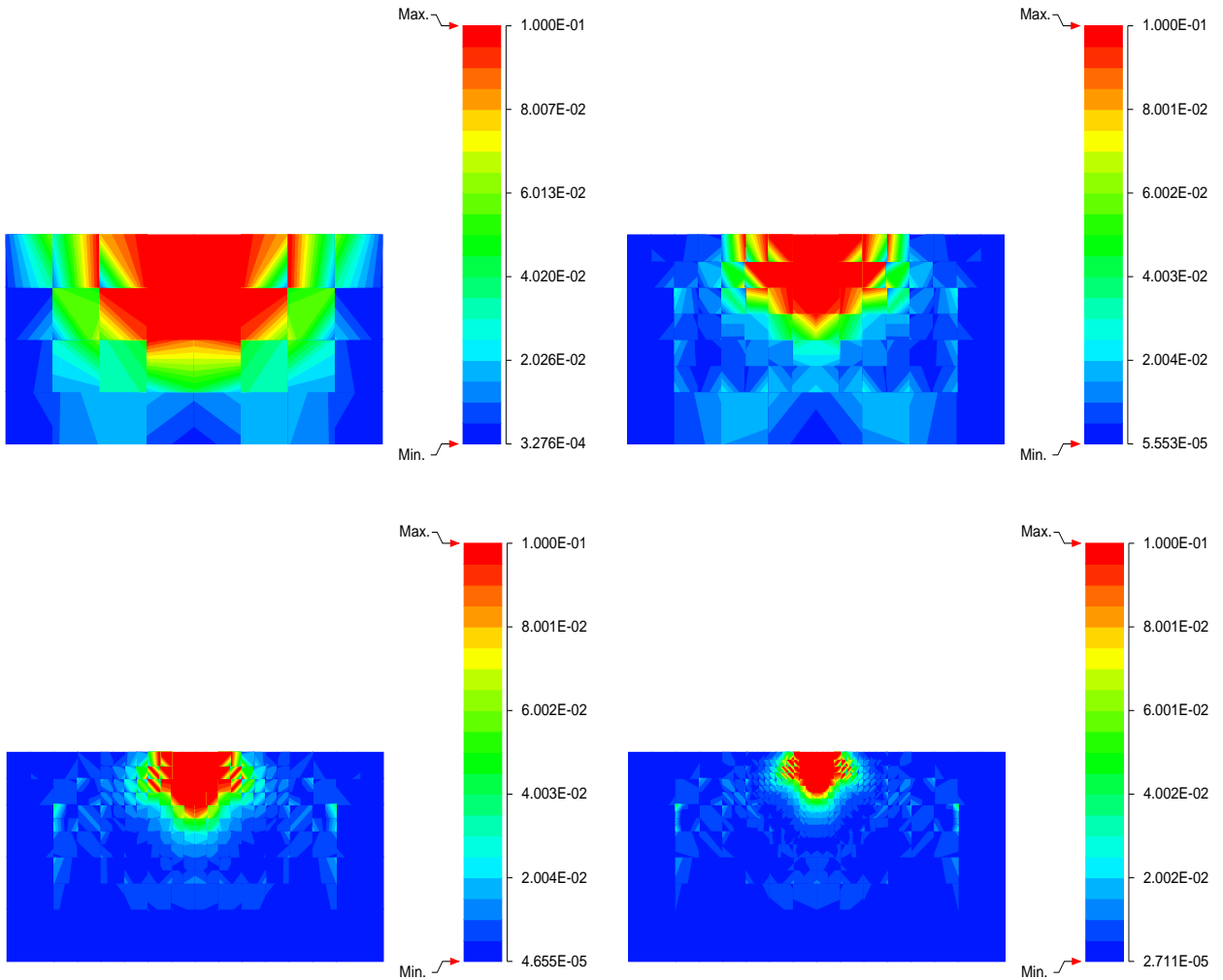


Figure 2.5: Evolution of strain energy error indicator for a sample $2d$ problem

`NOC_SIDE(NSI=1..N_SIDES, J=1..2)`:the node number of end-node J of side NSI .

`NSIDE_2SURF(NSU=1..N_SURFS, J=1..4)`:the side number of side J of surface NSU .

2. Identify surface type, results are stored in array
`NSIDE_2SURF(NSU=1..N_SURFSS, 5)=NSURFTP`, $NSURFTP \geq 1$ means side is on original boundary; $NSURFTP \leq -1$ means side is inner(or common, shared by two elements to be refined); $NSURFTP=0$ means side is dependent(contained in only unique element to be refined);
3. Identify side type, results are stored in array
`NOC_SIDE(NSI=1..N_SIDES, 3)=NSIDETP`, $NSIDETP \geq 1$ means side is on original boundary(type A); $NSIDETP \leq -1$ means side is inner(or common, shared by four elements to be refined)(type B); $NSIDETP=0$ means side is dependent(contained in only unique element to be refined)(type C);

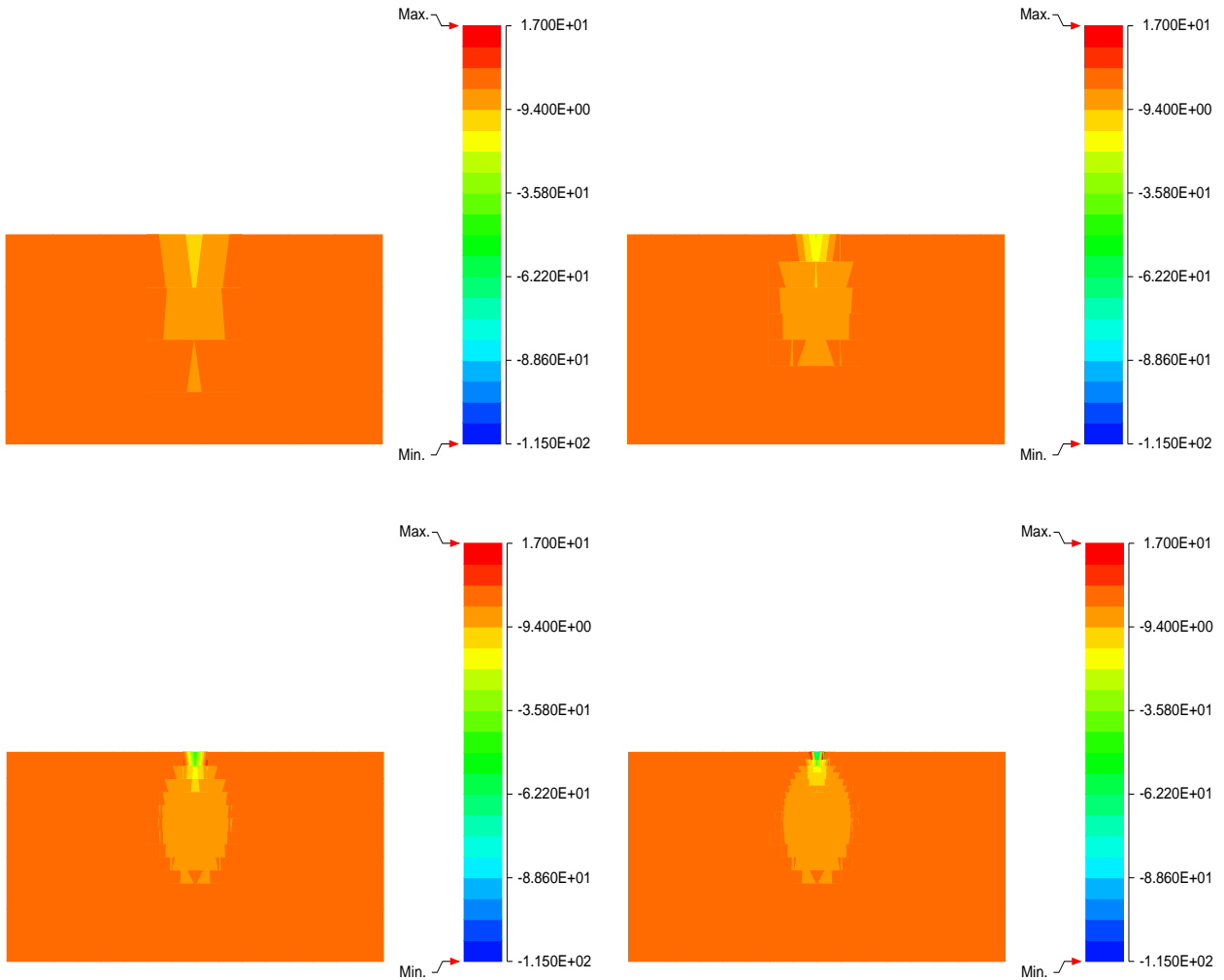


Figure 2.6: Convergence of first Piola-Kirchhoff stress T_{22} (in Pa) for the sample 2D problem

4. Generate nodes at the center of elements to be refined. Assign $X(J, \text{NODE_ALL})$ and $\text{MAP_GLB}(\text{NODE_ALL})$. These nodes are master (or independent) nodes;
5. Generate center nodes of surfaces. Assign $X(J, \text{NODE_ALL})$ and $\text{MAP_GLB}(\text{NODE_ALL})$. Center nodes of independent surfaces are slave nodes; center nodes of inner surfaces or surfaces on original boundary are independent;
6. Generate midway nodes of sides. Assign $X(J, \text{NODE_ALL})$ and $\text{MAP_GLB}(\text{NODE_ALL})$. Midway nodes of independent sides are slave nodes; midway nodes of inner sides or sides on original boundary are independent;
7. Generate new elements on level $L+1$, generate the element-node-connection array: $\text{NOC}(J, \text{NEL})$ for these new elements. Initialize $\text{ID_ELE}(\text{NEL})$ to zero.

Remarks: In step one, we first define an array $\text{NOC_SIDE_ELE}(\text{NSI}=1..12, J=1, 2)$ to store two end-nodes number of four sides for each element to be refined. In subroutine IDEN-

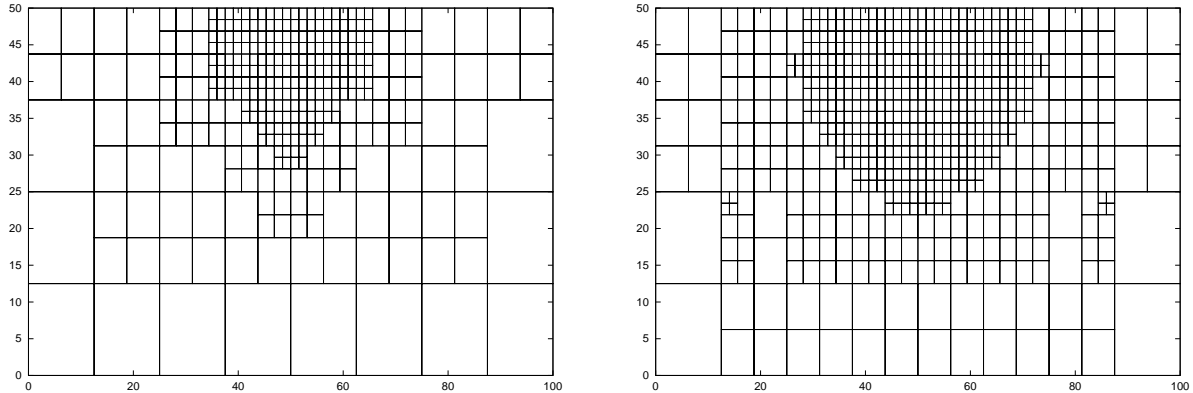


Figure 2.7: Meshes of three levels refinement for different strain energy error indicator cutoff: 2%(left) and 0.5%(right)

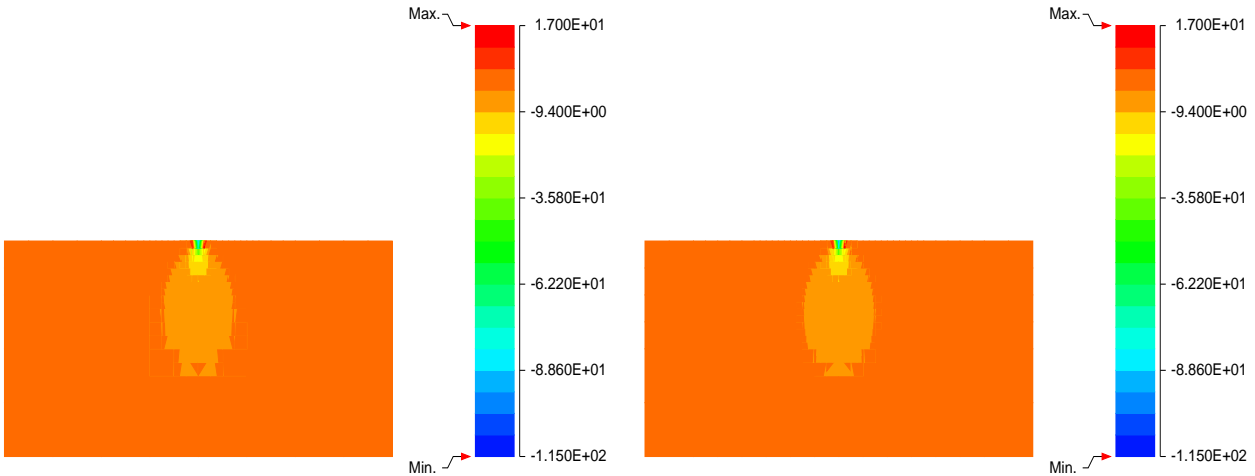


Figure 2.8: First Piola-Kirchoff stress T_{22} (in Pa) for different strain energy error indicator cutoff: 2%(left) and 0.5%(right)

TIFY_SIDES(..) we can use the above information to decide whether two sides are identical. Similarly, we define an array NOC_SURF_ELE(NSI=1..6, J=1, 4) to store four side numbers of six surfaces for each element to be refined. In subroutine IDENTIFY_SURFS(..) we can use them to decide whether two surfaces are identical. If and only if the four sides are identical, the two surface on the same level are identical. What's more, we can indicate these common surfaces. Then we store the six side numbers in array NUM_SURF(NR, J=1..6) for element(to be refined) NR.

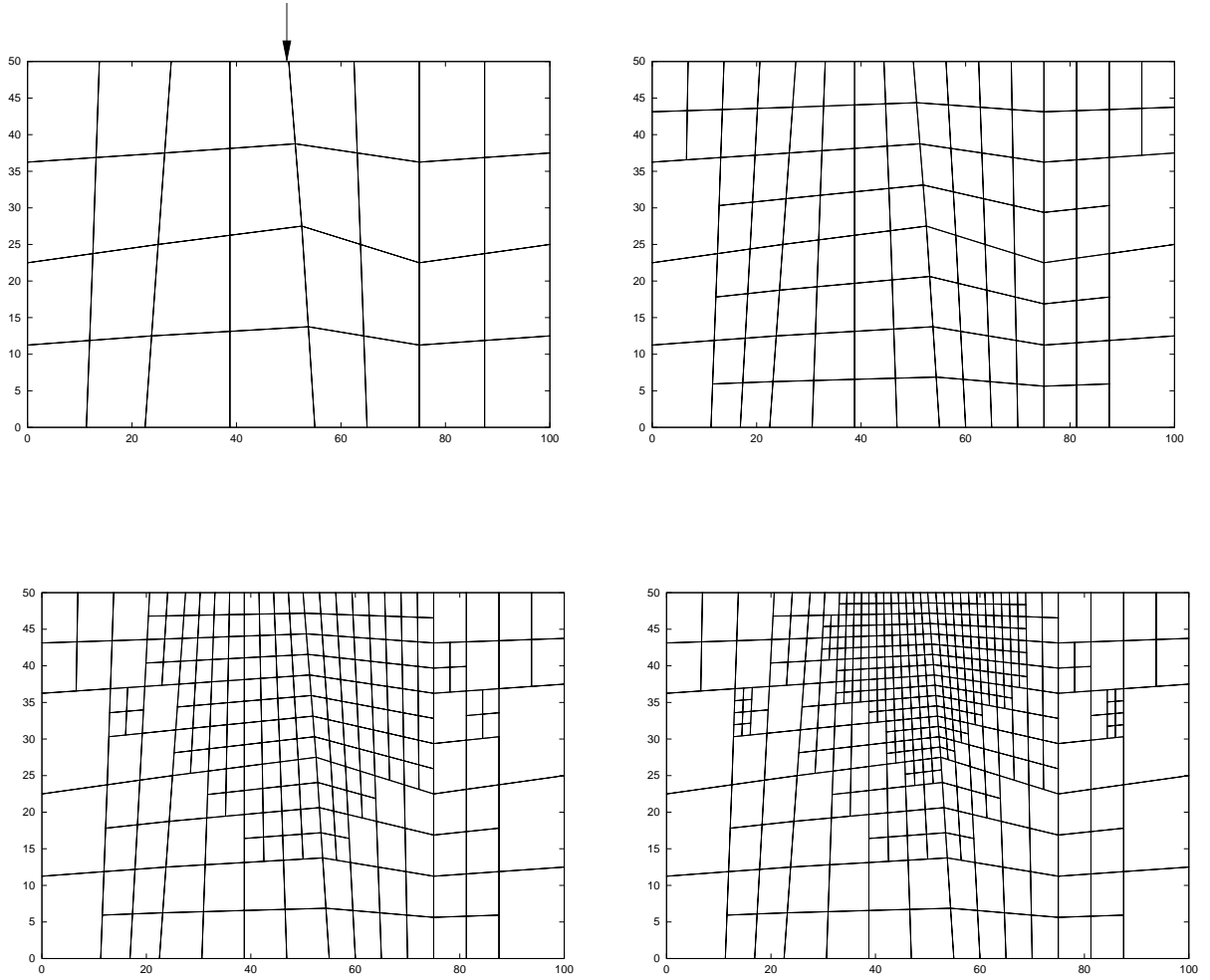


Figure 2.9: Series of mesh refinements generated by adaptive strategy with irregular initial mesh

In step two, array `LIST_BD_SURF(J=1..NSURF_BD)` stores the global number of surfaces on original boundary, where `NSURF_BD` is the number of surfaces on original boundary. The global number of surface `J` in element `NE_ALL1` is $(NE_ALL1-1)*6+J$. By scanning element by element, we can isolate surfaces on original boundary. The remaining surfaces, neither common surfaces nor surfaces on original boundary, are dependent surfaces. At the end this step, `NSURF_BD` and `LIST_BD_SURF(J=1..NSURF_BD)` are updated.

In step three, we first generate a node set `D` which consists of all nodes on dependent surfaces(surface type `C`). We set all `NOC_SIDE(NS,3) = -1` to initialize all sides as inner sides. Then we set all sides contained in surfaces type `A` or `C` are sides on original boundary by setting their `NOC_SIDE(NS,3) = 1`. Obviously, the sides that both end-nodes contained in node set `D` are dependent sides. Finally, the rest are really on original boundary.

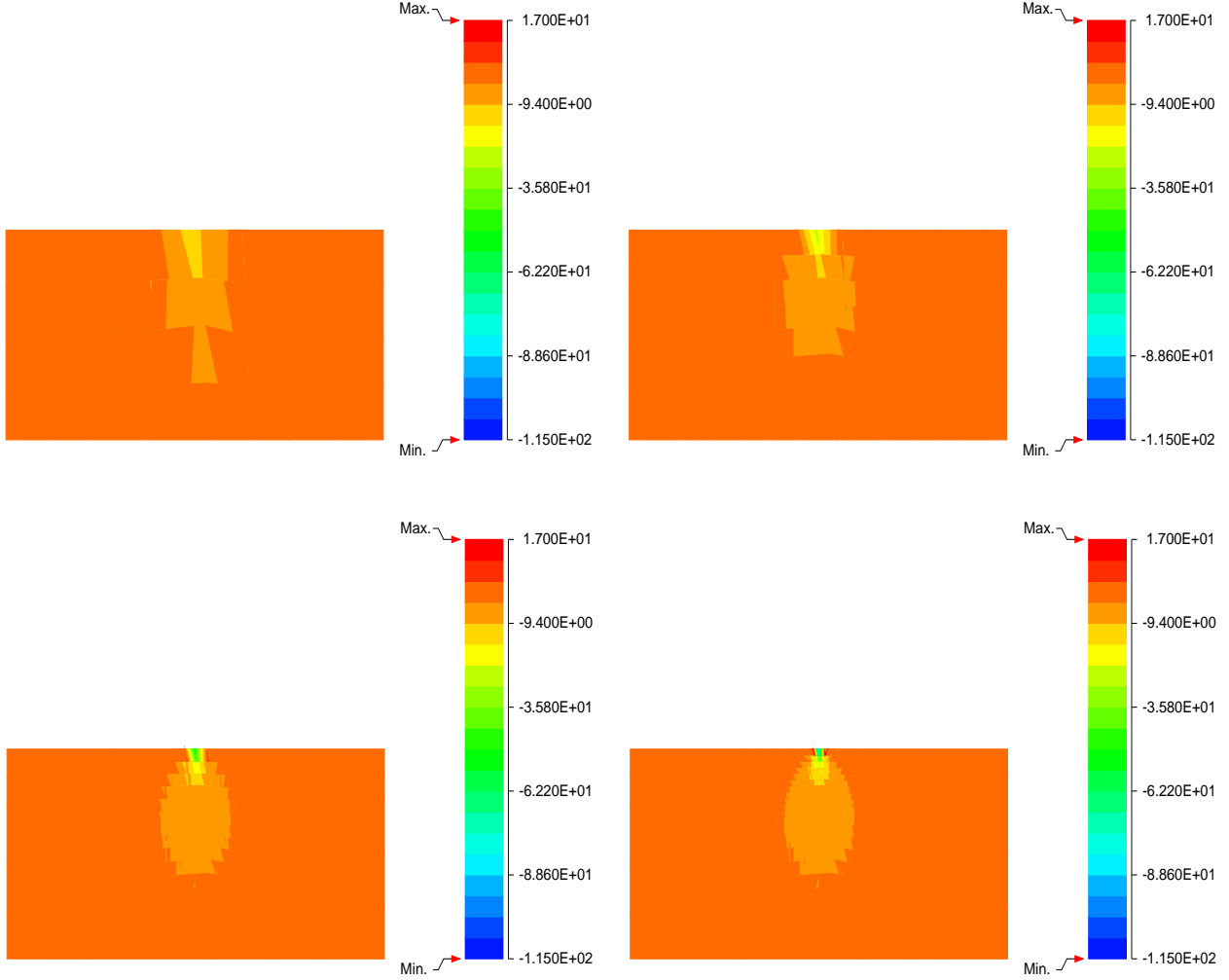


Figure 2.10: Convergence of first Piola-Kirchhoff stress T_{22} (in Pa) with irregular initial mesh

In step five, the center node number of surface NSU are stored in array NSIDE_SURF(NSU, 5). If the surface is on original boundary, we need check whether there are same displacement boundary condition on the four apex-nodes of the surface. If yes, then the midway node bears same displacement boundary condition. If the surface is dependent, we need generate the dependency of this center node from the information of four apex-nodes. We can handle the displacement boundary condition and dependency for midway side nodes similarly in step six.

Numerical Example

To demonstrate the steps involved in the adaptive methodology consider the problem depicted in figure 2.12. Here a virtual point indenter, is pressed into the free surface of a cubic block. The convergence of first Piola-Kirchhoff stress is given in figure 2.13. To test the adaptive algorithm for an irregular mesh, an irregular initial mesh figure 2.14 was taken as the starting point of

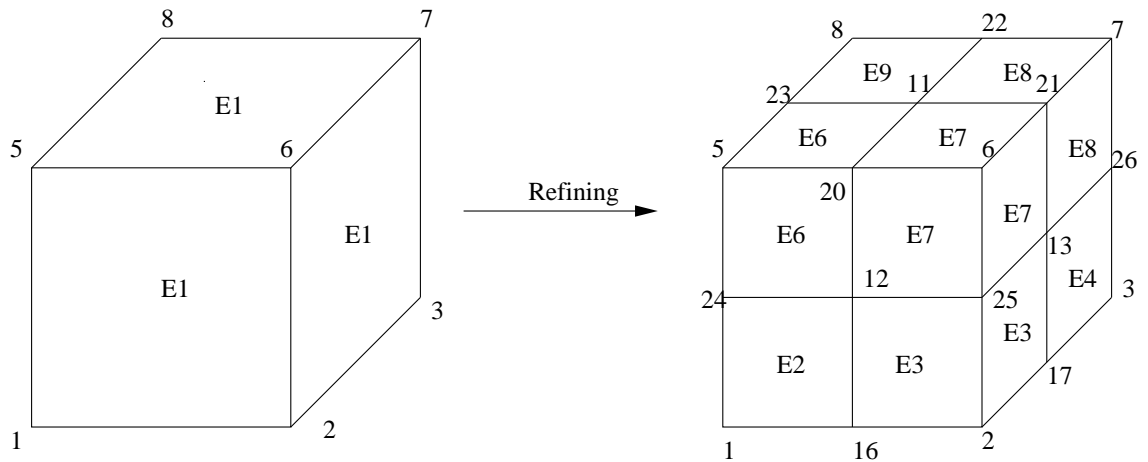
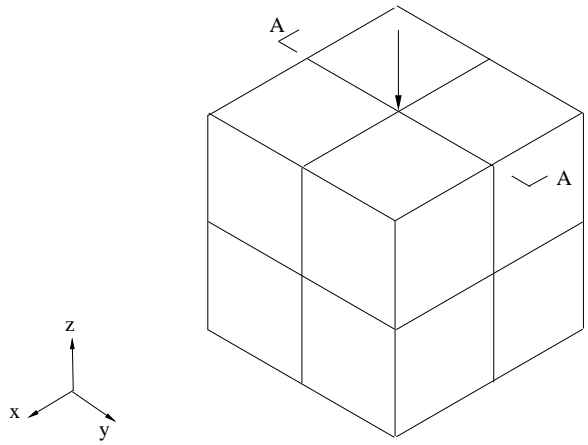


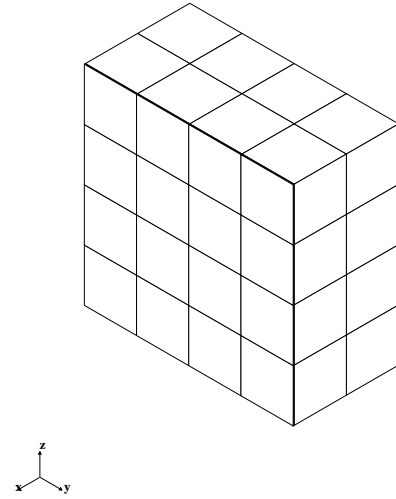
Figure 2.11: A H8 element refined to eight H8 elements

the computational experiment. The corresponding mesh and stress distribution were given in figure 2.14 and 2.15. The results are very close to those with regular initial mesh and effectively demonstrate the ability of the current mesh refinement algorithm to reproduced converged results from different starting points.

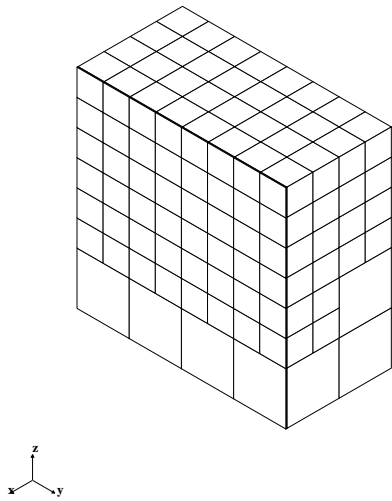
Once again the adaptive refining methodology works as expected with the mesh refinement algorithm automatically delineating regions of severe deformation. The adaptive methodology also produces a near continuous stress field as the level of mesh refinement is enhanced.



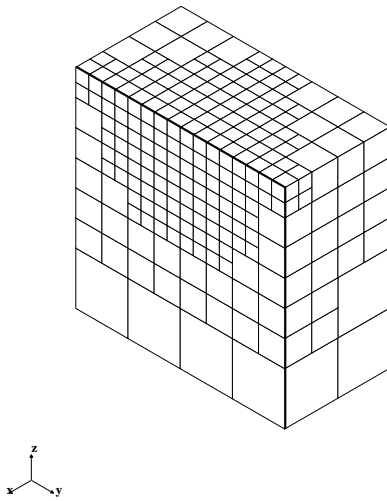
(a) Original mesh



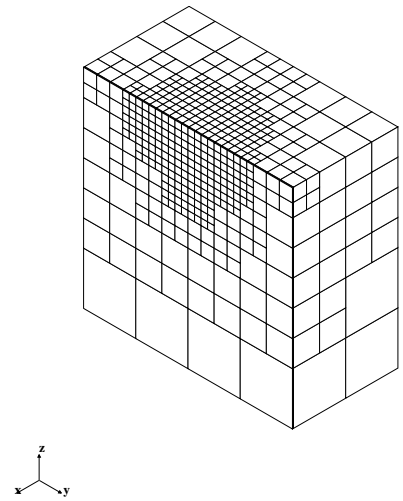
(b) A-A section(2 levels)



(c) A-A section(3 levels)



(d) A-A section(4 levels)



(e) A-A section(5 levels)

Figure 2.12: Automatic adaption process in three dimension refining

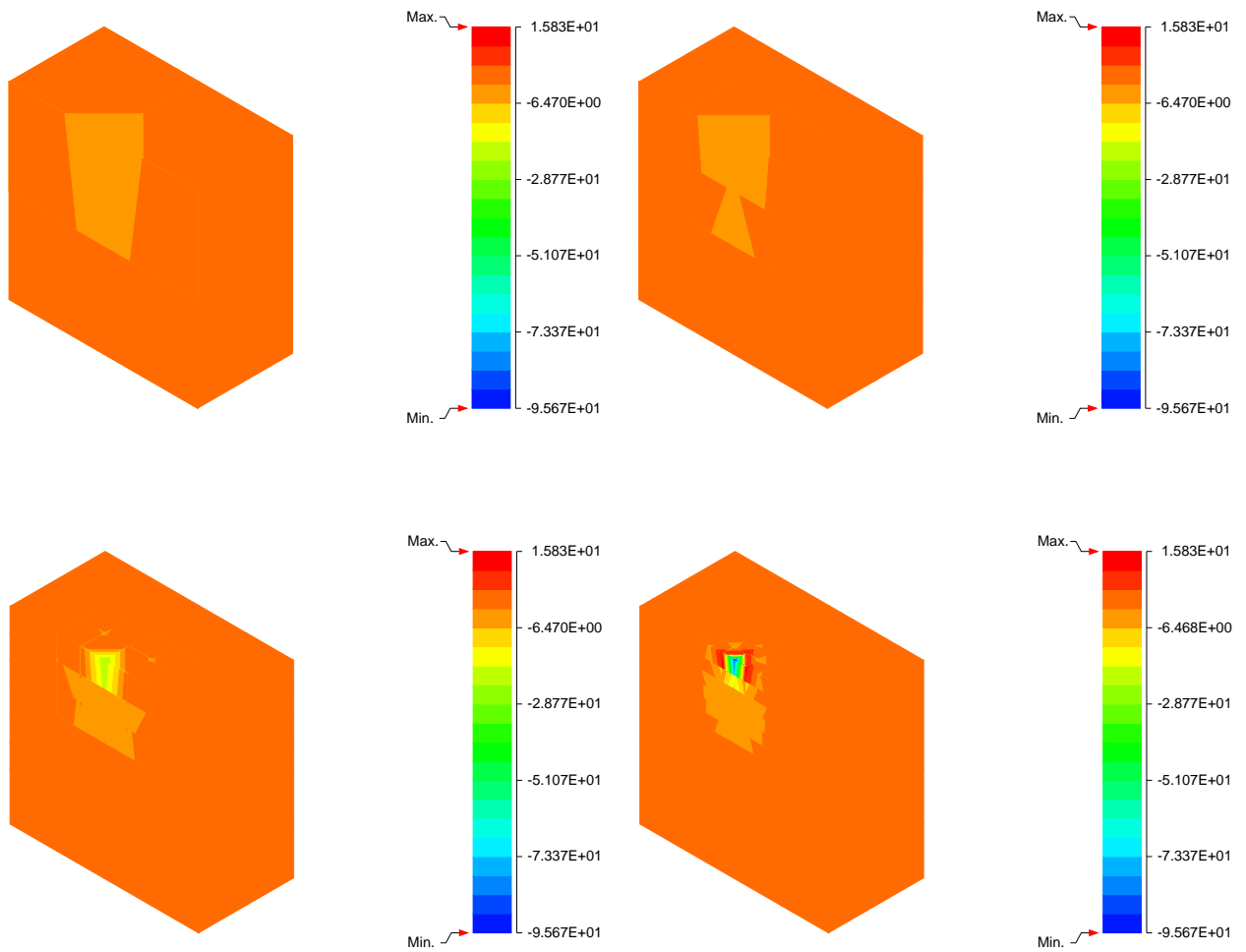
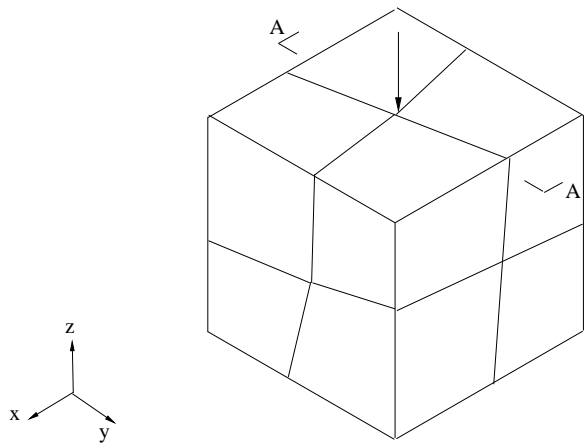
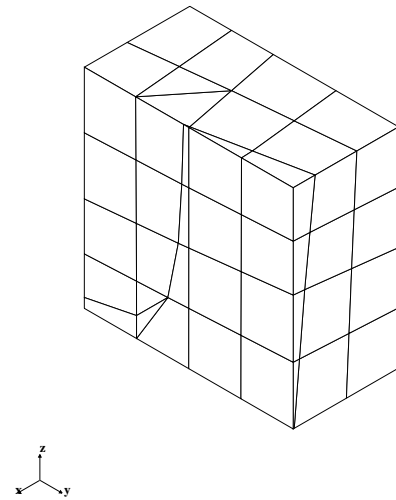


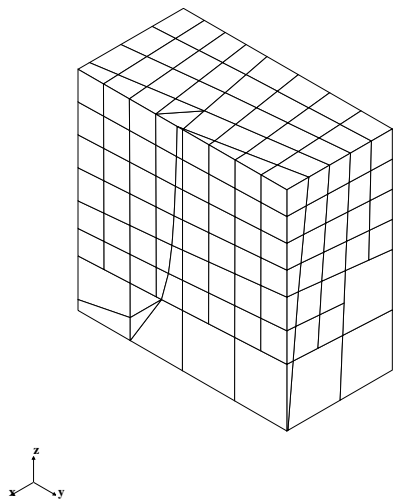
Figure 2.13: Convergence of first piola-Kirchhoff stress T_{33} (in Pa) for the sample 3d problem



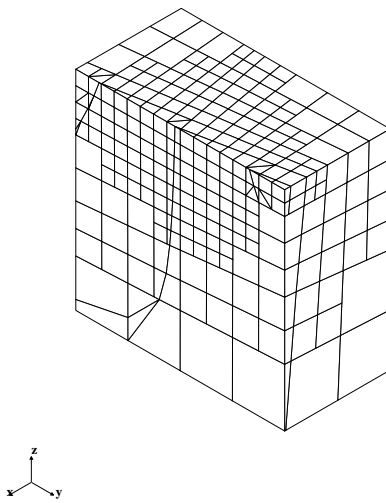
(a) Original mesh



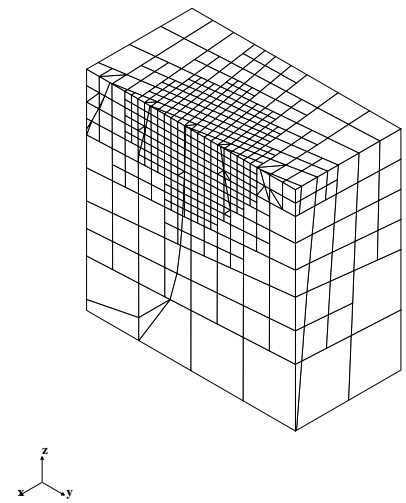
(b) A-A section(2 levels)



(c) A-A section(3 levels)



(d) A-A section(4 levels)



(e) A-A section(5 levels)

Figure 2.14: Automatic adaption process in three dimension refining with irregular initial mesh

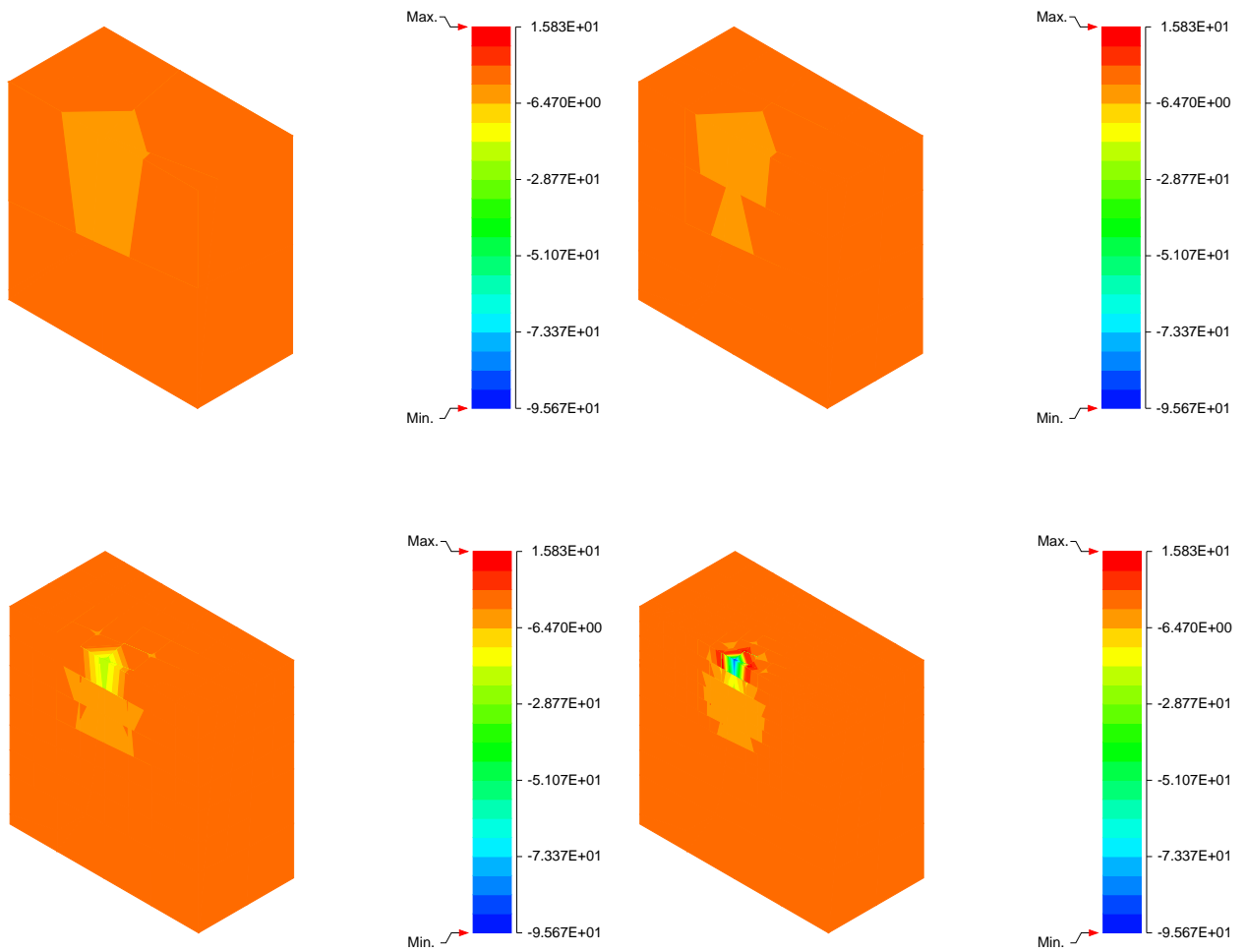


Figure 2.15: Convergence of first Piola-Kirchhoff stress T_{33} (in Pa) with irregular initial mesh

Chapter 3

Atomistic Calculation of Potentials for Coarse/Fine Scale Problems

In this chapter, the generation of the material constitutive property with underlying atomistic crystalline microstructure and a computational methodology to handle possible breakdown of continuum assumption are discussed. The chapter begins with a brief overview of atomistic models used for single crystal metals and its utility in deriving a continuum-scale material model. This is followed by the development of a computational model which uses continuum+atomistic descriptions of material behavior in different regions of the domain. Finally an extension of the computational model, for finite temperatures is presented.

3.1 Introduction

In Quantum mechanical total energy calculations, the energy of the system is a function of the collective atomistic coordinates. Partial derivatives of the total energy with respect to an individual nuclear coordinate result in the force on the desired atom. The quantum mechanical calculations, while very accurate, do not partition the total energy into energies on a per-atom basis. Therefore it is computationally expensive to treat the system with a huge number of atoms. On the other hand, the classical interatomic potentials, are semi-empirically approximate and admit decomposition of the total energy of the system into a sum of the energies of individual atoms. Specifically, the total atomic energy, E_{tot} , when obtained from classical potentials, is presented as

$$E_{tot} = \sum_i E_i \quad (3.1)$$

where E_i is the energy of the i th atom.

The embedded-atom method (*EAM*) [20] and Stillinger-Weber(*SW*) [88] are the two most widely used classical inter-atomic potentials. In both cases, the energy is decomposed as sum of individual atom energies. The *EAM* constitutive law for atom energy includes, aside from pair potentials, an embedding energy associated with the cost of embedding the atom in a specific electron density, and is inherently non-local with many-body interactions included implicitly in

its structure. Specifically, the EAM energy of atom i is represented as

$$E_i = F_i(\bar{\rho}_i) + \frac{1}{2} \sum_{j \neq i} V_{ij}(r_{ij}) \quad (3.2)$$

where F_i is an embedding energy which is dependent on electron-density, V_{ij} is a pair potential between atom i and its neighbor j and r_{ij} is the separation distance between the atom pair. $\bar{\rho}_i$ is electron density of atom i , and is expressed in terms of density contributions ρ_j from each of the neighbors j as

$$\bar{\rho}_i = \sum_{j \neq i} \rho_j(r_{ij}) \quad (3.3)$$

Given the atomic potentials as function of the atomic coordinates $r_1 \dots r_N$, the total potential energy is the simple sum of equation (3.2). Force on each atom is given by

$$f_i = -\frac{\partial E_{tot}(\{r_1 \dots r_N\})}{\partial r_i} \quad (3.4)$$

3.2 Inter-atomic Potentials

Mishin et. al. proposed an approach to the development of reliable inter-atomic potentials for monotonic metals based on a large set of experiment and *ab initio* data, especially for Al and Ni[62]. Table (3.1) lists function values at discrete data points for the inter-atomic potential of Al. Intermediate values and the derivatives of the potential functions needs to be interpolated/extrapolated using suitable spline functions. In this dissertation, a cubic-spline interpolation will be used for this purpose.

3.2.1 Interpolation and Extrapolation of Interatomic Potentials for Al

For pair potential function $V(r)$, a cubic spline interpolation for the interval $[1.0018, 6.2872]$ with clamped boundary conditions at both ends will be used. Also extrapolation functions to determine the functions value when $r \notin (1.0018, 6.2872)$ will be used. Specifically when $r \in (0, 1.0018)$, $V(r)$ is assumed to have a form

$$V(r) = a_0 \log r + a_1 r + a_2 \quad (3.5)$$

When $r \in (6.272, \infty)$, $V(r)$ is assumed to have the form

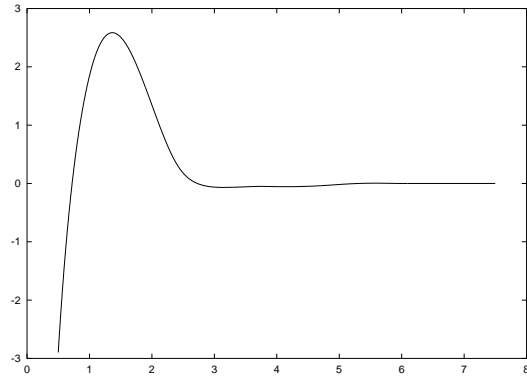
$$V(r) = a_3 r + a_4 \quad (3.6)$$

For atomic density function $\rho(r)$, a cubic spline interpolation for the interval $[1.0018, 6.2872]$ with clamped boundary conditions at both ends is used. Extrapolation to determine the functions value when $r \notin (1.0018, 6.2872)$ is accomplished when $r \in (0, 1.0018)$, by using

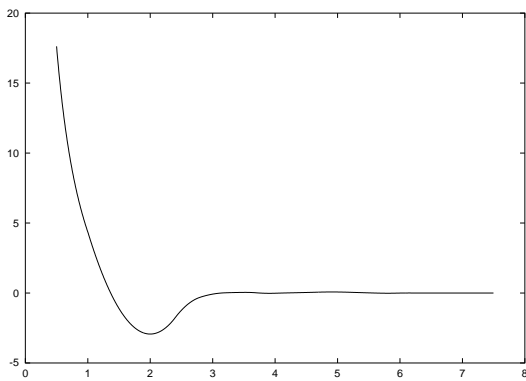
$$\rho(r) = b_0 r + b_1 r^2 + b_2 r^3 \quad (3.7)$$

When $r \in (6.272, \infty)$, $\rho(r)$ is taken in the form

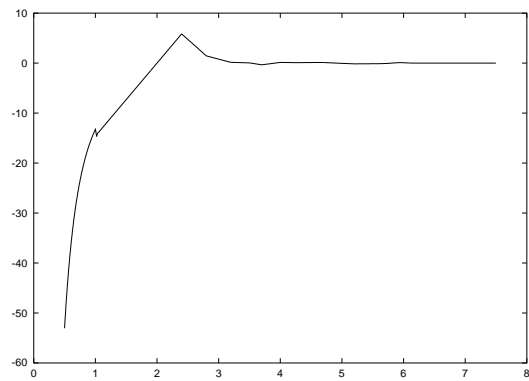
$$\rho(r) = b_3 r + b_4 \quad (3.8)$$



(a) pair potential $V(r)$

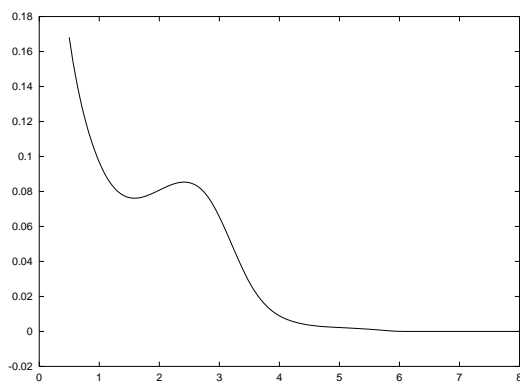


(b) $dV(r)/dr$

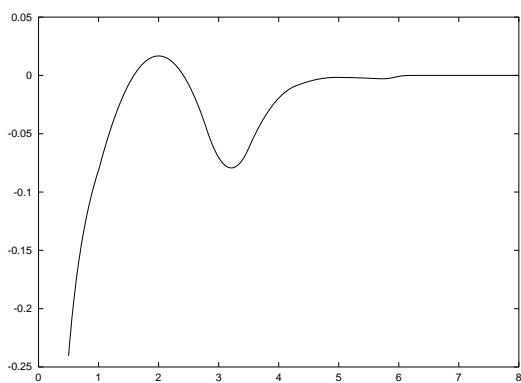


(c) $d^2V(r)/dr^2$

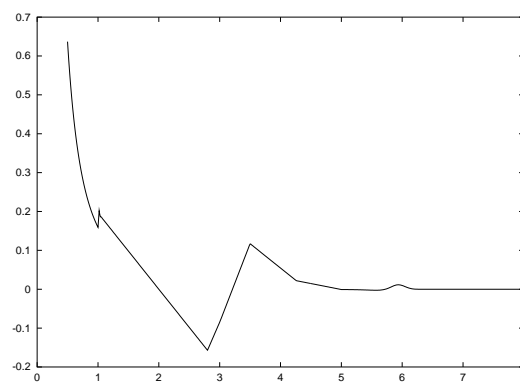
Figure 3.1: Pair potential functions for Al. (a) $V[\text{eV}]$ vs $r[\text{Å}]$. (b) $dV/dr [\text{eV}/\text{Å}]$ vs $r[\text{Å}]$. (c) $d^2V/dr^2 [\text{eV}/\text{Å}^2]$ vs $r[\text{Å}]$



(a) atomic density $\rho(r)$



(b) $d\rho(r)/dr$



(c) $d^2\rho(r)/dr^2$

Figure 3.2: Atomic density functions for Al. (a) ρ [unit] vs $r[\text{\AA}]$. (b) $d\rho/dr$ [unit/ \AA] vs $r[\text{\AA}]$. (c) $d^2\rho/dr^2$ [unit/ \AA^2] vs $r[\text{\AA}]$

Table 3.1: Tabulated potential functions for Al and Ni from [62]

| $r(\text{\AA})$ | Al | | | Ni | | | Al | | Ni | |
|-----------------|----------------|--------|-----------------|----------------|--------|--------------|----------------|--------------|----------------|--|
| | $V(\text{eV})$ | ρ | $r(\text{\AA})$ | $V(\text{eV})$ | ρ | $\bar{\rho}$ | $F(\text{eV})$ | $\bar{\rho}$ | $F(\text{eV})$ | |
| 2.000 | 1.3467 | 0.0808 | 2.0000 | 0.7597 | 0.0671 | 0.000 | 0.0000 | 0.0000 | 0.0000 | |
| 2.1786 | 0.8365 | 0.0835 | 2.1585 | 0.1812 | 0.0727 | 0.050 | -0.6192 | 0.050 | -0.2164 | |
| 2.3573 | 0.4096 | 0.0852 | 2.3170 | -0.1391 | 0.0761 | 0.100 | -1.0792 | 0.100 | -0.5094 | |
| 2.5359 | 0.1386 | 0.0847 | 2.4755 | -0.2214 | 0.0755 | 0.150 | -1.4100 | 0.150 | -0.8488 | |
| 2.7145 | 0.0062 | 0.0808 | 2.6340 | -0.2153 | 0.0691 | 0.200 | -1.6414 | 0.200 | -1.2042 | |
| 2.8932 | -0.0488 | 0.0724 | 2.7924 | -0.1766 | 0.0579 | 0.250 | -1.8033 | 0.250 | -1.5453 | |
| 3.0718 | -0.0665 | 0.0602 | 2.9509 | -0.1291 | 0.0440 | 0.300 | -1.9255 | 0.300 | -1.8419 | |
| 3.2504 | -0.0662 | 0.0463 | 3.1094 | -0.0909 | 0.0301 | 0.350 | -2.0330 | 0.350 | -2.0714 | |
| 3.4291 | -0.0605 | 0.0328 | 3.2679 | -0.0643 | 0.0193 | 0.400 | -2.1313 | 0.400 | -2.2426 | |
| 3.6077 | -0.0529 | 0.0220 | 3.4264 | -0.0423 | 0.0123 | 0.450 | -2.2209 | 0.450 | -2.3721 | |
| 3.7863 | -0.0503 | 0.0145 | 3.5849 | -0.0252 | 0.0081 | 0.500 | -2.3024 | 0.500 | -2.4766 | |
| 3.9650 | -0.0537 | 0.0096 | 3.7434 | -0.0139 | 0.0057 | 0.550 | -2.3764 | 0.550 | -2.5698 | |
| 4.1436 | -0.0554 | 0.0066 | 3.9019 | -0.0089 | 0.0043 | 0.600 | -2.4434 | 0.600 | -2.6542 | |
| 4.3222 | -0.0535 | 0.0048 | 4.0604 | -0.0084 | 0.0031 | 0.650 | -2.5038 | 0.650 | -2.7296 | |
| 4.5009 | -0.0485 | 0.0036 | 4.2189 | -0.0078 | 0.0021 | 0.700 | -2.5574 | 0.700 | -2.7958 | |
| 4.6795 | -0.0400 | 0.0029 | 4.3773 | -0.0043 | 0.0014 | 0.750 | -2.6039 | 0.750 | -2.8525 | |
| 4.8581 | -0.0279 | 0.0025 | 4.5358 | 0.0006 | 0.0008 | 0.800 | -2.6428 | 0.800 | -2.8995 | |
| 5.0368 | -0.0149 | 0.0022 | 4.6943 | 0.0044 | 0.0004 | 0.850 | -2.6737 | 0.850 | -2.9364 | |
| 5.2154 | -0.0041 | 0.0018 | 4.8528 | 0.0052 | 0.0002 | 0.900 | -2.6963 | 0.900 | -2.9631 | |
| 5.3940 | 0.0025 | 0.0015 | 5.0113 | 0.0037 | 0.0001 | 0.950 | -2.7101 | 0.950 | -2.9793 | |
| 5.5727 | 0.0048 | 0.0011 | 5.1698 | 0.0022 | 0.0000 | 0.975 | -2.7136 | 0.975 | -2.9834 | |
| 5.7513 | 0.0034 | 0.0006 | 5.3283 | 0.0024 | 0.0000 | 1.000 | -2.7148 | 1.000 | -2.9848 | |
| 5.9299 | 0.0006 | 0.0001 | 5.4868 | 0.0020 | 0.0000 | 1.025 | -2.7137 | 1.025 | -2.9840 | |
| 6.1086 | -0.0001 | 0.0000 | 5.6453 | 0.0004 | 0.0000 | 1.050 | -2.7108 | 1.050 | -2.9838 | |
| 6.2872 | 0.0000 | 0.0000 | 5.8037 | 0.0000 | 0.0000 | 1.100 | -2.7016 | 1.100 | -2.9990 | |

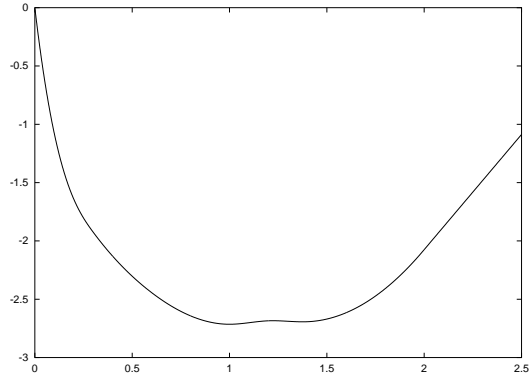
For embedding energy function $F(\bar{\rho})$, a cubic spline interpolation for the interval(0.00, 2.000] with clamped boundary conditions at both ends is used. Extrapolation to determine the functions value when $\bar{\rho} \in (2.000, \infty)$ results in

$$F(\bar{\rho}) = c_1\bar{\rho} + c_2 (\bar{\rho} \in (2.000, \infty)) \quad (3.9)$$

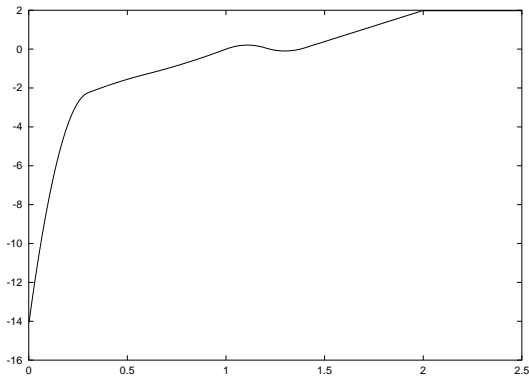
With the functions $V(r)$, $\rho(r)$, $F(\bar{\rho})$ at hand, the 0th, 1st and 2nd derivatives of these functions can be calculated as shown in figs.(3.1, 3.2&3.3).

3.3 Continuum Mechanics/Local Quasi-Continuum

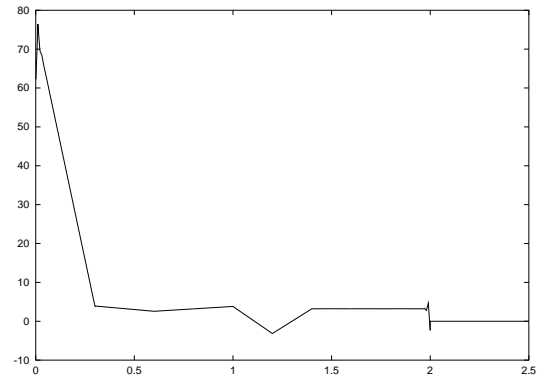
It is assumed in continuum mechanics that a strain energy functional W exists for a material. The energy stored in an incremental volume dV around point X is given by $W(X)dV$. The overall potential energy of the material can be obtained as an integral over the volume Ω of the



(a) embedding energy $F(\bar{\rho})$



(b) $dF(\bar{\rho})/d\bar{\rho}$



(c) $d^2F(\bar{\rho})/d\bar{\rho}^2$

Figure 3.3: Embedding energy functions for Al. (a) $F[\text{eV}]$ vs $\bar{\rho}[\text{unit}]$. (b) $dF/d\bar{\rho}[\text{eV/unit}]$ vs $\bar{\rho}[\text{unit}]$. (c) $d^2F/d\bar{\rho}^2[\text{eV/unit}]$ vs $\bar{\rho}[\text{unit}]$

body, i.e.

$$E_{tot} = \int_{\Omega} W(X) dV \quad (3.10)$$

3.3.1 Deformation Gradient and Large Deformation

Starting from the stress-free reference state of the undeformed perfect crystal, a deformed state can be described by a deformation gradient $F_{ij}(X_k)$. Let a point X_k in the undeformed material move to the point x_k in the deformed configuration. The displacement referenced to the undeformed configuration is $u_k(X) = x_k - X_k$. The deformation gradient $F_{ij}(X_k)$ is a second-rank tensor that maps an infinitesimal vector dX at point X in undeformed state to the infinitesimal vector dx in the deformed state. The infinitesimal difference $dx_k - dX_k$ describes the local deformation (stretching and rotating) referred to the original point X_k . The deformation gradient is simply written as

$$\mathbf{F}(\mathbf{X}) = \frac{d\mathbf{x}}{d\mathbf{X}} = \mathbf{I} + \nabla \mathbf{u}(\mathbf{X}) \quad (3.11)$$

3.3.2 Energy Density Functional

The locality of $W(X_k)$ implies that the strain energy density at material points X_k is equal to the energy stored in atomic bonds per unit volume of an infinite perfect crystal subject to a homogeneous deformation $\mathbf{F}(\mathbf{X})$.

This is the so called Cauchy-Born(CB) hypothesis used to calculate strain energy per unit volume of an infinite crystal. For a given deformation gradient \mathbf{F} , the unit cell deforms according to mapping the primitive bravais lattice vectors of the undeformed crystalline structure ($\mathbf{A}_i, i = 1, \dots, 3$) into the deformed vectors $\boldsymbol{\alpha}_i = \mathbf{F} \cdot \mathbf{A}_i$ (see figure 3.4).

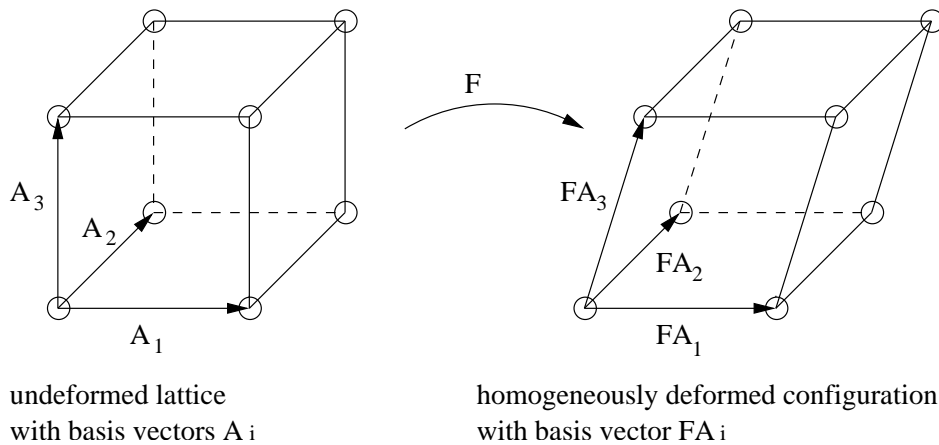


Figure 3.4: Illustration of Cauchy-Born rule which maps \mathbf{A}_i into $\boldsymbol{\alpha}_i$

The Cauchy-Born rule states that a uniform deformation gradient at the mesoscale can be mapped directly to the same uniform deformation gradient on the nanoscale. For crystalline solids with a simple lattice structure, this means that every atom in a region subject to a uniform deformation gradient will be equivalent in the sense of energy. Therefore, the energy within an

element can be estimated by an integral over the element volume with the use of Gaussian quadrature. Actually, the calculation of the CB energy is performed separately in a unit cell with periodic boundary conditions generated by the application of a deformation gradient \mathbf{F} . The resulting energy density is then written as

$$W(\mathbf{F}(\mathbf{X})) = \frac{E_{cell}[\mathbf{F}(\mathbf{X})]}{\Omega_{cell}} \quad (3.12)$$

where Ω_{cell} is the unit cell volume (in the undeformed configuration) and E_{cell} is the energy of the unit cell when its lattice vectors deform according to the deformation gradient \mathbf{F} .

The deformation gradient field is determined by the displacement of nodes. As mentioned above, the total energy of an element is an integral over the element volume, and the total energy of the system is simply the sum over energies of element e :

$$E_{tot} \approx \sum_{e=1}^{N_{element}} \int_{\Omega_e} U(F) d\Omega_e \quad (3.13)$$

However, even when the deformation is uniform within an element, the local prescription for the energy in the element is still approximate. The reason is that the displacement field, generated using periodic boundary conditions based on the deformation gradient, changes from one element to the next. Atoms at element boundaries and free surfaces, compared with those in a bulk uniformly deformed lattice, have different atomistic environment and therefore have significantly different energies.

In situations where the deformation is changing slowly from one element to the next and where surface energetics do not play an important role, the local prescription is a reasonably good approximation. Using the CB rule as in equation (3.12), the QC can be considered as continuum formulation in which the constitutive law is generated through inter-atomic potentials rather than experiments. The resulting CB constitutive law automatically ensures the correct anisotropic crystal elasticity response for small deformations. It acts like non-linear hyperelastic for intermediate strains and includes lattice invariance for large deformations[64].

When $W(X)$ is calculated in the continuum model, it accounts for the non-locality of the atomic interactions but it does so by assuming a homogeneous deformation around any given integration point rather than considering the true inhomogeneous deformation. Differentiating equation(3.12) with respect to the deformation gradient components, through use of equations (3.2) and (3.3), we obtain the components of the 1st Piola-Kirchoff stress tensor

$$\begin{aligned} T_{pQ} &= \frac{\partial W}{\partial F_{pQ}} \\ &= \frac{1}{\Omega_{cell}} \sum_{i=1}^{N_{latt}} \frac{\partial E_i}{\partial F_{pQ}} \\ &= \frac{1}{\Omega_{cell}} \sum_{i=1}^{N_{latt}} \left[\left. \frac{dF(\bar{\rho})}{d\bar{\rho}} \right|_{\bar{\rho}_i} \frac{\partial \bar{\rho}_i}{\partial F_{pQ}} + \frac{1}{2} \sum_{j \neq i}^{r_{ij} \leq r_{cut}} \frac{\partial V(r_{ij})}{\partial F_{pQ}} \right] \end{aligned}$$

$$\begin{aligned}
&= \frac{1}{\Omega_{\text{cell}}} \sum_{i=1}^{N_{\text{latt}}} \left[\frac{dF(\bar{\rho})}{d\bar{\rho}} \Big|_{\bar{\rho}_i} \sum_{j \neq i}^{r_{ij} \leq r_{\text{cut}}} \left(\frac{d\rho(r)}{dr} \Big|_{r_{ij}} \frac{\partial r_{ij}}{\partial F_{pQ}} \right) + \frac{1}{2} \sum_{j \neq i}^{r_{ij} \leq r_{\text{cut}}} \left(\frac{dV(r)}{dr} \Big|_{r_{ij}} \frac{\partial r_{ij}}{\partial F_{pQ}} \right) \right] \\
&= \frac{1}{\Omega_{\text{cell}}} \sum_{i=1}^{N_{\text{latt}}} \left[\sum_{j \neq i}^{r_{ij} \leq r_{\text{cut}}} \left(\left\langle F'(\bar{\rho}_i) \rho'(r_{ij}) + \frac{1}{2} V'(r_{ij}) \right\rangle \frac{\partial r_{ij}}{\partial F_{pQ}} \right) \right] \tag{3.14}
\end{aligned}$$

where N_{latt} is the number of atoms in a unit cell, Ω_{cell} is the unit cell volume. Note that

$$r_{ij} = \sqrt{(x_k^i - x_k^j)(x_k^i - x_k^j)} \text{ (sum on k, no sum on i and j)} \tag{3.15}$$

$$x_r^m = F_{rS} X_S^m \tag{3.16}$$

$$\frac{\partial x_r^m}{\partial F_{pQ}} = \delta_{pr} X_Q^m \tag{3.17}$$

$$\frac{\partial r_{ij}}{\partial x_n^i} = \frac{x_n^i - x_n^j}{r_{ij}} \text{ (no sum on i and j)} \tag{3.18}$$

So we have

$$\begin{aligned}
\frac{\partial r_{ij}}{\partial F_{pQ}} &= \frac{\partial r_{ij}}{\partial x_n^i} \frac{\partial x_n^i}{\partial F_{pQ}} + \frac{\partial r_{ij}}{\partial x_n^j} \frac{\partial x_n^j}{\partial F_{pQ}} \text{ (sum on n, no sum on i and j)} \\
&= \frac{x_n^i - x_n^j}{r_{ij}} \delta_{pn} X_Q^i + \frac{x_n^j - x_n^i}{r_{ij}} \delta_{pn} X_Q^j \\
&= \frac{(x_p^i - x_p^j)(X_Q^i - X_Q^j)}{r_{ij}} \\
&= \frac{F_{pT}(X_T^i - X_T^j)(X_Q^i - X_Q^j)}{r_{ij}} \text{ (sum on n, no sum on i and j)} \tag{3.19}
\end{aligned}$$

The 4th order material response tensor is

$$\begin{aligned}
C_{pQrS} &= \frac{\partial W}{\partial F_{pQ} \partial F_{rS}} \\
&= \frac{1}{\Omega_{\text{cell}}} \sum_{i=1}^{N_{\text{latt}}} \frac{\partial E_i}{\partial F_{pQ} \partial F_{rS}} \tag{3.20}
\end{aligned}$$

From equations (3.2), (3.3) and (3.14) we have

$$\begin{aligned}
\frac{\partial E_i}{\partial F_{pQ} \partial F_{rS}} &= \frac{\partial}{\partial F_{rS}} \left[\sum_{j \neq i}^{r_{ij} \leq r_{\text{cut}}} \left(\left\langle F'(\bar{\rho}_i) \rho'(r_{ij}) + \frac{1}{2} V'(r_{ij}) \right\rangle \frac{\partial r_{ij}}{\partial F_{pQ}} \right) \right] \\
&= F''(\bar{\rho}_i) \left[\sum_{m \neq i}^{r_{im} \leq r_{\text{cut}}} \rho'(r_{im}) \frac{\partial r_{im}}{\partial F_{rS}} \right] \left[\sum_{j \neq i}^{r_{ij} \leq r_{\text{cut}}} \rho'(r_{ij}) \frac{\partial r_{ij}}{\partial F_{pQ}} \right] \\
&+ \sum_{j \neq i}^{r_{ij} \leq r_{\text{cut}}} \left[\left(F'(\bar{\rho}_i) \rho''(r_{ij}) + \frac{1}{2} V''(r_{ij}) \right) \frac{\partial r_{ij}}{\partial F_{pQ}} \frac{\partial r_{ij}}{\partial F_{rS}} \right] \\
&+ \sum_{j \neq i}^{r_{ij} \leq r_{\text{cut}}} \left[\left(F'(\bar{\rho}_i) \rho'(r_{ij}) + \frac{1}{2} V'(r_{ij}) \right) \frac{\partial^2 r_{ij}}{\partial F_{pQ} \partial F_{rS}} \right] \tag{3.21}
\end{aligned}$$

The partial derivative $\frac{\partial r_{ij}}{\partial F_{pQ}}$ is given in eqn (3.19). Making use of equations (3.15) \sim (3.19) we have

$$\begin{aligned}
\frac{\partial^2 r_{ij}}{\partial F_{pQ} \partial F_{rS}} &= \frac{\partial}{\partial F_{rS}} \left[\frac{1}{r_{ij}} F_{pT} (X_T^i - X_T^j) (X_Q^i - X_Q^j) \right] \\
&= \frac{-1}{r_{ij}^2} \frac{\partial r_{ij}}{\partial F_{rS}} F_{pT} (X_T^i - X_T^j) (X_Q^i - X_Q^j) \\
&\quad + \frac{1}{r_{ij}} \delta_{rp} \delta_{TS} (X_T^i - X_T^j) (X_Q^i - X_Q^j) \\
&= \frac{-1}{r_{ij}^3} (x_p^i - x_p^j) (X_Q^i - X_Q^j) (x_r^i - x_r^j) (X_S^i - X_S^j) \\
&\quad + \frac{1}{r_{ij}} \delta_{rp} (X_S^i - X_S^j) (X_Q^i - X_Q^j) \text{ (no sum on i and j)} \tag{3.22}
\end{aligned}$$

One advantage of the local QC approach is that it permits the use of quantum mechanical calculation that cannot be decomposed as a sum over individual atom energies such as those generated by density functional theory (DFT) or by tight binding (TB) methods for a lattice undergoing a uniform deformation with periodic boundary conditions. Using quantum mechanical energy calculations in atomic model generally ensures the description more transferable, i.e. it provides a more accurate description of the energy of atomic configurations away from the reference configuration to which classical empirical potentials are fitted. This makes truly first-principles simulations applicable for some macroscopic process such as phase transformation [64].

3.4 Fully Atomistic/Nonlocal QC

The local QC formulation successfully incorporated atomistic properties such as nonlinearity, crystal symmetry and lattice invariance into the continuum FEM framework. The property of lattice invariance means that dislocations may exist in the continuum region. However, the core structure and energy of these dislocations will only be coarsely represented because of the uniform deformation assumption. Actually, due to uniform deformation constraint, the local QC formulation is unable to capture the details of non-uniform defects such as stacking faults, interfaces, and free surfaces.

In order to correctly capture these details, the nonlocal QC must be developed. The energy of the system, which in the local QC was dependent on the deformation gradient at integration points, must instead be replaced in a way that can sense non-uniform deformation and free surfaces, especially in the limit where full atomistic description is required. Traditionally nonlocal QC formulation falls into two basic categories: *energy-based* formulation and *force-based* formulation. Both start from the energy of the system, solving the problem by finding equilibrium configurations of the atoms. For energy-based formulation, this involves computing the total energy and then driving the system to the energy minimizing configuration. For force-based formulation, this involves computing forces on each atom/node, and then driving the system to the zero force configuration.

3.4.1 Energy-based Formulation

In the energy-based formulation, it is assumed that the approximate energy of the system can be obtained by explicitly computing only the energy of the representative atoms. Therefore, the new approximate energy was give by [79]

$$E_{tot} \approx \sum_{\alpha=1}^{N_{rep}} n_{\alpha} E_{\alpha} \quad (3.23)$$

The function n_{α} is a weight function for representative atom α , which will be high for representative atoms in regions of low representative atom density and vice versa. Obviously for consistency, the weight functions must satisfy the following condition

$$\sum_{\alpha=1}^{N_{rep}} n_{\alpha} = N \quad (3.24)$$

which further implies that all $n_{\alpha} = 1$ in fully atomistic regions. Physically, the weight functions n_{α} can be considered as the number of atoms represented by each representative atom α .

3.4.2 Force-based Formulation

The forced-based formulation is based on the fact that energy minimization physically implies driving the system to equilibrium status in which the force on each degree of freedom is zero. Equilibrium can be obtained by solving directly from an approximate expression for forces, rather than from the explicit differentiation of an single energy functional. This formulation starts from taking the partial derivatives of the total system energy with respect to each representative atom's displacement:

$$\begin{aligned} -f_p^i &= \frac{\partial E_{tot}}{\partial x_p^i} = \sum_{r_{ij} \leq r_{cut}} \frac{\partial E_j}{\partial x_p^i} = \sum_{j \neq i}^{r_{ij} \leq r_{cut}} \frac{\partial E_j}{\partial x_p^i} + \frac{\partial E_i}{\partial x_p^i} \\ &= \sum_{j \neq i}^{r_{ij} \leq r_{cut}} \left[\frac{dF(\bar{\rho})}{d\bar{\rho}} \Big|_{\bar{\rho}_j} \frac{\partial \bar{\rho}_j}{\partial x_p^i} + \frac{1}{2} \frac{\partial V(r_{ij})}{\partial x_p^i} \right] + \sum_{k \neq i}^{r_{ik} \leq r_{cut}} \left[\frac{dF(\bar{\rho})}{d\bar{\rho}} \Big|_{\bar{\rho}_i} \frac{\partial \rho(r_{ik})}{\partial x_p^i} + \frac{1}{2} \frac{\partial V(r_{ik})}{\partial x_p^i} \right] \\ &= \sum_{j \neq i}^{r_{ij} \leq r_{cut}} \left[\frac{dF(\bar{\rho})}{d\bar{\rho}} \Big|_{\bar{\rho}_j} \frac{d\rho(r)}{dr} \Big|_{r_{ij}} \frac{\partial r_{ij}}{\partial x_p^i} + \frac{1}{2} \frac{dV(r)}{dr} \Big|_{r_{ij}} \frac{\partial r_{ij}}{\partial x_p^i} \right] \\ &+ \sum_{k \neq i}^{r_{ik} \leq r_{cut}} \left[\frac{dF(\bar{\rho})}{d\bar{\rho}} \Big|_{\bar{\rho}_i} \frac{d\rho(r)}{dr} \Big|_{r_{ik}} \frac{\partial r_{ik}}{\partial x_p^i} + \frac{1}{2} \frac{dV(r)}{dr} \Big|_{r_{ik}} \frac{\partial r_{ik}}{\partial x_p^i} \right] \\ &= \sum_{j \neq i}^{r_{ij} \leq r_{cut}} \left(F'(\bar{\rho}_j) \rho'(r_{ij}) + \frac{1}{2} V'(r_{ij}) \right) \frac{\partial r_{ij}}{\partial x_p^i} \\ &+ \sum_{k \neq i}^{r_{ik} \leq r_{cut}} \left(F'(\bar{\rho}_i) \rho'(r_{ik}) + \frac{1}{2} V'(r_{ik}) \right) \frac{\partial r_{ik}}{\partial x_p^i} \end{aligned} \quad (3.25)$$

where

$$\frac{\partial r_{ij}}{\partial x_p^i} = \frac{x_p^i - x_p^j}{r_{ij}} \quad (i \neq j, \text{ no sum on } i \text{ and } j) \quad (3.26)$$

The global stiffness matrix contribution follows as

$$\begin{aligned} -\frac{\partial f_p^i}{\partial x_q^l} &= \frac{\partial^2 E^a}{\partial x_p^i \partial x_q^l} = \sum_{r_{ij} \leq r_{cut}} \frac{\partial^2 E_j}{\partial x_p^i \partial x_q^l} \\ &= \frac{\partial}{\partial x_q^l} \left[\sum_{\substack{r_{ij} \leq r_{cut} \\ j \neq i}} \left(F'(\bar{\rho}_j) \rho'(r_{ij}) + \frac{1}{2} V'(r_{ij}) \right) \frac{\partial r_{ij}}{\partial x_p^i} \right] \\ &+ \frac{\partial}{\partial x_q^l} \left[\sum_{\substack{r_{ik} \leq r_{cut} \\ k \neq i}} \left(F'(\bar{\rho}_i) \rho'(r_{ik}) + \frac{1}{2} V'(r_{ik}) \right) \frac{\partial r_{ik}}{\partial x_p^i} \right] \\ &= \sum_{\substack{r_{ij} \leq r_{cut} \\ j \neq i}} \left[F''(\bar{\rho}_j) \rho'(r_{ij}) \frac{\partial r_{ij}}{\partial x_p^i} \sum_{\substack{r_{nj} \leq r_{cut} \\ n \neq j}} \left(\rho'(r_{nj}) \frac{\partial r_{nj}}{\partial x_q^l} \right) \right] \\ &+ \sum_{\substack{r_{ij} \leq r_{cut} \\ j \neq i}} \left[\left(F'(\bar{\rho}_j) \rho''(r_{ij}) + \frac{1}{2} V''(r_{ij}) \right) \frac{\partial r_{ij}}{\partial x_p^i} \frac{\partial r_{ij}}{\partial x_q^l} \right] \\ &+ \sum_{\substack{r_{ij} \leq r_{cut} \\ j \neq i}} \left[\left(F'(\bar{\rho}_j) \rho'(r_{ij}) + \frac{1}{2} V'(r_{ij}) \right) \frac{\partial^2 r_{ij}}{\partial x_p^i \partial x_q^l} \right] \\ &+ \sum_{\substack{r_{ik} \leq r_{cut} \\ k \neq i}} \left[F''(\bar{\rho}_i) \rho'(r_{ik}) \frac{\partial r_{ik}}{\partial x_p^i} \sum_{\substack{r_{ni} \leq r_{cut} \\ n \neq i}} \left(\rho'(r_{ni}) \frac{\partial r_{ni}}{\partial x_q^l} \right) \right] \\ &+ \sum_{\substack{r_{ik} \leq r_{cut} \\ k \neq i}} \left[\left(F'(\bar{\rho}_i) \rho''(r_{ik}) + \frac{1}{2} V''(r_{ik}) \right) \frac{\partial r_{ik}}{\partial x_p^i} \frac{\partial r_{ik}}{\partial x_q^l} \right] \\ &+ \sum_{\substack{r_{ik} \leq r_{cut} \\ k \neq i}} \left[\left(F'(\bar{\rho}_i) \rho'(r_{ik}) + \frac{1}{2} V'(r_{ik}) \right) \frac{\partial^2 r_{ik}}{\partial x_p^i \partial x_q^l} \right] \end{aligned} \quad (3.27)$$

where

$$\frac{\partial r_{ij}}{\partial x_q^l} = \frac{1}{r_{ij}} (x_q^i - x_q^j) (\delta_{il} - \delta_{jl}) \quad (i \neq j, \text{ no sum on } i \text{ and } j) \quad (3.28)$$

$$\begin{aligned} \frac{\partial^2 r_{ij}}{\partial x_p^i \partial x_q^l} &= \frac{\partial}{\partial x_q^l} \left[\frac{x_p^i - x_p^j}{r_{ij}} \right] \\ &= \frac{1}{r_{ij}} \frac{\partial (x_p^i - x_p^j)}{\partial x_q^l} + (x_p^i - x_p^j) \frac{-1}{r_{ij}^2} \frac{\partial r_{ij}}{\partial x_q^l} \\ &= \frac{1}{r_{ij}} \delta_{pq} (\delta_{il} - \delta_{jl}) - \frac{1}{r_{ij}^3} (x_p^i - x_p^j) (x_q^i - x_q^j) (\delta_{il} - \delta_{jl}) \end{aligned}$$

$$(i \neq j, \text{ no sum on } i \text{ and } j) \quad (3.29)$$

The main disadvantage of fully nonlocal QC is its high computational cost in regions of slowly changing deformation gradient as compared with the local description.

The main advantage of the nonlocal QC, including both energy and force-based, is that when it is refined down to the atomic scale, it can correctly capture details of the dislocation core, stacking faults and grain boundary effects because it exactly equal to lattice statics.

3.5 Coupled Atomistic/Continuum Methods

Noting that the nonlocal QC is exact in regions where full atomistic description is required, while the local QC is computationally advantageous in regions of slowly varying deformation gradients, it is desirable to have the ability to use both formulations in a single simulation.

3.5.1 Local QC and Energy-based Methods

In order to develop such a formulation consider the energy of a system of atoms in equation(3.1). As in the energy-based nonlocal QC, the assumption that this energy can be approximated by computing only the energy of the representative atoms is retained with an additional assumption that each representative atom can either be *local* or *nonlocal* depending on its deformation environment. The energy expression is then approximately given by

$$E_{tot} \approx \sum_{\alpha=1}^{N_{nloc}} n_{\alpha} E_{\alpha} + \sum_{\alpha=1}^{N_{loc}} n_{\alpha} E_{\alpha} = \sum_{\alpha=1}^{N_{nloc}} n_{\alpha} E_{\alpha} + \sum_{e=1}^{N_{element}} \int_{\Omega_e} W(F) d\Omega_e$$

Effects of the Nonlocal/Local Interface: Ghost Force

In a coupled QC method, the basic idea is to use a fully atomistic description in some regions of material and a continuum description in other regions. The detailed treatment of interfaces between the nonlocal atomistic and local continuum regions is a key aspect of the QC method. One such interface is illustrated in figure 3.5, to highlight some of the important details. In the figure, nonlocal representative atoms are shown as filled, local atoms are shown as open. The left side of the interface is the atomistic region where every atom is explicitly represented and treated using interatomic potentials. On the other side, there is a FE mesh with its associated nodes where the nodes coincide with atomic lattice sites. Of course, not all atoms sites are occupied by nodes. At the interface between the FE nodes and the atoms there is a one-to-one mapping between atoms and nodes on the FE mesh. Moving away from the interface toward the continuum side, the FE nodes become increasingly sparse and the corresponding elements become larger. Finally, there is a 'pad' region where pseudo atoms exist on the continuum side of the interface and overlap physical space with FE elements. Some of the 'pad' atoms sit on the FE nodes while others reside within the elements. The pad of pseudo-atoms is a tool used to help account for the non-local interactions between atoms so that real atoms at and near the interface have a full atomistic environment. The single QC potential energy leads to some non-physical effects in the transition region. Taking partial derivatives of the energy functional, w.r.t atomic displacements, to obtain forces on atoms and FE nodes leads to so-called *ghost forces* in the transition region [79]. The ghost forces result from the assumption of locality in the continuum region, nonlocality in the atomistic region, and the local/nonlocal mismatch in the transition region. In short, the finite range of atomic interaction implies that the motion of pad atoms in the local region will effect the energy of nonlocal representative atoms, while the converse is not true if nonlocal atoms do not reside within the *FE* containing pad atoms. This

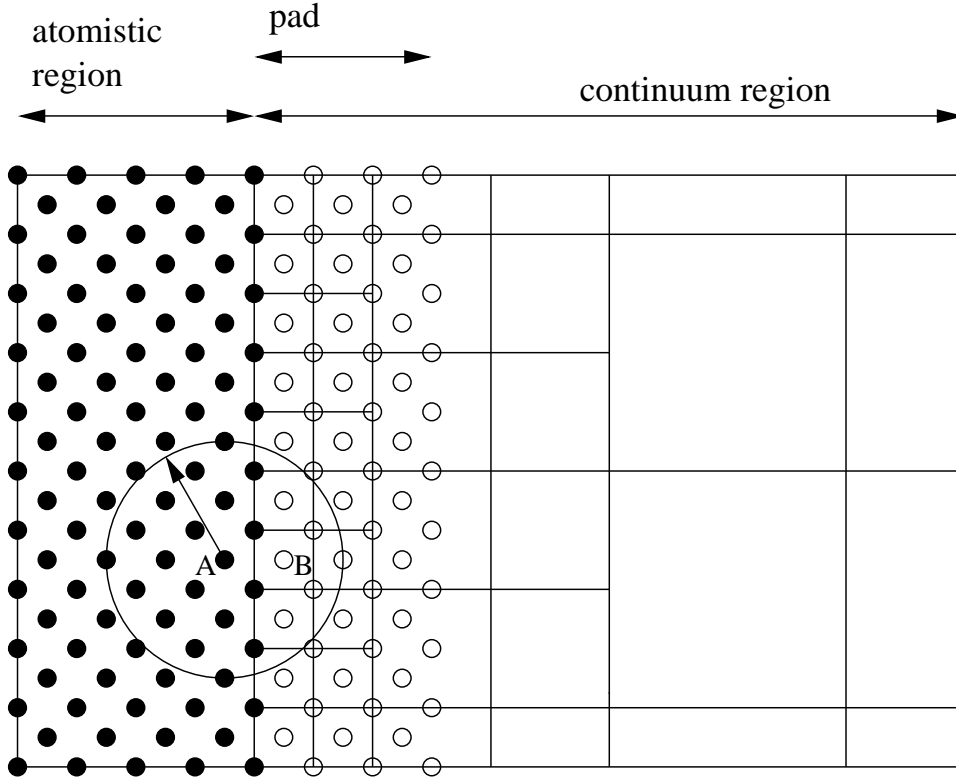


Figure 3.5: The atomistic/continuum transition region for the QC method

is shown in figure 3.5. The circle drawn around nonlocal atom A denotes the range of EAM interactions. On the one hand, as local atom B resides inside the sphere, its motion affects A and $\partial E_A/\partial u_B \neq 0$, which implies to a force acting on B due to A . In other words, A can see B . On the other hand, the energy of atom B is computed locally and depends on the deformation of the element containing it. Therefore, it is not affected by the nonlocal atom A . In other words, $\partial E_B/\partial u_A = 0$ and the motion of atom A does not lead to force on B . This means B can not see A . Note that these *ghost forces* are a consequence of differentiating an approximate energy functional.

Ghost Forces Correction

In order to correct the ghost forces, we have to add or subtract necessary forces acting on atoms and nodes in the transition regions. The basic rule is that atoms should 'see', from energetic point of view, only atoms while continuum nodes should 'see' only continuum nodes. This is achieved by requiring that forces acting on any atom be computed using only the formulation which corresponds to its status, as if the atoms was in a fully local or nonlocal description [64]. For example, the nonlocal term $\partial E_A/\partial u_B$ is subtracted from the forces acting on local atom B and a term, $\partial E_B/\partial u_A$ is computed for atom A . Ghost forces do not derive from a potential and consequently they are not symmetrical, i.e. the ghost force on B due to A is not equal to that due to B on A . To correct the ghost forces effect an auxiliary potential energy function \hat{E}_{QC} is introduced for the mixed formulation where missing terms are added on as dead loads and

extraneous terms are subtracted off,

$$\hat{E}_{QC} = E_{QC} - \sum_{\alpha} f_{\alpha}^G \cdot u_{\alpha} \quad (3.30)$$

where f_{α}^G are the ghost-force correction terms and u_{α} are the corresponding displacements. Especially, the f_{α}^G are

$$f_{\alpha}^G = \begin{cases} -\frac{\partial \sum_{i \in P} E^i}{\partial u_{\alpha}} & \text{if } \alpha \in A \\ \frac{\partial \sum_{i \in A} E^i}{\partial u_{\alpha}} & \text{if } \alpha \in P \\ -\frac{\partial \sum_{i \in P} E^i}{\partial u_{\alpha}} + \frac{\partial \sum E_{\mu}}{\partial u_{\alpha}} & \text{if } \alpha \in I \end{cases} \quad (3.31)$$

Where 'A', 'I', 'P' denote atoms in the true atomistic region, atoms on the interface, and pseudo-atoms in the pad respectively. E_{μ} denotes the energy of FE element μ . Minimization of the auxiliary function \hat{E}_{QC} leads to the equilibrium configuration. The ghost forces are a function of atomic positions and thus new ghost forces arise, once atoms relax. This implies that we need recompute the ghost forces correction at the equilibrium configuration. Moreover, when adaptive meshing is applied such that the continuum/atomistic interface is changing, it is necessary to recalculate the ghost forces after each remeshing step since the atoms/nodes experiencing ghost forces are changing.

Forces and Stiffness Calculation for Nonlocal Atoms

In the nonlocal atomic region, due to the absence of a uniform strain field, it is impossible to define general measures of stress and stiffness as in a local continuum region. Consequently, the out-of-balance force residual and global stiffness must be written directly in terms of the EAM potentials sums. The nonlocal contribution to the out-of-balance residual is given by

$$\begin{aligned} -f_p^i &= \frac{\partial E^a}{\partial x_p^i} = \sum_{j \neq i, j \in (A, I)}^{r_{ij} \leq r_{cut}} \frac{\partial E_j}{\partial x_p^i} + \frac{\partial E_i}{\partial x_p^i} \\ &= \sum_{j \neq i, j \in (A, I)}^{r_{ij} \leq r_{cut}} \left[\left. \frac{dF(\bar{\rho})}{d\bar{\rho}} \right|_{\bar{\rho}_j} \frac{\partial \bar{\rho}_j}{\partial x_p^i} + \frac{1}{2} \frac{\partial V(r_{ij})}{\partial x_p^i} \right] + \sum_{k \neq i, k \in (A, I, P)}^{r_{ik} \leq r_{cut}} \left[\left. \frac{dF(\bar{\rho})}{d\bar{\rho}} \right|_{\bar{\rho}_i} \frac{\partial \rho(r_{ik})}{\partial x_p^i} + \frac{1}{2} \frac{\partial V(r_{ik})}{\partial x_p^i} \right] \\ &= \sum_{j \neq i, j \in (A, I)}^{r_{ij} \leq r_{cut}} \left(F'(\bar{\rho}_j) \rho'(r_{ij}) + \frac{1}{2} V'(r_{ij}) \right) \frac{\partial r_{ij}}{\partial x_p^i} \\ &+ \sum_{k \neq i, k \in (A, I, P)}^{r_{ik} \leq r_{cut}} \left(F'(\bar{\rho}_i) \rho'(r_{ik}) + \frac{1}{2} V'(r_{ik}) \right) \frac{\partial r_{ik}}{\partial x_p^i} \end{aligned} \quad (3.32)$$

Similarly, the nonlocal contribution to the global stiffness matrix is given by

$$\begin{aligned} -\frac{\partial f_p^i}{\partial x_q^l} &= \frac{\partial E^a}{\partial x_p^i \partial x_q^l} = \sum_{j \neq i, j \in (A, I)}^{r_{ij} \leq r_{cut}} \left[\frac{\partial^2 E_j}{\partial x_p^i \partial x_q^l} \right] + \frac{\partial^2 E_i}{\partial x_p^i \partial x_q^l} \\ &= \frac{\partial}{\partial x_q^l} \left[\sum_{j \neq i, j \in (A, I)}^{r_{ij} \leq r_{cut}} \left(F'(\bar{\rho}_j) \rho'(r_{ij}) + \frac{1}{2} V'(r_{ij}) \right) \frac{\partial r_{ij}}{\partial x_p^i} \right] \end{aligned}$$

$$\begin{aligned}
& + \frac{\partial}{\partial x_q^l} \left[\sum_{k \neq i, k \in (A, I, P)}^{r_{ik} \leq r_{cut}} \left(F'(\bar{\rho}_i) \rho'(r_{ik}) + \frac{1}{2} V'(r_{ik}) \right) \frac{\partial r_{ik}}{\partial x_p^i} \right] \\
& = \sum_{j \neq i, j \in (A, I)}^{r_{ij} \leq r_{cut}} \left[F''(\bar{\rho}_j) \rho'(r_{ij}) \frac{\partial r_{ij}}{\partial x_p^i} \sum_{n \neq j}^{r_{nj} \leq r_{cut}} \left(\rho'(r_{nj}) \frac{\partial r_{nj}}{\partial x_q^l} \right) \right] \\
& + \sum_{j \neq i, j \in (A, I)}^{r_{ij} \leq r_{cut}} \left[\left(F'(\bar{\rho}_j) \rho''(r_{ij}) + \frac{1}{2} V''(r_{ij}) \right) \frac{\partial r_{ij}}{\partial x_p^i} \frac{\partial r_{ij}}{\partial x_q^l} \right] \\
& + \sum_{j \neq i, j \in (A, I)}^{r_{ij} \leq r_{cut}} \left[\left(F'(\bar{\rho}_j) \rho'(r_{ij}) + \frac{1}{2} V'(r_{ij}) \right) \frac{\partial^2 r_{ij}}{\partial x_p^i \partial x_q^l} \right] \\
& + \sum_{k \neq i, k \in (A, I, P)}^{r_{ik} \leq r_{cut}} \left[F''(\bar{\rho}_i) \rho'(r_{ik}) \frac{\partial r_{ik}}{\partial x_p^i} \sum_{n \neq i}^{r_{ni} \leq r_{cut}} \left(\rho'(r_{ni}) \frac{\partial r_{ni}}{\partial x_q^l} \right) \right] \\
& + \sum_{k \neq i, k \in (A, I, P)}^{r_{ik} \leq r_{cut}} \left[\left(F'(\bar{\rho}_i) \rho''(r_{ik}) + \frac{1}{2} V''(r_{ik}) \right) \frac{\partial r_{ik}}{\partial x_p^i} \frac{\partial r_{ik}}{\partial x_q^l} \right] \\
& + \sum_{k \neq i, k \in (A, I, P)}^{r_{ik} \leq r_{cut}} \left[\left(F'(\bar{\rho}_i) \rho'(r_{ik}) + \frac{1}{2} V'(r_{ik}) \right) \frac{\partial^2 r_{ik}}{\partial x_p^i \partial x_q^l} \right] \tag{3.33}
\end{aligned}$$

For $\frac{\partial r_{ij}}{\partial x_q^l}$ and $\frac{\partial^2 r_{ij}}{\partial x_p^i \partial x_q^l}$, please refer to equation (3.28) and (3.29), respectively.

3.5.2 Local QC and Forced-based Methods

The main reason for ghost forces is the fact that the above procedure has focus on approximating the energy rather than the forces. An alternative approach to eliminate ghost forces is to give up the requirement of a single energy functional and instead drive the system to equilibrium by seeking a configuration for which the forces on all the atoms/nodes are zero. Starting from this point, the forces need not be calculated strictly as partial derivatives of a single energy functional, and can instead be approximate expression for a physically motivated set of forces. Without a well defined total energy from which force can be derived, it is impossible to use the computationally efficient conjugate-gradient method to drive the entire system toward equilibrium. Static equilibrium can still be found using the forces only, however, via quasi-Newton methods or by applying the conjugate-gradient method to find a zero of the total force rather than a minimum of the total energy [85].

Force and Stiffness Calculation for Non-local Atoms

In the local QC plus forced based methods, true atom can 'see' pad atoms directly. The non-local contribution to the out-of-balance residual follows as

$$-f_p^i = \frac{\partial E_{tot}}{\partial x_p^i} = \sum_{j \neq i, j \in (A, I, P)}^{r_{ij} \leq r_{cut}} \frac{\partial E_j}{\partial x_p^i} + \frac{\partial E_i}{\partial x_p^i}$$

$$\begin{aligned}
&= \sum_{j \neq i, j \in (A, I, P)}^{r_{ij} \leq r_{cut}} \left[\frac{dF(\bar{\rho})}{d\bar{\rho}} \Big|_{\bar{\rho}_j} \frac{\partial \bar{\rho}_j}{\partial x_p^i} + \frac{1}{2} \frac{\partial V(r_{ij})}{\partial x_p^i} \right] + \sum_{k \neq i, k \in (A, I, P)}^{r_{ik} \leq r_{cut}} \left[\frac{dF(\bar{\rho})}{d\bar{\rho}} \Big|_{\bar{\rho}_i} \frac{\partial \rho(r_{ik})}{\partial x_p^i} + \frac{1}{2} \frac{\partial V(r_{ik})}{\partial x_p^i} \right] \\
&= \sum_{j \neq i, j \in (A, I, P)}^{r_{ij} \leq r_{cut}} \left(F'(\bar{\rho}_j) \rho'(r_{ij}) + \frac{1}{2} V'(r_{ij}) \right) \frac{\partial r_{ij}}{\partial x_p^i} \\
&+ \sum_{k \neq i, k \in (A, I, P)}^{r_{ik} \leq r_{cut}} \left(F'(\bar{\rho}_i) \rho'(r_{ik}) + \frac{1}{2} V'(r_{ik}) \right) \frac{\partial r_{ik}}{\partial x_p^i} \tag{3.34}
\end{aligned}$$

The non-local contribution to the global stiffness matrix can similarly be obtained

$$\begin{aligned}
-\frac{\partial f_p^i}{\partial x_q^l} &= \frac{\partial E^a}{\partial x_p^i \partial x_q^j} = \sum_{j \neq i, j \in (A, I, P)}^{r_{ij} \leq r_{cut}} \left[\frac{\partial^2 E_j}{\partial x_p^i \partial x_q^l} \right] + \frac{\partial^2 E_i}{\partial x_p^i \partial x_q^l} \\
&= \frac{\partial}{\partial x_q^l} \left[\sum_{j \neq i, j \in (A, I, P)}^{r_{ij} \leq r_{cut}} \left(F'(\bar{\rho}_j) \rho'(r_{ij}) + \frac{1}{2} V'(r_{ij}) \right) \frac{\partial r_{ij}}{\partial x_p^i} \right] \\
&+ \frac{\partial}{\partial x_q^l} \left[\sum_{k \neq i, k \in (A, I, P)}^{r_{ik} \leq r_{cut}} \left(F'(\bar{\rho}_i) \rho'(r_{ik}) + \frac{1}{2} V'(r_{ik}) \right) \frac{\partial r_{ik}}{\partial x_p^i} \right] \\
&= \sum_{j \neq i, j \in (A, I, P)}^{r_{ij} \leq r_{cut}} \left[F''(\bar{\rho}_j) \rho'(r_{ij}) \frac{\partial r_{ij}}{\partial x_p^i} \sum_{n \neq j}^{r_{nj} \leq r_{cut}} \left(\rho'(r_{nj}) \frac{\partial r_{nj}}{\partial x_q^l} \right) \right] \\
&+ \sum_{j \neq i, j \in (A, I, P)}^{r_{ij} \leq r_{cut}} \left[\left(F'(\bar{\rho}_j) \rho''(r_{ij}) + \frac{1}{2} V''(r_{ij}) \right) \frac{\partial r_{ij}}{\partial x_p^i} \frac{\partial r_{ij}}{\partial x_q^l} \right] \\
&+ \sum_{j \neq i, j \in (A, I, P)}^{r_{ij} \leq r_{cut}} \left[\left(F'(\bar{\rho}_j) \rho'(r_{ij}) + \frac{1}{2} V'(r_{ij}) \right) \frac{\partial^2 r_{ij}}{\partial x_p^i \partial x_q^l} \right] \\
&+ \sum_{k \neq i, k \in (A, I, P)}^{r_{ik} \leq r_{cut}} \left[F''(\bar{\rho}_i) \rho'(r_{ik}) \frac{\partial r_{ik}}{\partial x_p^i} \sum_{n \neq i}^{r_{ni} \leq r_{cut}} \left(\rho'(r_{ni}) \frac{\partial r_{ni}}{\partial x_q^l} \right) \right] \\
&+ \sum_{k \neq i, k \in (A, I, P)}^{r_{ik} \leq r_{cut}} \left[\left(F'(\bar{\rho}_i) \rho''(r_{ik}) + \frac{1}{2} V''(r_{ik}) \right) \frac{\partial r_{ik}}{\partial x_p^i} \frac{\partial r_{ik}}{\partial x_q^l} \right] \\
&+ \sum_{k \neq i, k \in (A, I, P)}^{r_{ik} \leq r_{cut}} \left[\left(F'(\bar{\rho}_i) \rho'(r_{ik}) + \frac{1}{2} V'(r_{ik}) \right) \frac{\partial^2 r_{ik}}{\partial x_p^i \partial x_q^l} \right] \tag{3.35}
\end{aligned}$$

Again, for $\frac{\partial r_{ij}}{\partial x_q^l}$ and $\frac{\partial^2 r_{ij}}{\partial x_p^i \partial x_q^l}$, please refer to equation (3.28) and (3.29) respectively. Note that stiffness matrix for force-based methods is not symmetrical any more since pad atoms can not see true atoms. The force-based formulation is implemented in this thesis. The unbalanced forces on atoms (on/close to free surfaces or interfaces) in the initial configuration are added as dead loads.

3.6 The Effect of Finite Temperature

The QC method discussed previously is limited to zero temperature or molecular statics. For many cases, the errors introduced by neglecting temperature effect are smaller than the errors associated with the empirical interatomic potentials. For some cases, for instance for the studying of thermal expansion, the effect must be accounted for. There are several approaches to account for the effect of finite temperature in numerical simulation. One is the molecular dynamics (*MD*) simulation. In *MD*, the motions of atoms are governed by Newton's second law. The *MD* will be able to generate the trajectories of the atoms with a given set of initial conditions. The instantaneous temperature is decided by the total kinetic energy of the system[24]. In another approach, Monte Carlo(MC) simulation are used to sample a set of statistically equivalent random atomistic states to derive a stochastic continuum-scale temperature[31]. These atomistic approaches are very accurate, but they have the disadvantage that of being computationally expensive.

An more efficient alternative finite-temperature continuum theory based on interatomic potentials was proposed by Jiang *et al* [37]. QC method has been successfully applied to quasistatic problems [79, 90]. Shenoy *et al*[82] first introduced temperature into QC to perform Monte Carlo (MC) simulation. The main limitation of this method is that short wavelength phonons in the atomistic region are reflected back rather than transferred to continuum region [64]. Cai *et al* [15] proposed a time-dependent condition based on Green's function to minimize the reflection across the interface. This method, due to computational intension, appears to be impractical for general problem. Huang *et.al* [26] have proposed a more practical matching conditions in atomistic-continuum modeling of materials. Utilizing renormalization group theory, Curtaloro and Ceder [17] have introduced a *MD* method with time and spatial coarse graining. Diestler *et al* [23] proposed an extension of the QC method to nonzero temperature to perform Monte Carlo simulation. The QC results match excellently with fully atomistic results. Using the framework of QC, Dupuy *et al* [25] developed a *MD* method without all the atoms.

3.6.1 Local Harmonic Approximation of Finite Temperature Effects

In this thesis, a finite-temperature QC method not involving *MD* or MC simulation is presented. The current model uses a local harmonic approximation to atom vibration to in local and nonlocal regions of the domain to approximate temperature effects in the material. At nonzero temperature(T), atoms will vibrate around the so-called *equilibrium* position. Therefore, the forces on atoms/nodes are determined by minimizing the Helmholtz free energy A , instead of the potential energy E . The Helmholtz free energy A is given by[16, 49]

$$A = E + k_B T \sum_{n=1}^{3N} \ln \left[2 \sinh \left(\frac{h\omega_n}{4\pi k_B T} \right) \right] \quad (3.36)$$

where E is the static lattice energy, N is the number of atoms, $k_B T$ is the thermal energy, k_B is the Boltzmann constant $1.3807 \times 10^{-23} JK^{-1}$, h is the Planck's constant, ω_n are the vibrations frequencies of the system and are determined from the static lattice energy E . The equation is referred as quasiharmonic(QH) approximation. The QH approach is known to be quite accurate and yield good agreements with the Monte Carlo simulation [30]. However,

the computational cost of QH is very expensive because of the processing of the $3N \times 3N$ dynamical matrix. To reduce the computational intensity, Lesar *etal* [49] introduced the local harmonic(LH) approximation by neglecting all terms that couple vibration of different atoms. Therefore, each atom acts as an Einstein oscillator. The vibration frequencies of independent atom i are determined by diagonalizing the 3×3 local dynamical matrix of atom i . In LH method the equation (3.36) then can be simplified as [16, 49]

$$A = E + 3k_B T \sum_{i=1}^N \ln \left[\frac{\|\mathbf{D}^i\|^{1/6}}{k_B T} \right] \quad (3.37)$$

where $\|\mathbf{D}^i\|$ is the determinant of the dynamical matrix of atom i . The local dynamical matrix of atom i is given by[103]

$$D_{pq}^i = \frac{\partial^2 E_{tot}}{\partial x_p^i \partial x_q^i} \quad (3.38)$$

Several studies [30, 49, 66, 103] have shown that local harmonic method is reasonably accurate up to half the melting temperature.

The Constitutive Model for Continuum at Finite Temperature

To account for the effect of temperature in continuum scale material model, the static lattice energy E is replaced by the Helmholtz free energy A . Due to the energetic equivalence of atoms under Cauchy-Born rule, the Helmholtz free energy in equation (3.37) can be rewritten as

$$A(F, T) = N \left(E_i + 3k_B T \ln \left[\frac{\|\mathbf{D}^i\|^{1/6}}{k_B T} \right] \right) \quad (3.39)$$

The Helmholtz free energy per unit volume is the energy density at finite temperature [100]

$$W(F, T) = \frac{A}{N\Omega_\epsilon} = \frac{1}{\Omega_\epsilon} \left(E_i + 3k_B T \ln \left[\frac{\|\mathbf{D}^i\|^{1/6}}{k_B T} \right] \right) \quad (3.40)$$

Partial derivative of energy density with respect to the deformation gradient \mathbf{F} gives the first Piola-Kirchhoff stress \mathbf{T}

$$\begin{aligned} T_{rS} &= \frac{\partial W}{\partial F_{rS}} \\ &= \frac{1}{\Omega_\epsilon} \frac{\partial E_i}{\partial F_{rS}} + \frac{1}{\Omega_\epsilon} 3k_B T \frac{1}{6} \frac{1}{\|\mathbf{D}^i\|} \frac{\partial \|\mathbf{D}^i\|}{\partial F_{rS}} \\ &= \frac{1}{\Omega_\epsilon} \frac{\partial E_i}{\partial F_{rS}} + \frac{1}{2} \frac{1}{\Omega_\epsilon} k_B T \frac{1}{\|\mathbf{D}^i\|} \text{adj}(D^i)_{pq} \frac{\partial \mathbf{D}_{pq}^i}{\partial F_{rS}} \end{aligned} \quad (3.41)$$

where $\text{adj}(\mathbf{D}^i)$ is the adjugate of matrix \mathbf{D}^i . The first term on the right-hand side is the contribution due to static lattice energy, the same as in previous sections. The second term is the contribution due to thermal energy. The equation (3.41) is constitutive relation for a centrosymmetric atomic structure at finite temperature.

The above formulation is for general interatomic potentials. Now let us incorporate the EAM potentials into equation (3.41). Recall the following EAM expressions

$$E_{tot} = \sum_{i=1}^N E_i \quad (3.42)$$

$$E_i = F_i(\bar{\rho}_i) + \frac{1}{2} \sum_{j \neq i}^{r_{ij} \leq r_{cut}} V_{ij}(r_{ij}) \quad (3.43)$$

$$\bar{\rho}_i = \sum_{j \neq i}^{r_{ij} \leq r_{cut}} \rho_j(r_{ij}) \quad (3.44)$$

The local dynamical matrix of atom i then becomes

$$\begin{aligned} D_{pq}^i &= \frac{\partial^2 E_{tot}}{\partial x_p^i \partial x_q^i} = \frac{\partial^2}{\partial x_p^i \partial x_q^i} \left[E_i + \sum_{j \neq i}^{r_{ij} \leq r_{cut}} E_j \right] \\ &= \frac{\partial}{\partial x_q^i} \left[\frac{\partial E_i}{\partial x_p^i} + \sum_{j \neq i}^{r_{ij} \leq r_{cut}} \frac{\partial E_j}{\partial x_p^i} \right] \\ &= \frac{\partial}{\partial x_q^i} \left[\sum_{j \neq i}^{r_{ij} \leq r_{cut}} \left(F'(\bar{\rho}_i) \rho'(r_{ij}) + F'(\bar{\rho}_j) \rho'(r_{ij}) + V'(r_{ij}) \right) \frac{\partial r_{ij}}{\partial x_p^i} \right] \\ &= \sum_{j \neq i}^{r_{ij} \leq r_{cut}} \left[F'(\bar{\rho}_i) \rho'(r_{ij}) + F'(\bar{\rho}_j) \rho'(r_{ij}) + V'(r_{ij}) \right] \frac{\partial^2 r_{ij}}{\partial x_p^i \partial x_q^i} \\ &+ \sum_{j \neq i}^{r_{ij} \leq r_{cut}} \left[\left(F'(\bar{\rho}_i) + F'(\bar{\rho}_j) \right) \rho''(r_{ij}) + V''(r_{ij}) + F''(\bar{\rho}_j) \rho'(r_{ij}) \rho'(r_{ij}) \right] \frac{\partial r_{ij}}{\partial x_q^i} \frac{\partial r_{ij}}{\partial x_p^i} \\ &+ \sum_{j \neq i}^{r_{ij} \leq r_{cut}} \left[F''(\bar{\rho}_i) \left(\sum_{k \neq i}^{r_{ik} \leq r_{cut}} \frac{\partial \rho}{\partial r_{ik}} \frac{\partial r_{ik}}{\partial x_q^i} \right) \rho'(r_{ij}) \right] \frac{\partial r_{ij}}{\partial x_p^i} \end{aligned} \quad (3.45)$$

where ($i \neq j$, no sum on i and j)

$$\frac{\partial r_{ij}}{\partial x_p^i} = \frac{1}{r_{ij}} (x_p^i - x_p^j) \quad (3.46)$$

$$\frac{\partial^2 r_{ij}}{\partial x_p^i \partial x_q^i} = \frac{1}{r_{ij}} \delta_{pq} - \frac{1}{r_{ij}^3} (x_p^i - x_p^j)(x_q^i - x_q^j) \quad (3.47)$$

The derivative of dynamical matrix with respect to deformation gradient is given by

$$\begin{aligned} \frac{\partial \mathbf{D}_{pq}^i}{\partial F_{LM}} &= \frac{\partial}{\partial F_{LM}} \left\langle \frac{\partial^2 U_{tot}}{\partial x_p^i \partial x_q^i} \right\rangle \\ &= \frac{\partial}{\partial F_{LM}} \left\langle \sum_{j \neq i}^{r_{ij} \leq r_{cut}} \left[F'(\bar{\rho}_i) \rho'(r_{ij}) + F'(\bar{\rho}_j) \rho'(r_{ij}) + V'(r_{ij}) \right] \frac{\partial^2 r_{ij}}{\partial x_p^i \partial x_q^i} \right\rangle \end{aligned}$$

$$\begin{aligned}
& + \frac{\partial}{\partial F_{LM}} \left\langle \sum_{j \neq i}^{r_{ij} \leq r_{cut}} \left[\left(F'(\bar{\rho}_i) + F'(\bar{\rho}_j) \right) \rho''(r_{ij}) + V''(r_{ij}) + F''(\bar{\rho}_j) \rho'(r_{ij}) \rho'(r_{ij}) \right] \frac{\partial r_{ij}}{\partial x_p^i} \frac{\partial r_{ij}}{\partial x_q^i} \right\rangle \\
& + \frac{\partial}{\partial F_{LM}} \left\langle \sum_{j \neq i}^{r_{ij} \leq r_{cut}} \left[F''(\bar{\rho}_i) \left(\sum_{k \neq i}^{r_{ik} \leq r_{cut}} \frac{\partial \rho}{\partial r_{ik}} \frac{\partial r_{ik}}{\partial x_q^i} \right) \rho'(r_{ij}) \right] \frac{\partial r_{ij}}{\partial x_p^i} \right\rangle \\
& = S1 + S2 + S3
\end{aligned} \tag{3.48}$$

where

$$\begin{aligned}
S1 & = \sum_{j \neq i}^{r_{ij} \leq r_{cut}} \left[F'(\bar{\rho}_i) \rho''(r_{ij}) + F'(\bar{\rho}_j) \rho''(r_{ij}) + V''(r_{ij}) \right] \frac{\partial r_{ij}}{\partial F_{LM}} \frac{\partial^2 r_{ij}}{\partial x_p^i \partial x_q^i} \\
& + \sum_{j \neq i}^{r_{ij} \leq r_{cut}} \left[F''(\bar{\rho}_i) \frac{\partial \bar{\rho}_i}{\partial F_{LM}} \rho'(r_{ij}) + F''(\bar{\rho}_j) \frac{\partial \bar{\rho}_j}{\partial F_{LM}} \rho'(r_{ij}) \right] \frac{\partial^2 r_{ij}}{\partial x_p^i \partial x_q^i} \\
& + \sum_{j \neq i}^{r_{ij} \leq r_{cut}} \left[F'(\bar{\rho}_i) \rho'(r_{ij}) + F'(\bar{\rho}_j) \rho'(r_{ij}) + V'(r_{ij}) \right] \frac{\partial^3 r_{ij}}{\partial x_p^i \partial x_q^i \partial F_{LM}}
\end{aligned} \tag{3.49}$$

$$\begin{aligned}
S2 & = \sum_{j \neq i}^{r_{ij} \leq r_{cut}} \left[F'(\bar{\rho}_i) \rho'''(r_{ij}) + F'(\bar{\rho}_j) \rho'''(r_{ij}) + V'''(r_{ij}) + 2F''(\bar{\rho}_j) \rho''(r_{ij}) \rho'(r_{ij}) \right] \frac{\partial r_{ij}}{\partial F_{LM}} \frac{\partial r_{ij}}{\partial x_q^i} \frac{\partial r_{ij}}{\partial x_p^i} \\
& + \sum_{j \neq i}^{r_{ij} \leq r_{cut}} \left[F''(\bar{\rho}_i) \frac{\partial \bar{\rho}_i}{\partial F_{LM}} \rho''(r_{ij}) + F''(\bar{\rho}_j) \frac{\partial \bar{\rho}_j}{\partial F_{LM}} \rho''(r_{ij}) + F'''(\bar{\rho}_j) \frac{\partial \bar{\rho}_j}{\partial F_{LM}} \rho'(r_{ij}) \rho'(r_{ij}) \right] \frac{\partial r_{ij}}{\partial x_q^i} \frac{\partial r_{ij}}{\partial x_p^i} \\
& + \sum_{j \neq i}^{r_{ij} \leq r_{cut}} \left[\left(F'(\bar{\rho}_i) + F'(\bar{\rho}_j) \right) \rho''(r_{ij}) + V''(r_{ij}) + F''(\bar{\rho}_j) \rho'(r_{ij}) \rho'(r_{ij}) \right] \\
& \left[\frac{\partial^2 r_{ij}}{\partial x_q^i \partial F_{LM}} \frac{\partial r_{ij}}{\partial x_p^i} + \frac{\partial r_{ij}}{\partial x_q^i} \frac{\partial^2 r_{ij}}{\partial x_p^i \partial F_{LM}} \right]
\end{aligned} \tag{3.50}$$

$$\begin{aligned}
S3 & = \sum_{j \neq i}^{r_{ij} \leq r_{cut}} \left[F'''(\bar{\rho}_i) \frac{\partial \bar{\rho}_i}{\partial F_{LM}} \left(\sum_{k \neq i}^{r_{ik} \leq r_{cut}} \frac{\partial \rho}{\partial r_{ik}} \frac{\partial r_{ik}}{\partial x_q^i} \right) \rho'(r_{ij}) \right] \frac{\partial r_{ij}}{\partial x_p^i} \\
& + \sum_{j \neq i}^{r_{ij} \leq r_{cut}} \left[F''(\bar{\rho}_i) \left(\sum_{k \neq i}^{r_{ik} \leq r_{cut}} \left\langle \frac{\partial^2 \rho}{\partial^2 r_{ik}} \frac{\partial r_{ik}}{\partial x_q^i} \frac{\partial r_{ik}}{\partial F_{LM}} + \frac{\partial \rho}{\partial r_{ik}} \frac{\partial^2 r_{ik}}{\partial x_q^i \partial F_{LM}} \right\rangle \right) \rho'(r_{ij}) \right] \frac{\partial r_{ij}}{\partial x_p^i} \\
& + \sum_{j \neq i}^{r_{ij} \leq r_{cut}} \left[F''(\bar{\rho}_i) \left(\sum_{k \neq i}^{r_{ik} \leq r_{cut}} \frac{\partial \rho}{\partial r_{ik}} \frac{\partial r_{ik}}{\partial x_q^i} \right) \rho''(r_{ij}) \frac{\partial r_{ij}}{\partial F_{LM}} \right] \frac{\partial r_{ij}}{\partial x_p^i} \\
& + \sum_{j \neq i}^{r_{ij} \leq r_{cut}} \left[F''(\bar{\rho}_i) \left(\sum_{k \neq i}^{r_{ik} \leq r_{cut}} \frac{\partial \rho}{\partial r_{ik}} \frac{\partial r_{ik}}{\partial x_q^i} \right) \rho'(r_{ij}) \right] \frac{\partial^2 r_{ij}}{\partial x_p^i \partial F_{LM}}
\end{aligned} \tag{3.51}$$

$$\frac{\partial \bar{\rho}_i}{\partial F_{LM}} = \sum_{k \neq i}^{r_{ik} \leq r_{cut}} \frac{\partial \rho}{\partial r_{ik}} \frac{\partial r_{ik}}{\partial F_{LM}} \tag{3.52}$$

$$\frac{\partial r_{ij}}{\partial F_{lM}} = \frac{(x_l^i - x_l^j)(X_M^i - X_M^j)}{r_{ij}} \quad (3.53)$$

$$\frac{\partial^2 r_{ij}}{\partial x_p^i \partial F_{lM}} = \frac{\delta_{pl}(X_M^i - X_M^j)}{r_{ij}} - \frac{(x_l^i - x_l^j)(X_M^i - X_M^j)(x_p^i - x_p^j)}{r_{ij}^3} \quad (3.54)$$

$$\begin{aligned} \frac{\partial^3 r_{ij}}{\partial x_p^i \partial x_q^j \partial F_{lM}} &= -\frac{(X_M^i - X_M^j)}{r_{ij}^3} [\delta_{ql}(x_p^i - x_p^j) + \delta_{pl}(x_q^i - x_q^j) + \delta_{pq}(x_l^i - x_l^j)] \\ &\quad + \frac{3}{r_{ij}^5} (X_M^i - X_M^j)(x_l^i - x_l^j)(x_p^i - x_p^j)(x_q^i - x_q^j) \end{aligned} \quad (3.55)$$

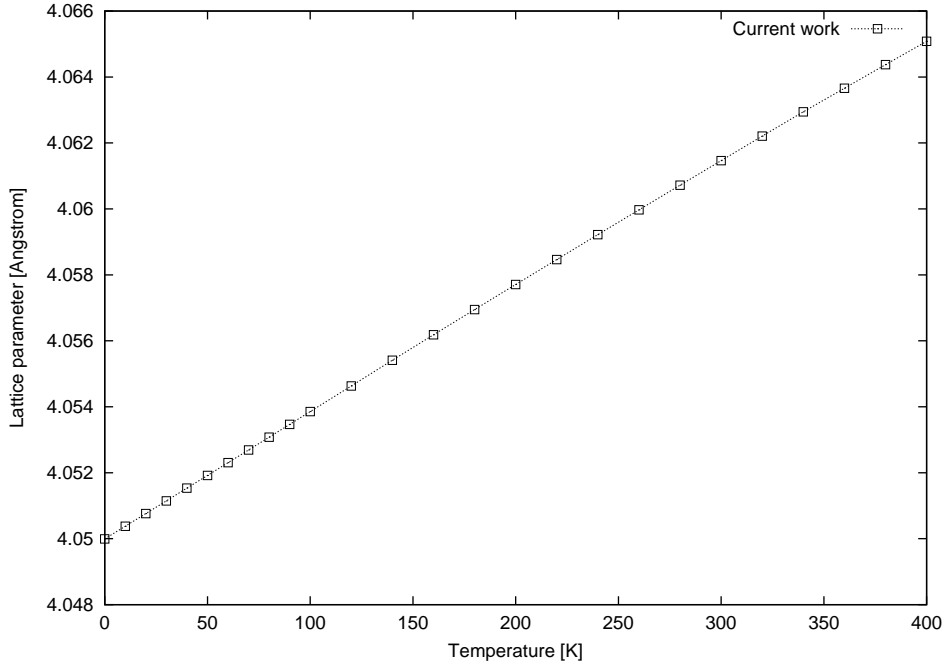


Figure 3.6: Effect of temperature on the lattice parameter of single crystal aluminum

The resulting continuum model is used to analyze the lattice structure of *FCC* aluminum using EAM potential in [62]. The lattice parameter a_0 , that characterizes the primitive cube corners of the crystal, is obtained by calculating the 1st Piola-Kirchoff stress \mathbf{T} at various values of a_0 at zero deformation gradient, i.e. by calculating $\mathbf{T}(a_0)|_{\mathbf{F}=\mathbf{I}} = \left. \frac{\partial U(a_0)}{\partial \mathbf{F}} \right|_{\mathbf{F}=\mathbf{I}}$. Since the material is expected to be stress free at unit deformation gradient, the lattice parameter of the material can now be obtained from the equation $\mathbf{T}(a_0) = \mathbf{0}$. The equilibrium lattice constant of $a_0 = 4.050\text{\AA}$ and the elastic moduli predicted by this potential $C_{11} = 113.68\text{ GPa}$, $C_{12} = 61.43\text{ GPa}$, and $C_{44} = 31.60\text{ GPa}$ are very close to those in [62]. This result can be compared to material properties of single crystal aluminum in [34]. These analytical predictions, are written in material properties such as shear modulus μ and Poisson ratio ν and effective values for the parameters were computed from C_{11} , C_{12} , and C_{44} by performing a Voigt average. The invariants of the elastic modulus tensor computed from the effective isotropic moduli by

Voigt average are the same as those from the anisotropic moduli [34]. The relations for effective parameters are

$$\begin{aligned}\mu &= \frac{1}{5} (C_{11} - C_{12} + 3C_{44}) \\ \nu &= \frac{1}{2} \left[\frac{C_{11} + 4C_{12} - 2C_{44}}{2C_{11} + 3C_{12} + C_{44}} \right]\end{aligned}\quad (3.56)$$

which give $\mu = 29.41\text{GPa}$ and $\nu = 0.334$ for Mishin Aluminum. Finally the effect of temperature on the lattice parameter is depicted in figure 3.6.

The Forces on Atoms at Finite Temperature

The partial derivative of Helmholtz free energy(3.37) with respect to the displacement of atom l gives the forces on atom l

$$\begin{aligned}f_r^l &= \frac{\partial A}{\partial x_r^l} \\ &= \frac{\partial E_{tot}}{\partial x_r^l} + 3k_B T \sum_{i=1}^N \frac{1}{6} \frac{1}{\|\mathbf{D}^i\|} \frac{\partial \|\mathbf{D}^i\|}{\partial x_r^l} \\ &= \frac{\partial E_{tot}}{\partial x_r^l} + \frac{1}{2} k_B T \sum_{i=1}^N \frac{1}{\|\mathbf{D}^i\|} \text{adj}(D^i)_{pq} \frac{\partial \mathbf{D}_{pq}^i}{\partial x_r^l}\end{aligned}\quad (3.57)$$

The first term on the right-hand side is the contribution due to static lattice energy, the same as in previous chapter. The second term is the contribution due to thermal energy.

The derivative of dynamical matrix with respect to displacement of atom l is given by

$$\begin{aligned}\frac{\partial \mathbf{D}_{pq}^i}{\partial x_r^l} &= \frac{\partial}{\partial x_r^l} \left\langle \frac{\partial^2 U_{tot}}{\partial x_p^i \partial x_q^i} \right\rangle \\ &= \frac{\partial}{\partial x_r^l} \left\langle \sum_{j \neq i}^{r_{ij} \leq r_{cut}} \left[F'(\bar{\rho}_i) \rho'(r_{ij}) + F'(\bar{\rho}_j) \rho'(r_{ij}) + V'(r_{ij}) \right] \frac{\partial^2 r_{ij}}{\partial x_p^i \partial x_q^i} \right\rangle \\ &+ \frac{\partial}{\partial x_r^l} \left\langle \sum_{j \neq i}^{r_{ij} \leq r_{cut}} \left[\left(F'(\bar{\rho}_i) + F'(\bar{\rho}_j) \right) \rho''(r_{ij}) + V''(r_{ij}) + F''(\bar{\rho}_j) \rho'(r_{ij}) \rho'(r_{ij}) \right] \frac{\partial r_{ij}}{\partial x_p^i} \frac{\partial r_{ij}}{\partial x_q^i} \right\rangle \\ &+ \frac{\partial}{\partial x_r^l} \left\langle \sum_{j \neq i}^{r_{ij} \leq r_{cut}} \left[F''(\bar{\rho}_i) \left(\sum_{k \neq i}^{r_{ik} \leq r_{cut}} \frac{\partial \rho}{\partial r_{ik}} \frac{\partial r_{ik}}{\partial x_q^i} \right) \rho'(r_{ij}) \right] \frac{\partial r_{ij}}{\partial x_p^i} \right\rangle \\ &= SA1 + SA2 + SA3\end{aligned}\quad (3.58)$$

where

$$SA1 = \sum_{j \neq i}^{r_{ij} \leq r_{cut}} \left[F'(\bar{\rho}_i) \rho''(r_{ij}) + F'(\bar{\rho}_j) \rho''(r_{ij}) + V''(r_{ij}) \right] \frac{\partial r_{ij}}{\partial x_r^l} \frac{\partial^2 r_{ij}}{\partial x_p^i \partial x_q^i}$$

$$\begin{aligned}
& + \sum_{j \neq i}^{r_{ij} \leq r_{cut}} \left[F''(\bar{\rho}_i) \frac{\partial \bar{\rho}_i}{\partial x_r^l} \rho'(r_{ij}) + F''(\bar{\rho}_j) \frac{\partial \bar{\rho}_j}{\partial x_r^l} \rho'(r_{ij}) \right] \frac{\partial^2 r_{ij}}{\partial x_p^i \partial x_q^i} \\
& + \sum_{j \neq i}^{r_{ij} \leq r_{cut}} \left[F'(\bar{\rho}_i) \rho'(r_{ij}) + F'(\bar{\rho}_j) \rho'(r_{ij}) + V'(r_{ij}) \right] \frac{\partial^3 r_{ij}}{\partial x_p^i \partial x_q^i \partial x_r^l} \tag{3.59}
\end{aligned}$$

$$\begin{aligned}
SA2 = & \sum_{j \neq i}^{r_{ij} \leq r_{cut}} \left[F'(\bar{\rho}_i) \rho'''(r_{ij}) + F'(\bar{\rho}_j) \rho'''(r_{ij}) + V'''(r_{ij}) + 2F''(\bar{\rho}_j) \rho''(r_{ij}) \rho'(r_{ij}) \right] \frac{\partial r_{ij}}{\partial x_r^l} \frac{\partial r_{ij}}{\partial x_q^i} \frac{\partial r_{ij}}{\partial x_p^i} \\
& + \sum_{j \neq i}^{r_{ij} \leq r_{cut}} \left[F''(\bar{\rho}_i) \frac{\partial \bar{\rho}_i}{\partial x_r^l} \rho''(r_{ij}) + F''(\bar{\rho}_j) \frac{\partial \bar{\rho}_j}{\partial x_r^l} \rho''(r_{ij}) + F'''(\bar{\rho}_j) \frac{\partial \bar{\rho}_j}{\partial x_r^l} \rho'(r_{ij}) \rho'(r_{ij}) \right] \frac{\partial r_{ij}}{\partial x_q^i} \frac{\partial r_{ij}}{\partial x_p^i} \\
& + \sum_{j \neq i}^{r_{ij} \leq r_{cut}} \left[\left(F'(\bar{\rho}_i) + F'(\bar{\rho}_j) \right) \rho''(r_{ij}) + V''(r_{ij}) + F''(\bar{\rho}_j) \rho'(r_{ij}) \rho'(r_{ij}) \right] \\
& \left[\frac{\partial^2 r_{ij}}{\partial x_q^i \partial x_r^l} \frac{\partial r_{ij}}{\partial x_p^i} + \frac{\partial r_{ij}}{\partial x_q^i} \frac{\partial^2 r_{ij}}{\partial x_p^i \partial x_r^l} \right] \tag{3.60}
\end{aligned}$$

$$\begin{aligned}
SA3 = & \sum_{j \neq i}^{r_{ij} \leq r_{cut}} \left[F'''(\bar{\rho}_i) \frac{\partial \bar{\rho}_i}{\partial x_r^l} \left(\sum_{k \neq i}^{r_{ik} \leq r_{cut}} \frac{\partial \rho}{\partial r_{ik}} \frac{\partial r_{ik}}{\partial x_q^i} \right) \rho'(r_{ij}) \right] \frac{\partial r_{ij}}{\partial x_p^i} \\
& + \sum_{j \neq i}^{r_{ij} \leq r_{cut}} \left[F''(\bar{\rho}_i) \left(\sum_{k \neq i}^{r_{ik} \leq r_{cut}} \left\langle \frac{\partial^2 \rho}{\partial^2 r_{ik}} \frac{\partial r_{ik}}{\partial x_q^i} \frac{\partial r_{ik}}{\partial x_r^l} + \frac{\partial \rho}{\partial r_{ik}} \frac{\partial^2 r_{ik}}{\partial x_q^i \partial x_r^l} \right\rangle \right) \rho'(r_{ij}) \right] \frac{\partial r_{ij}}{\partial x_p^i} \\
& + \sum_{j \neq i}^{r_{ij} \leq r_{cut}} \left[F''(\bar{\rho}_i) \left(\sum_{k \neq i}^{r_{ik} \leq r_{cut}} \frac{\partial \rho}{\partial r_{ik}} \frac{\partial r_{ik}}{\partial x_q^i} \right) \rho''(r_{ij}) \frac{\partial r_{ij}}{\partial x_r^l} \right] \frac{\partial r_{ij}}{\partial x_p^i} \\
& + \sum_{j \neq i}^{r_{ij} \leq r_{cut}} \left[F''(\bar{\rho}_i) \left(\sum_{k \neq i}^{r_{ik} \leq r_{cut}} \frac{\partial \rho}{\partial r_{ik}} \frac{\partial r_{ik}}{\partial x_q^i} \right) \rho'(r_{ij}) \right] \frac{\partial^2 r_{ij}}{\partial x_p^i \partial x_r^l} \tag{3.61}
\end{aligned}$$

$$\frac{\partial \bar{\rho}_i}{\partial x_r^l} = \sum_{k \neq i}^{r_{ik} \leq r_{cut}} \frac{\partial \rho}{\partial r_{ik}} \frac{\partial r_{ik}}{\partial x_r^l} \tag{3.62}$$

$$\frac{\partial r_{ij}}{\partial x_r^l} = \frac{(x_r^i - x_r^j)}{r_{ij}} (\delta_{il} - \delta_{jl}) \tag{3.63}$$

$$\frac{\partial^2 r_{ij}}{\partial x_p^i \partial x_r^l} = -\frac{(\delta_{il} - \delta_{jl})}{r_{ij}^3} (x_r^i - x_r^j) (x_p^i - x_p^j) + \frac{(\delta_{il} - \delta_{jl})}{r_{ij}} \delta_{pr} \tag{3.64}$$

$$\begin{aligned}
\frac{\partial^3 r_{ij}}{\partial x_p^i \partial x_q^i \partial x_r^l} = & -\frac{3}{r_{ij}^5} (x_q^i - x_q^j) (x_p^i - x_p^j) (x_r^i - x_r^j) (\delta_{il} - \delta_{jl}) \\
& - \frac{(\delta_{il} - \delta_{jl})}{r_{ij}^3} [\delta_{pq} (x_r^i - x_r^j) + \delta_{qr} (x_p^i - x_p^j) + \delta_{pr} (x_q^i - x_q^j)] \tag{3.65}
\end{aligned}$$

With the effect of temperature incorporated into local and nonlocal parts of the computational model, numerical simulation of the coupled QC method follows the development in section 3.5. Various examples to demonstrate the effectiveness of the method are presented in the next chapter.

Chapter 4

Nanoindentation Problems at Finite Temperatures

4.1 Introduction

The indentation test is widely used to assess the hardness in the materials industry. In nanoindentation experiments, a nanoscale indenter is pressed on the material to generate dislocations within the material. Nanoindentation is therefore a powerful way to investigate incipient plasticity at the atomistic scale of the material. Important mechanical properties, such as elastic moduli, hardness, flow strength can be obtained through such a nanoindentation experiment [68]. An understanding of those properties is critical in the design of such materials.

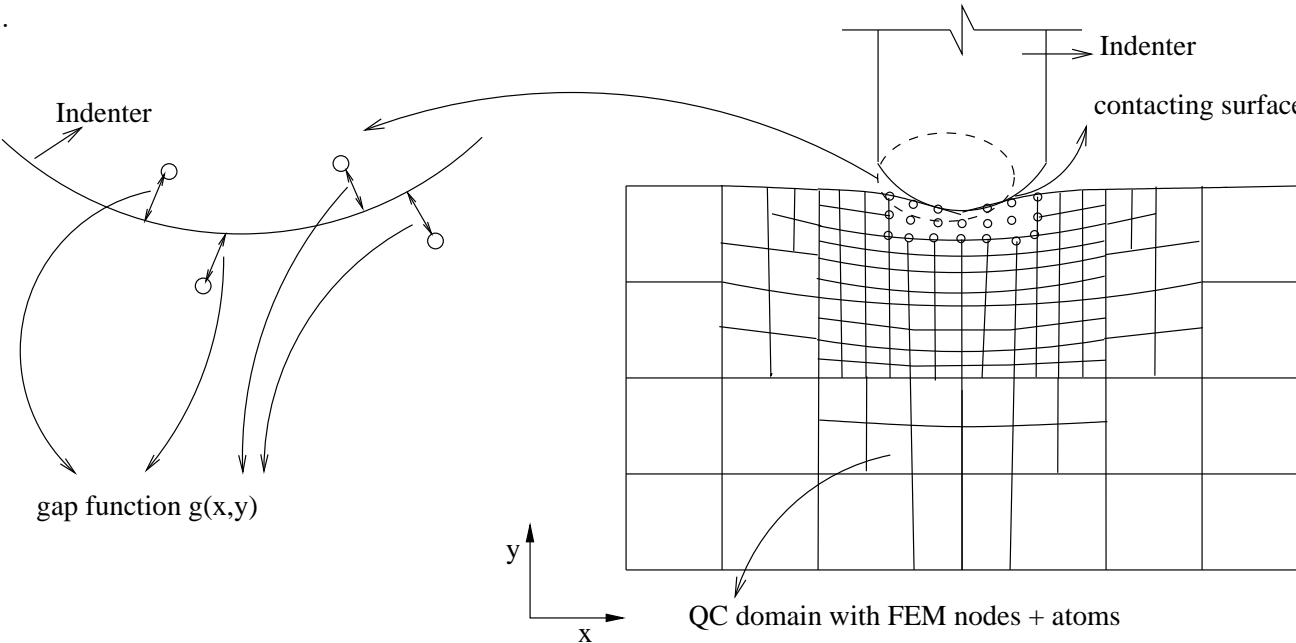


Figure 4.1: Schematic of the computational model used in a nanoindentation experiment

Literally, the nanoindentation is an extension of classical indentation problem to a length scale where the mechanics of the material is governed by atomistic interactions. In classical

indentation, the large plastic region formed beneath the indenter is used to generate the yield strength of the material using semiempirical formulations [68]. In nanoindentation there is no large-scale plasticity. Instead, early discrete dislocations under the indenter generated at threshold loads are used as indicators for the onset of plasticity.

There are many experimental studies of nanoindentation [7, 36, 55, 60, 86, 98]. Those experiments offer useful information on the onset of the plasticity. Some difficulties emerge in analysis of nanoindentation test data. These include the tip geometrical imperfections of the indenter and the definition of the contact area [29]. Therefore, numerical simulations of nanoindentation tests can be a helpful tool for better understanding the influence of the collective behavior of dislocations. In nanoindentation tests, the size of the residual impression is too small to be measured directly. Thus, the contact areas are obtained from recorded depth together with a known geometry of the indenters [29]. In general, sharp, geometrically-similar indenters such as the Berkovich triangular pyramid are useful when one wishes to probe properties at the smallest possible scale. The Berkovich indenter has the advantage that the edges of the pyramid are more easily constructed to meet at a single point than Vickers pyramid. Spherical indenters are also frequently employed in nanoindentation tests. The main advantage of the spherical indenter is that it provides a smooth transition from elastic to elastic-plastic contact. Another reason for interest in spherical indenters is that even the sharpest Berkovich diamonds are not perfectly sharp but have a tip radius in the order of 10-100nm [71]. Due to the complicated stress distribution in the neighborhood of the indenter, interpretation of nanoindentation experiments at fundamental level is still challenging. Computer simulations have been very useful for a clear understanding of the process taking place during the test. Recently there have been many studies on nanoindentation by using molecular dynamics(*MD*) simulation [110]. Those studies provided good understanding of atomistic mechanisms in nanoindentation response. However, the *MD* simulation faces some serious challenges. These include the large computational cost which in turn could results in small model sizes. Some investigators have studied the nanoindentation process using finite element method [4, 33, 51, 105]. A number of atomistic simulation of nanoindentation have been conducted in recent years[42, 110]. Tadmor et al.[92] used the QC method to study two-dimension nanoindentation. Knap and Ortiz [45] used the QC method to study effect of indenter-radius size on Au(001) nanoindentation.

In this chapter we use the finite temperature QC method, developed in this dissertation, to model typical nanoindentation experiments. The results are meant to demonstrate the efficacy of the developed computational in dislocation generation and motion for indenters of different shapes in 2D and 3D problems.

4.2 Contact Algorithm for Indentation Problem

In a typical indentation experiment, shown in figure 4.1, indenter of spherical or conical or cylindrical shapes are used to generate dislocations along the contact surface. In order to account for varied indenter shapes, a suitable contact algorithm needs to be incorporated into the coupled *QC* finite element procedure developed in chapter 2&3. Figure (4.1) shows the effect of an indenter on the material surface. Global surfaces/atoms of the material domain under an

indenter are constrained to move normal to the indenter surface. On the other hand regions away from the indenter are expected to move such that they do not penetrate the indenter. The resulting contact problem is a system subject to inequality constraints that need to be applied on the global *DOF* $\{\mathbf{D}\}$ of the computational model. The pivotal issue of the contact formulation is the method used to convert the associated inequalities constraint into a tractable system of algebraic equation. Most proposed techniques can be broken down into two broad categories: the method of Lagrange multipliers and the penalty method. In these iterative methods, *DOF* directly under the indenter are assumed to be on the contact surface (equality constraint with zero gap between indenter and *DOF*). The remaining portion of the material domain is assumed to satisfy the the inequality constraint (positive gap function) apriori. If the computational solution is such that non contacting regions penetrate the indenter, they are made into contacting *DOF* and the computational model is resolved iteratively until the exact contacting surface is obtained. The perturbed Lagrangian formulation is a mixed method which introduces a quadratic term to classical Lagrangian functional to regularize the penalty formulation [87]. Various aspects of this formulation are considered next.

4.2.1 Perturbed Lagrange Formulation

Let $\partial\Omega_i$ be the boundary of the indenter. Further, let $g(\mathbf{x})$ be the gap between the nodes/atoms and indenter, $\partial\Omega_C$ be the contact surface, λ be the contact force acting on C . The contact condition may be expressed in a Kuhn-Tucker form as

$$g\lambda = 0, \lambda \leq 0, g \geq 0 \quad (4.1)$$

Let $\bar{\Pi}$ be the total potential energy associated with the structure underneath the indenter. The mixed penalty functional Π_ϵ is defined as [87]

$$\Pi_\epsilon = \bar{\Pi} + \sum_{j=1}^m \lambda_j g_j - \frac{1}{2\epsilon} \sum_{j=1}^m \lambda_j^2 \quad (4.2)$$

where m is the number of contact nodes, ϵ is a large positive parameter. The last term in equation (4.2) is to regularize the classical Lagrangian. The functional Π_ϵ is referred as a perturbed Lagrangian. As $\epsilon \rightarrow \infty$ the solution from 4.2 will converges to the solution obtained by classical Lagrange multiplier method. The stiffness matrix obtained from classical Lagrange multiplier method, corresponding to $\frac{1}{\epsilon} = 0$, always has a zero diagonal terms which makes the solving precess more complicated. The additional penalty term regularizes the system by generating positive definite stiffness matrix for the discrete problem.

Variation of the functional Π_ϵ is given by

$$\delta\Pi_\epsilon = \delta\bar{\Pi} + \sum_{j=1}^m (\delta\lambda_j g_j + \lambda_j \delta g_j) - \frac{1}{\epsilon} \sum_{j=1}^m \lambda_j \delta\lambda_j \quad (4.3)$$

To make the perturbed Lagrangian Π_ϵ stationary, one gets the following equations

$$\sum_e \int_{\Omega_e} [B]^T \{T\} dV + \sum_j \lambda_j \frac{\partial g}{\partial \mathbf{x}} = 0 \quad (4.4)$$

$$g_j - \frac{1}{\epsilon} \lambda_j = 0 \quad j=1, \dots, m \quad (4.5)$$

The first term in equation (4.4) is the nodal force vector due to deformation in the specimen; the second term in the equation is contribution to force vector due to contacts. The equation (4.5) is the non-penetration condition when $\epsilon \rightarrow \infty$. If the # DOF in a problem is denoted by NQ , there are m additional unknowns (i.e. contact forces $\lambda_j, j = 1, \dots, m$, m is the number of contacts) from equation (4.5). Therefore, the total number of DOF in the system will be $NQ+m$.

The above equations are nonlinear and need to be solved iteratively. Differentiating 4.4, 4.5 with respect to the unknowns (i.e. the displacements of the nodes and atoms and the contact forces), the stiffness matrix contribution due to contact j can be written as:

$$[K_{cont_1}^j] = \lambda_j \begin{bmatrix} \frac{\partial^2 g}{\partial x^2} & \frac{\partial^2 g}{\partial x \partial y} & \frac{\partial^2 g}{\partial x \partial z} \\ \frac{\partial^2 g}{\partial y \partial x} & \frac{\partial^2 g}{\partial y^2} & \frac{\partial^2 g}{\partial y \partial z} \\ \frac{\partial^2 g}{\partial z \partial x} & \frac{\partial^2 g}{\partial z \partial y} & \frac{\partial^2 g}{\partial z^2} \end{bmatrix}_{(x_j, y_j, z_j)} \quad (4.6)$$

$$\{K_{cont_2}^j\} = \left[\frac{\partial g}{\partial x} \quad \frac{\partial g}{\partial y} \quad \frac{\partial g}{\partial z} \right]_{(x_j, y_j, z_j)} \quad (4.7)$$

The diagonal entry in stiffness matrix corresponding to j th contact is $-\frac{1}{\epsilon}$.

Implementation of Perturbed Lagrangian Problem in Indentation Problem

In this dissertation, we assume the indenter is rigid with no interaction between the contact surfaces (friction-free conditions). When a material is acted upon by the indenter, the material particles on the contact surface should lie on the surfaces defined by the geometry of the indenter. Since a frictionless condition is assumed in the present work, no constraint is imposed on the tangential displacements at the interfaces. Also, since the indenter is assumed to be rigid, it is not necessary to model indenter deformation explicitly in the simulation. Instead, the vertical down-ward displacement can be used directly to describe the position of the whole indenter. The resulting constraint equation is imposed through a perturbed Lagrange formulation discussed in the previous section.

For a horizontal flat $2D$ indenter, the contact surface is:

$$(y - y_c) = 0 \quad (4.8)$$

where y_c is the vertical coordinate of the horizontal contacting surface. The resulting gap function can now be written as:

$$g(x, y) = y - y_c \quad (4.9)$$

with the gap function $g(x, y) \geq 0$ for any point not inside the indenter. Physically such a constraint implies impenetrability of the material domain into the rigid indenter. Similarly for a $2D$ cylindrical indenter, the contact surface is:

$$(x - x_c)^2 + (y - y_c)^2 - R^2 = 0 \quad (4.10)$$

where (x_c, y_c) is the coordinate of the center of the cylindrical indenter, R is the radius of the indenter. The resulting gap function can now be written as:

$$g(x, y) = (x - x_c)^2 + (y - y_c)^2 - R^2 \quad (4.11)$$

Using a similar methodology it is quite easy to show that the gap function for a 3D spherical indenter of radius R is given as:

$$g(x, y, z) = (x - x_c)^2 + (y - y_c)^2 + (z - z_c)^2 - R^2 \quad (4.12)$$

With the above gap functions, we can implement equation (4.4), 4.5 into the coupled QC finite element procedure developed in chapters 2&3. In the iterative procedure, the finite element program continually checks the status of each contact DOF, iteratively deleting and reinstating contact atoms/nodes as required, until force equilibrium is reached with an unchanging set of contact points. Theoretically, the penalty parameter ϵ in equation (4.5) should be assigned an infinite value to ensure a non-penetrating contact between the indenter and specimen. However, this is not possible in practice because of the finite numeric restrictions of computer hardware. Consequently, during contact, the indenter could possibly slightly intrude into the specimen by a small amount, which depends on the largeness of the penalty parameter. It is desirable at least to have the penalty parameter considerably larger than stiffness of the specimen material. If the penalty parameter is too low, then there is insufficient stiffness to enforce the contact condition. If the penalty parameter is too large, then there is numerical error due to the loss of information when a large quantity is added to a small one in the computer. A penalty parameter of ≈ 10000 times of stiffness of the specimen material is usually sufficient.

4.3 Applications to Nanoindentation Simulations

In these set of results, two different crystallographic orientations were studied for the nanoindentation of aluminum. In the first one the indenter was driven into a (001) surface of the crystal, while in the second one the indenter was pressed into a ($\bar{1}10$) surface. Besides the two different crystallographic orientations, two different indenter geometries were investigated. The first one is a rectangular indenter with a width of 250Å. The second indenter geometry was cylindrical indenter with a radius of 11.6Å. We note that the choice of indenter size was by choice and does reflect a fundamental limitation of the system sizes that the model can handle. For both indenter geometries the indenter was modeled as displacement boundary condition applied to the surface node/atoms lying underneath it. Therefore the indenter is rigid and there are no interactions between tip atoms and film atoms. Friction-free condition was considered between indenter and crystal. The substrate was modeled as a rigid surface allowing no displacements. The top surfaces(except the region right under the indenter) was left unconstrained.

Before we go to 2D QC simulation of indentation, the out-of-plane movements of nodes/atoms is briefly discussed.

4.3.1 Deformation in Out-of-plane Direction

Plain Strain Problem

In plain strain problem, the deformed shape of the material is limited to remain in-plane. There are no out-of-pane movements for neither nodes nor true atoms.

$$u_x = u_x(x, y)$$

$$\begin{aligned}
u_y &= u_y(x, y) \\
u_z &= 0
\end{aligned}
\tag{4.13}$$

The the unknowns are u_x and u_y . Although the analysis is performed in 2D coordinate system, the atoms are in a 3D atomistic environment. Specifically, each atom is surround by a sphere of neighbor atoms for the purpose of calculating atomic force and stiffness.

Generalized Plain Strain Problem

In generalized plain strain problem, the displacement fields are in-plane movements plus a uniform out-of-plane deformation.

$$\begin{aligned}
u_x &= u_x(x, y) \\
u_y &= u_y(x, y) \\
u_z &= \bar{u}z
\end{aligned}
\tag{4.14}$$

where \bar{u} is the so called out-of plane generalized plane strain. The the unknowns are u_x , u_y at all nodes/atom and \bar{u} which is a constant for the entire domain of analysis. Similarly, each atom is in 3D atomistic environment. In generalized plane strain for continuum problem, the sum of out-of-plane force is set to be zero for the purpose of solving out-of-plane deformation. If there are n nodes in the system, then we have $2n$ in-plane unknowns ($n u_x$ and $n u_y$) and one additional out-of-plane unknowns (\bar{u}). Correspondingly, we have $2n$ in-plane constrain equations($n f_x = 0$ and $n f_y = 0$) and one additional out-of-plane constrain equation($f_z = 0$). In this continuum/atomistic coupling model, the above assumptions still hold. The issue is how we calculate the out-of-plane force. For continuum region, we can calculate the deformation gradient for given in-plane displacement field plus a given out-of-plane deformation. Out-of-plane force contribution due to continuum region can be obtained with these deformation gradients. For atomic region, the calculation is based on repeating cells. As an example, the cell contains six atoms residing in cell position for an FCC crystal rotated into the $[111] - [\bar{1}10]$ coordinate system. The out-of plane force on those atoms in the repeating cell is from contribution of atoms in another half plane. The sum of these half-plane atomic forces is the out-of-plane force acted on the cell. Again, the sum over forces on all repeating cells is the out-of-plane force for atomic region. Adding up the out-of-plane force due to continuum region and atomic region, we get total out-of-plane force of the system. In the generalized plane strain problem, the unknown out-of plane strain \bar{u} is solved so as to render this out of plane force equal to zero.

4.3.2 2D Cylindrical Indenter

In this example a rigid cylindrical indenter, infinite in the out-of-plane direction, is pressed into a $(\bar{1}10)$ plane of the crystal as shown in figure 4.2. The radius of the indenter is $R = 11.64\text{\AA}$. Friction-free conditions were assumed between the indenter and the thin film. For the cylindrical indenter, the contact area increases with indentation depth and new atoms/nodes will occasionally come into contact with the indenter surface. To handle this we implement the contact algorithm discussed in the previous section.

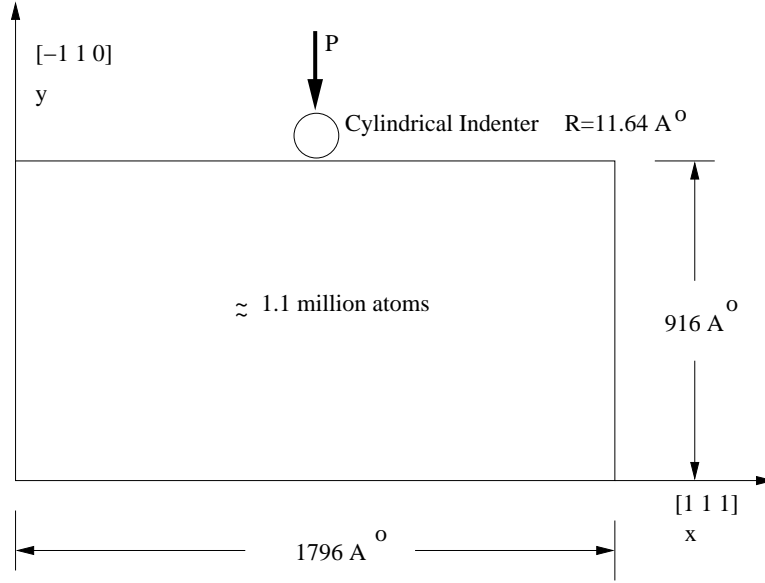


Figure 4.2: Nanoindentation in an aluminum single crystal with cylindrical indenter

The material assumed is *FCC* aluminum with *EAM* potentials obtained from [62]. As discussed in chapter 3, the equilibrium lattice constant at 0 K is $a_0 = 4.050\text{\AA}$. The elastic moduli predicted by this potential are $C_{11} = 113.68\text{ GPa}$, $C_{12} = 61.43\text{ GPa}$, and $C_{44} = 31.60\text{ GPa}$.

As the indenter is $[\bar{1}10]$ direction, the rotated *FCC* crystal into the $[111] - [\bar{1}10]$ coordinate system to get representative cell to be used in the analysis. The cell contains six representative atoms. The dimensions of the repeating cell then are $a_x = \sqrt{3}a$ for x direction; $a_y = 0.5\sqrt{6}a$ for y direction; $a_z = 0.5\sqrt{2}a$ for out-of-plane direction, where a is the lattice parameter for aluminum.

In this example, any element with strain energy error density larger than 1% of the average system strain energy is selected to be refined to next level. The elements on initial mesh (level 0) have dimension of $32a_x \times 32a_y$. Continuum elements could therefore exist as high as the 5th level. A element at 5th level, having dimension of $a_x \times a_y$ will be opened into atoms if needed. A series of the progressive mesh refinements for this problem are given in figure (4.3). Refinement through all 6 levels (upto atoms) occurred at the first step, with subsequent refinements skewed mainly from 5th-6th level. The QC model has 99 nodes in initial mesh. At final stage (1st dislocation) the QC model only includes 2,134 atoms plus 897 nodes (3011 total). The actual thin film contains around 1.1 million atoms, demonstrating the substantially reduced computational expense of the current method. At each load step, the indentation depth is increased by 0.1 \AA . This depth was chosen so as to prevent too many new contact points at each iteration step.

The atomic structures under indenter during the formation of the 1st dislocation is given in figure 4.4. The 1st Piola-Kirchhoff stress (T_{yy}) just before first dislocation is presented in figure 4.6. The load-displacement curve obtained from the simulation is plotted in figure 4.7. The loads are given in Newtons per meter length of the indenter in the out-of-plane direction. The result of Tadmor [92] is also plotted in the figure. The current predictions are in excellent

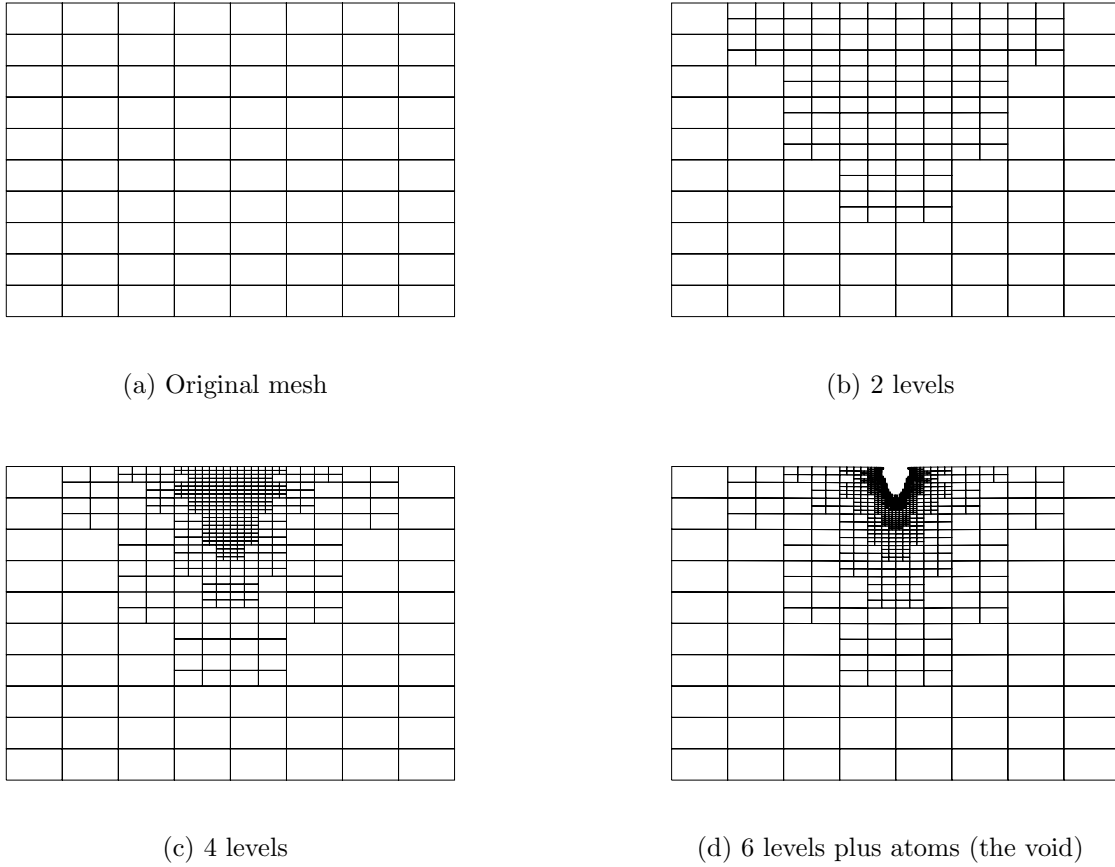


Figure 4.3: Automatic multi-scale mesh refinement generated for nanoindentation problem in figure 4.2

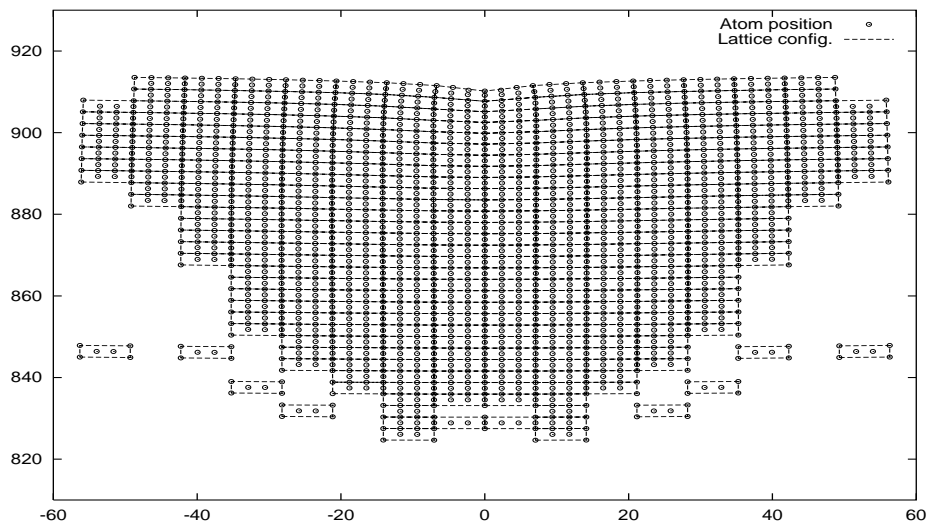


Figure 4.4: Atomic structure under indenter, just before nucleation of first defect, for nanoindentation problem in figure 4.2

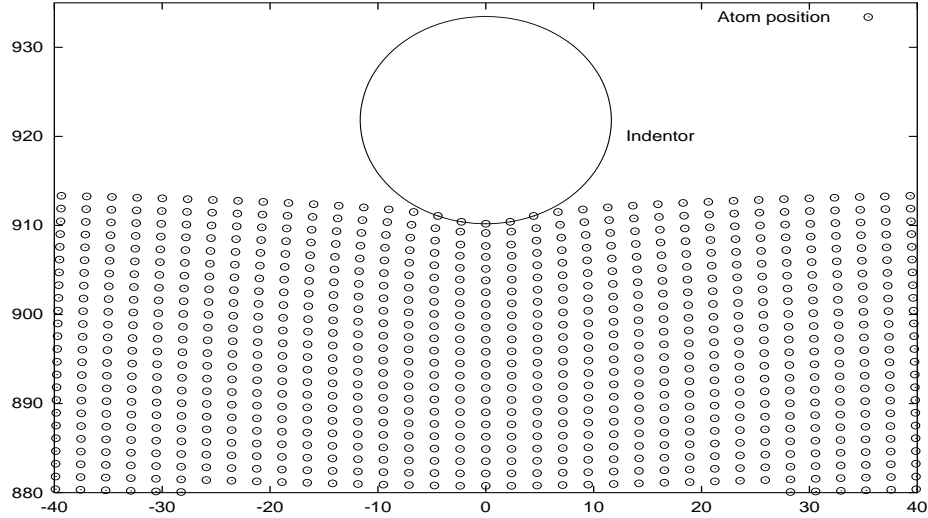


Figure 4.5: Atomic structure under indenter, just before nucleation of first defect, for nanoindentation problem in figure 4.2, a close look

agreement with the results in Tadmor[92] with both simulations predicting first dislocation at depth around 6.5 \AA .

For a cylindrical indenter, Hertz contact theory provides the relationship between indentation load P and the contact half-width a ,

$$a^2 = \frac{4PR}{\pi E^*} \quad (4.15)$$

where for rigid indenter,

$$E^* = \left(\frac{1 - \nu^2}{E} \right)^{-1} = \frac{2\mu}{(1 - \nu)} \quad (4.16)$$

Substituting equation 4.16 into equation 4.15, we have,

$$P = \frac{\pi\mu a^2}{2(1 - \nu)R} \quad (4.17)$$

Substituting in the corresponding values we got previously (i.e. $\mu = 29.41 \text{ GPa}$, $\nu = 0.334$, and $R = 11.64 \text{ \AA}$) yields $P = 0.600a^2$ with P taken in N/m and a obtained in \AA .

The load versus contact half-width obtained from equation (4.17) and that predicted by the simulation were compared in figure 4.8. Elasticity contact theory assumed that the contact half-width increase continuously with the load P ; however in our simulation the contact half-width grows in jumps as new atoms become in contact with the indenter surface. We see that before dislocation the elastic continuum theory matches the stepwise atomic simulation pretty well at the early stages of the simulation, but deviates from the hertzian solution with increased loads.

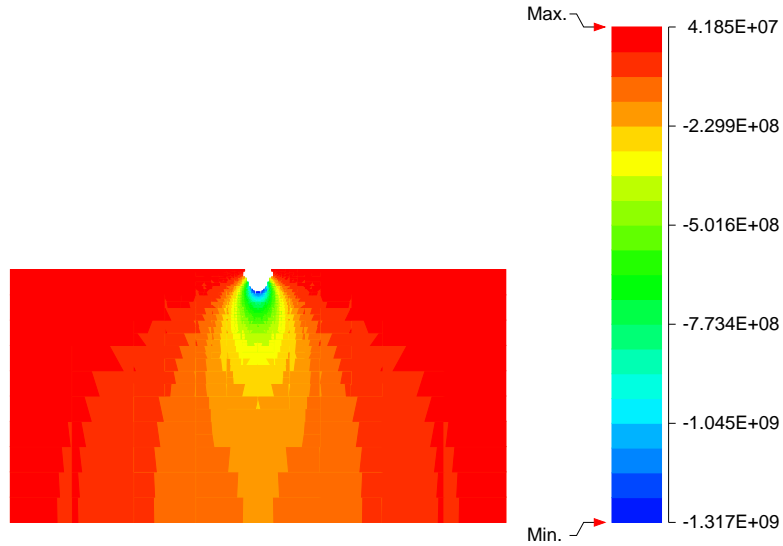


Figure 4.6: Stress T_{yy} (in Pa) just before first dislocation for nanoindentation problem in figure 4.2

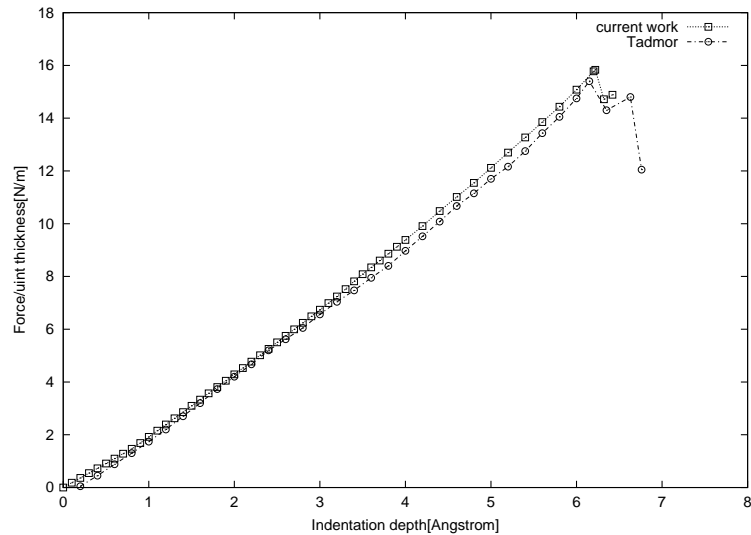


Figure 4.7: Load vs indenter displacement for nanoindentation problem in figure 4.2

4.3.3 Effect of Temperature due to Nanoindentation of a 2D Flat Indenter

To demonstrate the steps involved in the finite temperature adaptive multi-scale model, consider the problem depicted in figure 4.9. Here a rigid rectangular indenter, infinitely long in the out of plane direction, is pressed into the free surface of a single crystal aluminum along the 010 direction. The displacement in the out-of-plane direction are constrained to zero values, i.e plain strain problem. The indenter is a rigid rectangular block 257.6\AA wide.

The thin film studied in this example is 515.1\AA thick, 772.7\AA wide. This system size was chosen to ensure that the far-field boundary conditions did not affect the behavior in the vicinity

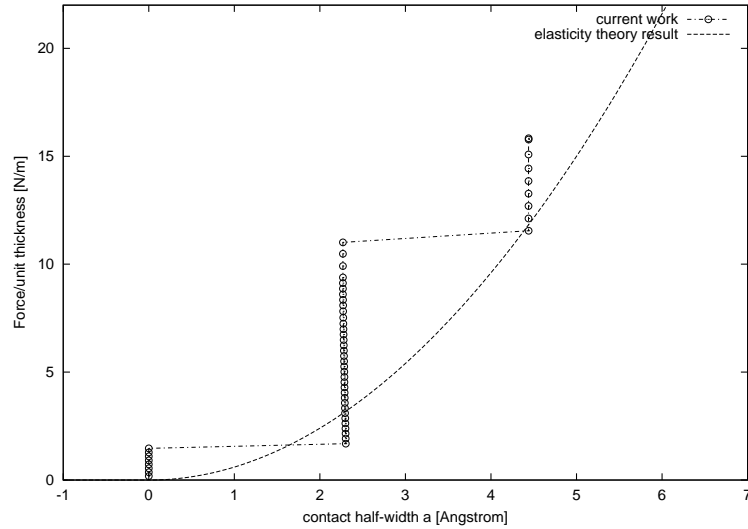


Figure 4.8: Load vs contact half-width for nanoindentation problem in figure 4.2

of the indenter. Increasing system size did not change the results. The system investigated here is very large by current direct atomistic modeling. A direct atomistic modeling would require 300, 000 atoms or 900, 000 degrees of freedom. By using the quasicontinuum method the computational cost is greatly reduced. In current simulation, only 2, 080 nodes+atoms are explicitly treated (4,160 degrees of freedom) in the analysis.

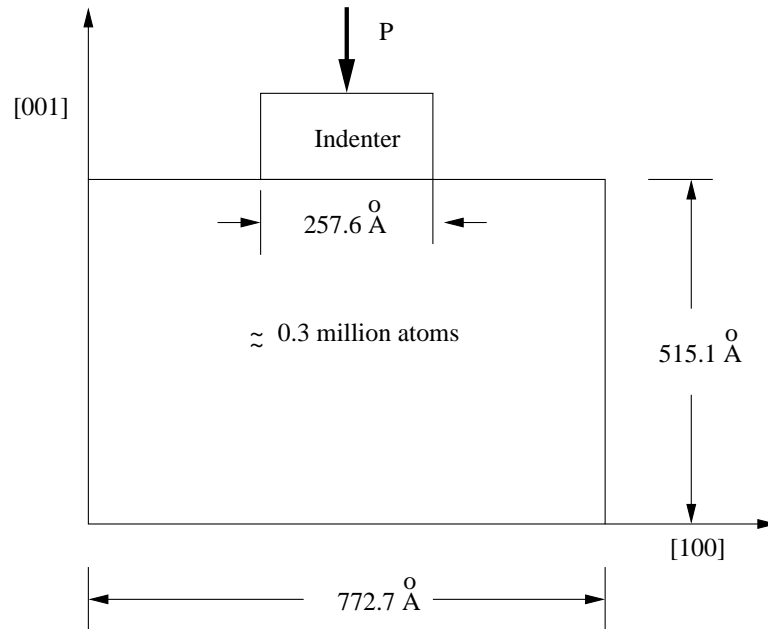


Figure 4.9: Nanoindentation in an aluminum single crystal

The adaptive refining algorithm discussed previously was used in this example. Specifically, any element with strain energy err density larger than 1% of the average system strain energy is selceted to be refined to next level. In this example, the elements on initial mesh(level 0) have

dimension of $32a \times 32a$, where a is the lattice parameter for aluminum. Continuum elements could exist as high as 6th level. A element at 6th level, having dimension of $a \times a$ will be opened into atoms if needed. A series of the progressive mesh refinements for this problem are given in figure (4.10). The QC model has 35 nodes in initial mesh. At final stage (1st dislocation) the QC model only includes 1, 068 atoms plus 1012 nodes. We assume that the atoms in contact with the indenter cannot slip out from under the indenter (the atoms right under the indenter experience very little x-direction movement).

The atomic structures under indenter at different temperature(0 K, 293 K, 373 K) are given in figure(4.11, 4.12, 4.13). The load-displacement curve obtained from the simulation is in figure 4.14. The results were performed with displacement control and thus the figure represents the load required to hold the indenter at a given indentation depth. At each load step, the indentation depth is increased by 0.3 Å. Loads are given in Newtons per meter length of the indenter in the out-of-plane direction.

For 0 K temperature, the resulting response of the material is almost linear as predicted by elasticity theory till the formation of defects at the atomistic scale. Toward the end of the loading cycle these defect cause a flat shift in the load-displacement curve. This in turn is reflected by the fact that the corner atom under the indenter requires no contact force. From this deformed configuration shown in figure 4.11, the corner atoms under the indenter are expected to move into the defect under the indenter resulting in the formation of the 1st dislocation in the material. The first dislocation is emitted at the indentation depth of 27.7 Å. At the initial stage,i.e. till depth equal to 5.0 angstroms, the responses of 293 K and 373 K are almost the same to 0 K. Passing that point, both cases show somewhat nonlinear properties. However, the critical loads for emission are close to each other. We may conclude that the temperature effect on first dislocation is small when the temperature is moderate. The 1st Piola-Kirchhoff stress (T_{yy}) distribution, at 373K during the formation of the 1st dislocation is shown in figure 4.15.

4.3.4 Nanoindentation with a Spherical Indenter

In this 3D example, a rigid indenter($R=4700$ Å) is driven into a thin single crystal aluminum along the 001 direction. The dimensions of the material specimen, schematically shown in figure 4.16, is $0.829 \mu m \times 0.829 \mu m \times 0.415 \mu m$. The bottom surface of the cell rests on a rigid half space, with traction-free surfaces. The contact algorithm discussed previously is used to model the spherical indenter. The size of the indenter is from the experiment of [97]. The cell contains around 1.7×10^{10} atoms.

The initial uniform mesh is $16 \times 16 \times 8$ with 2601 nodes. The elements on initial mesh(level 0) have dimension of $128a \times 128a \times 128a$, where a is the lattice parameter for aluminum. The adaptive refinement algorithm automatically delineate the region of severe deformation upto 7 levels of continuum elements and into atoms at the 8th level. Strain energy error was taken as error estimator to decide what elements to be refined. Specifically, any element with strain energy err density larger than 1% of the average system strain energy is selcted to be refined to next level. Varied step sizes were taken in this simulation. At the early stage, the indenter is pushed down 10 Å each step. Near to the critical load, the step load low down to 0.5Å. At a indentation depth of 210.5 Å, the model includes 78, 000 nodes+atoms. The mesh at depth of 210.5 Å

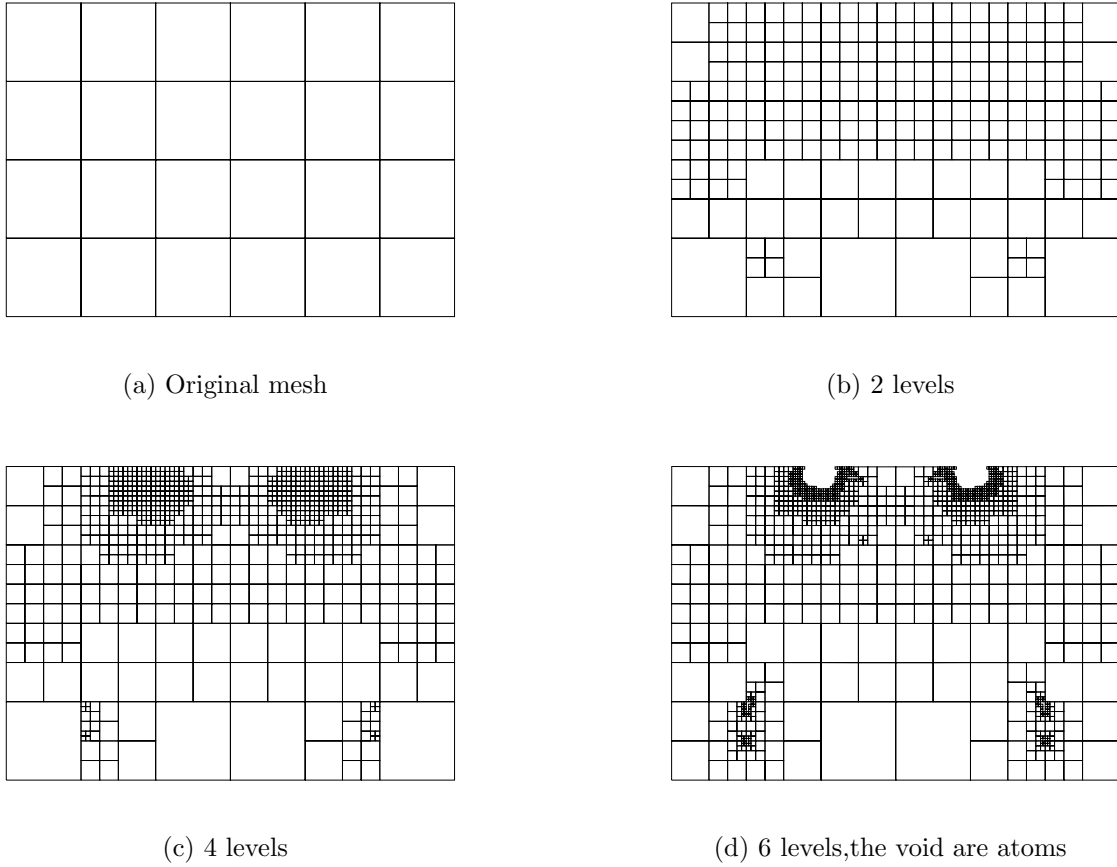


Figure 4.10: Automatic multi-scale mesh refinement generated for nanoindentation problem in figure 4.9

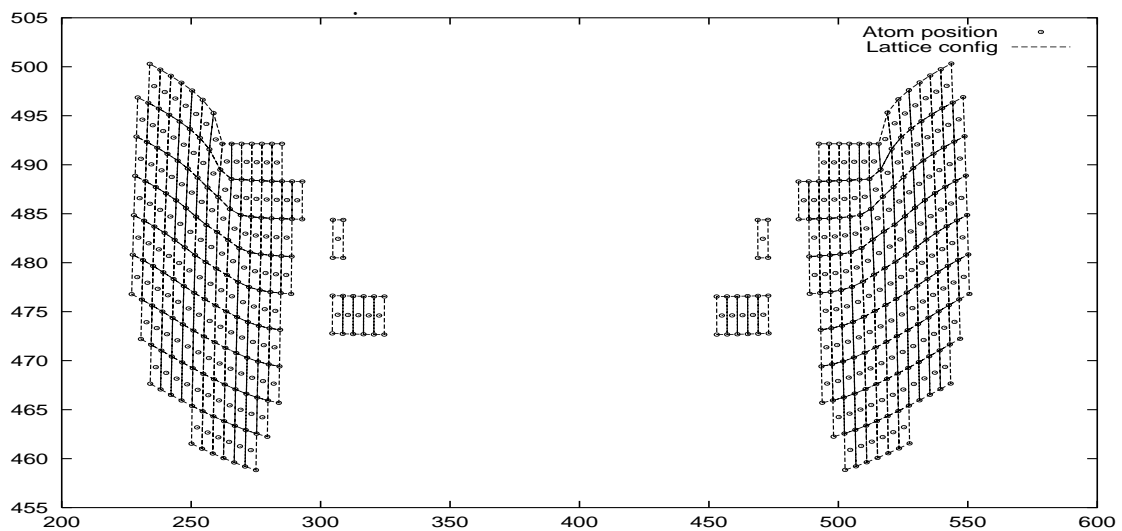


Figure 4.11: Atomic structure under indenter, just before nucleation of first defect, for nanoindentation problem (temperature: 0 K) in figure 4.9

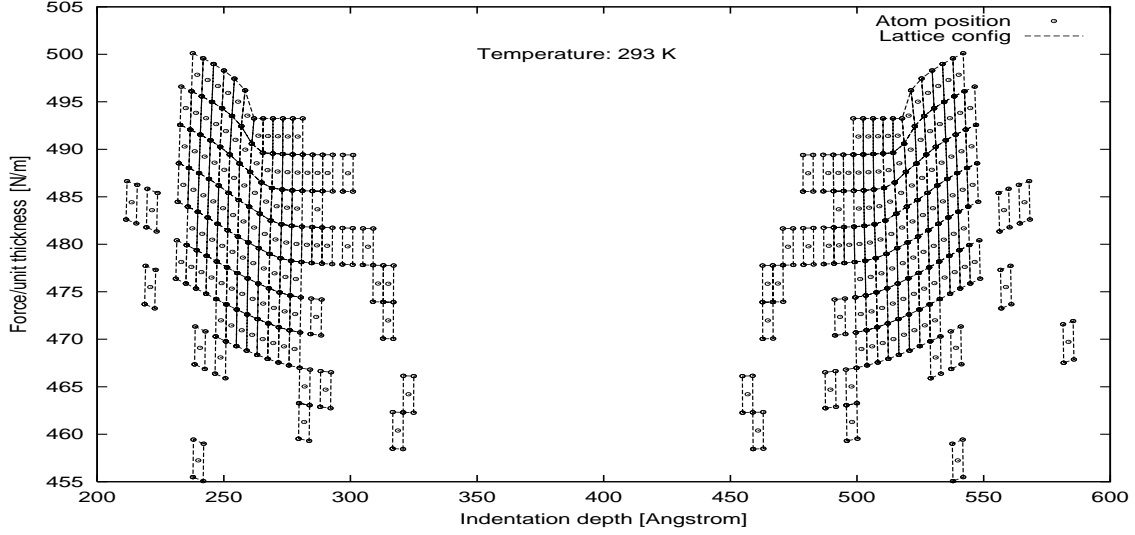


Figure 4.12: Atomic structure under indenter, just before nucleation of first defect, for nanoindentation problem (temperature: 293 K) in figure 4.9

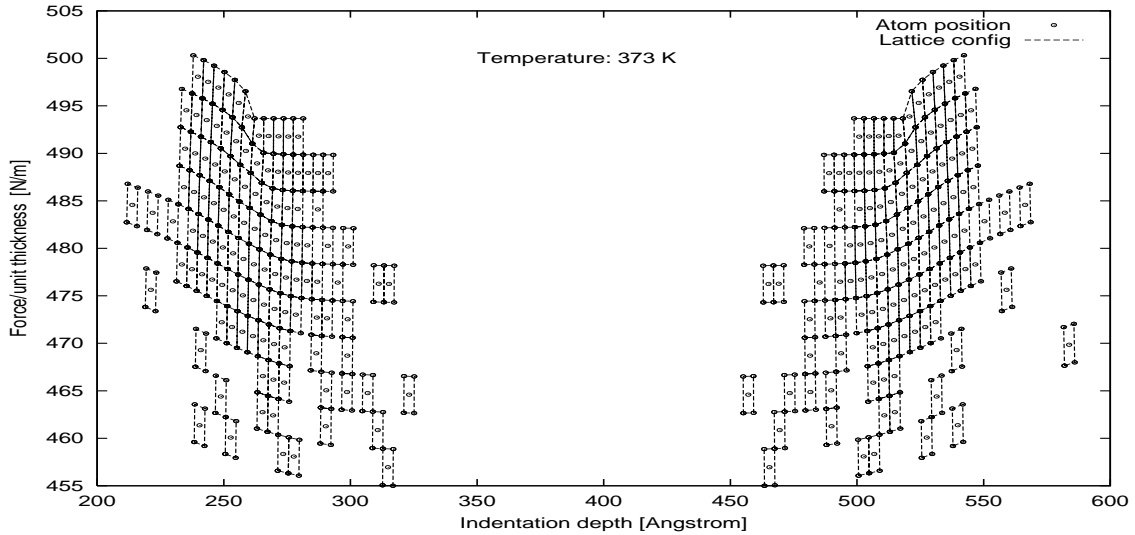


Figure 4.13: Atomic structure under indenter, just before nucleation of first defect, for nanoindentation problem (temperature: 373 K) in figure 4.9

is given by figure 4.17. Note that the refinement mainly focus on the edge of the contact surface.

The 1st Piola-Kirchhoff stress (T_{zz}) is presented in figure 4.18. The computed force vs displacement indentation is plotted in figure 4.19. For spherical indenter, Hertz contact theory provides the relationship between indentation load P and the indentation depth δ [38],

$$\delta = \left(\frac{9P^2}{16RE^*2} \right)^{1/3} \quad (4.18)$$

Substituting equ. 4.16 into equ. 4.18, we have,

$$P = \frac{8\mu\delta^{3/2}\sqrt{R}}{3(1-\nu)} \quad (4.19)$$

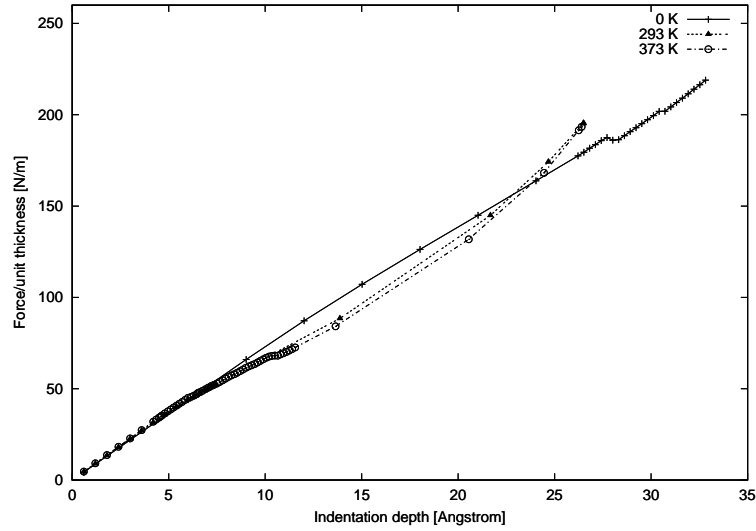


Figure 4.14: Load vs indenter displacement at different temperature for nanoindentation problem in figure 4.9

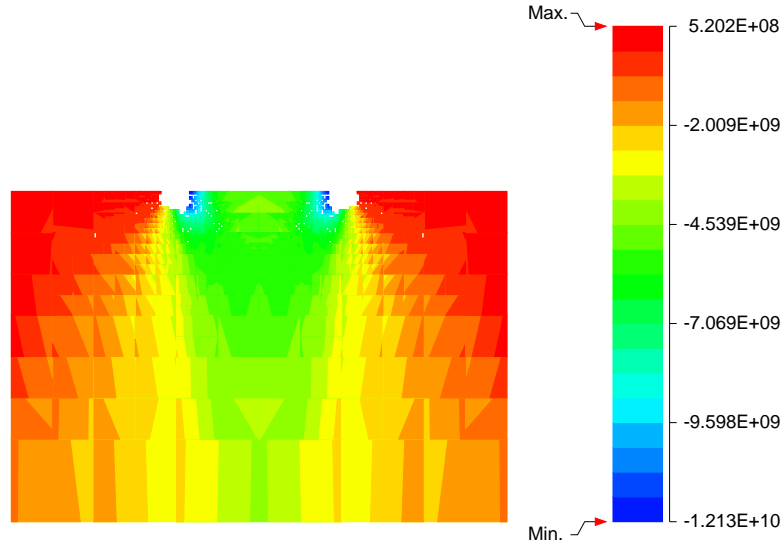


Figure 4.15: Stress T_{yy} (in Pa) just before first dislocation for nanoindentation problem in figure 4.9 at $T = 373K$

Substituting in the corresponding values we got previously (i.e. $\mu = 29.41\text{GPa}$, $\nu = 0.334$, and $R = 4700.0\text{\AA}$) yields $P = 0.08073\delta^{3/2}$ with P in μN and δ in \AA .

At the indentation depth of 210.5\AA , the force P is $3.02 \times 10^{-4}\text{N}$. The hardness is $P/A = 9.20\text{GPa}$ (elasticity theory predicts the hardness as $P/A = 7.93\text{GPa}$), which differs from the experimental value [97] 0.81GPa . This may be contributed to the fact that no dislocation has been generated yet. In order to model the problem into generation of the 1st dislocation, it is estimated that the current computational model would require ≈ 2 million degrees of freedom. Such a huge system would require parallelization of the computational algorithm which is currently being pursued by the computational group.

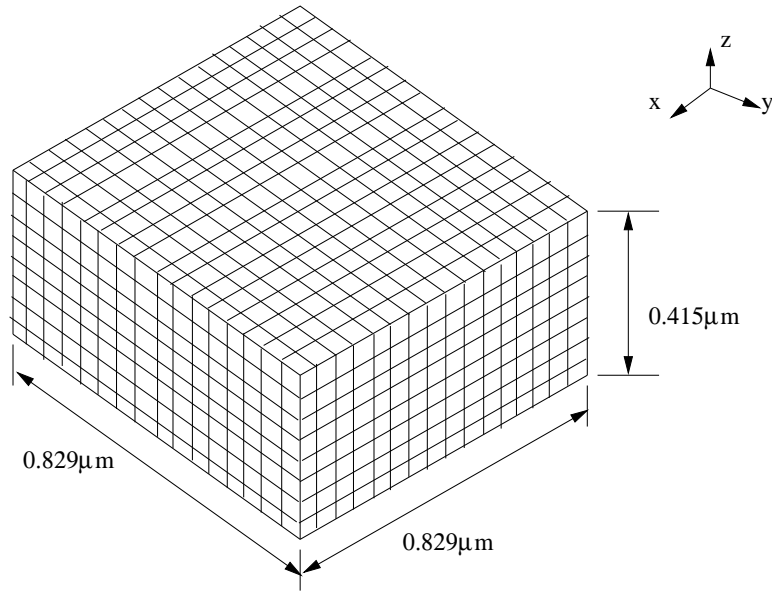


Figure 4.16: Geometry of the computational cell and initial mesh

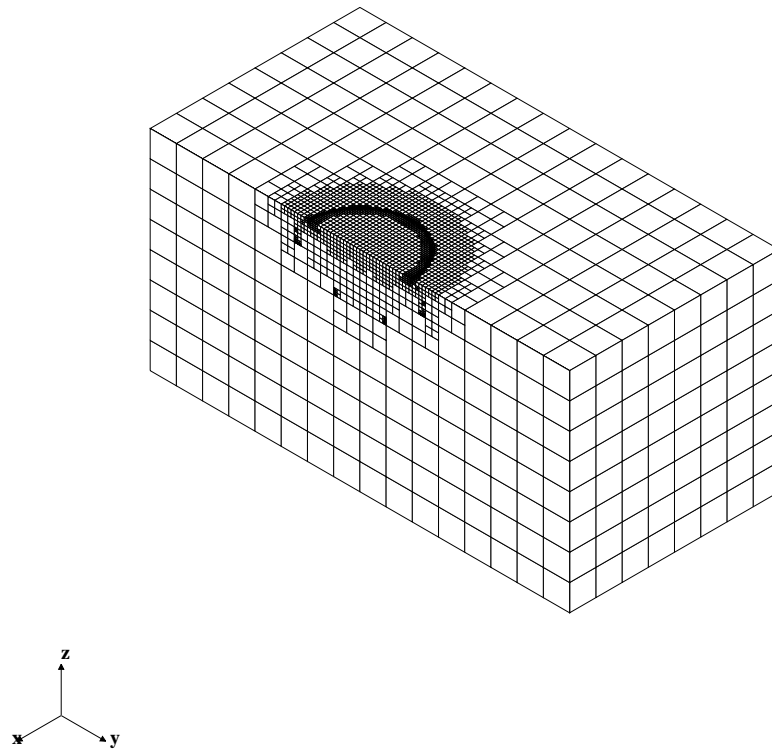


Figure 4.17: Cross section of the computational mesh at an indentation depth of 210.5 \AA

To conclude, these examples demonstrate the efficiency and accuracy of the adaptive multi-scale model for generating incipient plasticity in nanocomposites. The main conclusions of this dissertation and possible utility of the model are discussed briefly in the next chapter.

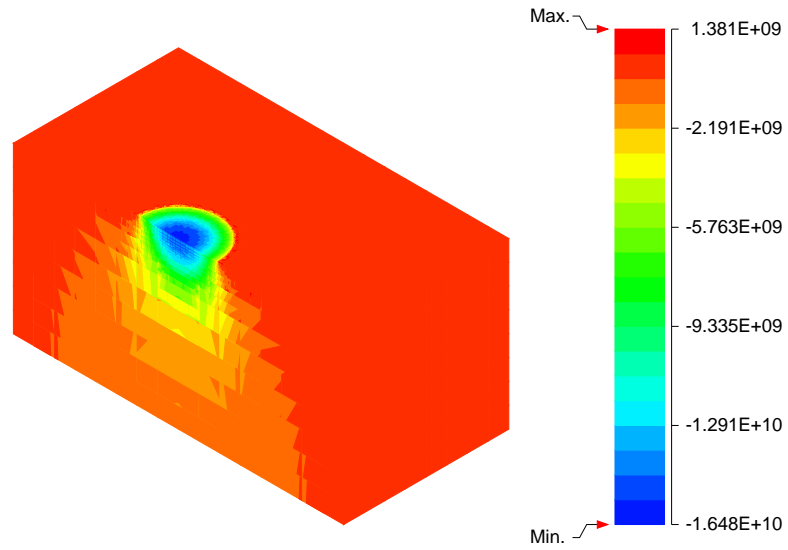


Figure 4.18: Stress T_{zz} (in Pa) at an indentation depth of 210.5 Å

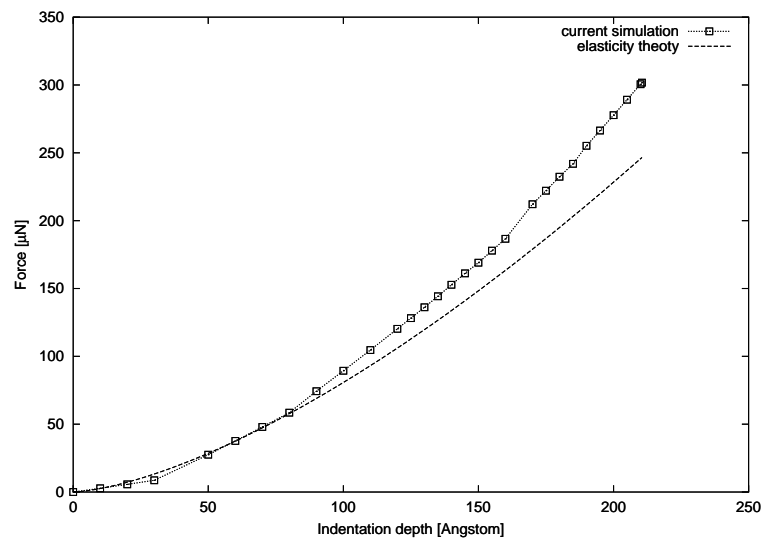


Figure 4.19: Force vs displacement curve for the 4700 Å-radius indenter

Chapter 5

Conclusions and Future Work

In this thesis an adaptive multiscale computational model is used to simulate incipient plasticity in nanoscale materials at finite temperatures. Numerical examples to demonstrate the applicability of the method for $2D$ and $3D$ nanoindentation problems are presented. The computational model uses a continuum scale description of the deformation in regions of smooth deformation and an atomistic scale description in regions where a dislocation is being generated. A major advantage of the hierarchical adaptive scheme is that it can *automatically* delineate the two-scales of analysis without any user interference. This completely avoids cumbersome remeshing techniques used in some of the state of art simulations. The underlying physics of the problem, at both continuum and atomistic scales, is generated through interatomic potentials at finite temperatures using a local harmonic approximation. This approximation provides an efficient framework for the analysis of material phenomena without having to employ expensive MD simulations to capture dynamic atomic vibration. Thus the adaptive nature of the model, when coupled with finite temperature effects, provides a computational efficient and accurate method to study plasticity in nanoscale materials at practical time/length scales.

Future applications for the current method are expected to include

- The adaptive computational methodology developed in this thesis can provide an effective framework for analysis of a large number of physical phenomena in which material behavior is characterized by deformation/processes localized over sub-regions of the domain.
- At the microscale such processes could include (a) material design of polycrystalline materials (b) two-scale analysis of composite structures with underlying heterogeneities or (c) manufacturing processes such as solidification used to prepare such composites.
- At the nanoscale, such phenomena are vital in the characterization of plastic deformation processes, which in turn are an important aspect for targeted design of these materials. These could possibly include modeling hardness and toughness experiments for nanocomposites composed of a mixture of dissimilar materials which individually provide specific property enhancements
- The current capabilities have been implemented using in house model development in a single PC processor environment. When the current $3D$ capabilities are exported to parallel processor environment they should be able to greatly assist in the realistic material design of realistic material/structural systems.

Bibliography

- [1] **Abraham, F.F., Schneider, D., Land, B., Lifka, D., Skovia, J., Gerner, J., Rosenkrantz, M.**, 1998. Instability dynamics in three-dimensional fracture: an atomistic simulation. *Journal of Mechanics and Physics of Solids*, **45**, 1461-1471.
- [2] **Abraham, F.F., Walkup, R., Gao, H.J., Duchaineau, M., De la Rubia, T.D., Seager, M.**, 2002. Simulating materials failure by using up to one billion atoms and the world's faster computer: brittle fracture. *Proc. Natl. Acad. Sci. USA*, **99**, 5777-5782.
- [3] **Ainsworth, M., Oden, J.T.**, 1992. A procedure for a posteriori error estimation h-p finite element methods. *Comp. Meth. App. Mech. Engrg.*, **101**, 73-96.
- [4] **Antunes, J.M., Menesez, L.F., Fernandes, J.V.**, 2006. Three-dimensional numerical simulation of Vickers indentation tests. *International Journal of Solids and Structures*, **43**, 784-806.
- [5] **Asaro, R.**, 1983. Micromechanics of crystals and polycrystals. *Advances in Applied Mechanics*, **23**1115,
- [6] **Babuska, I., Melenk, J.M.**, 1996. The partition of unity finite element method: Basic theory and applications. Research report no. 96-01, Seminar for Angewandte Mathematik, Zurich, Switzerland.
- [7] **Bahr, D.F., Kramer, D.E., Gerberich, W.W.**, 1998. Non-linear deformation mechanisms during nanoindentation. *Acta Mater.*, **46**, 3605-3617.
- [8] **Baskes, M., Johnson, R.A.**, 1994. A Modified embedded atom potential for hcp metals. *Model. Simul. Mat. Sci. Engrg.*, **2**, 147-163.
- [9] **Banerjee, S., Ghoniem, N., Lu, G., Kioussis, N.**, 2005. A Hybrid Atomistic-Continuum Model for the Core Structure of Curved Dislocations, to appear in *Modeling and Simulat. in Mat. Sci. and Eng.*
- [10] **Bank, R.E., Widser, A.**, 1985. Some a posteriori error estimators for elliptic partial differential equations. *Math. Comput.*, **44**, 283-301
- [11] **Belytschko, T., Tbbara, M.**, 1993. H-adaptive finite element methods for dynamic problems, with emphasis on localization. *International Journal of Numerical Methods in Engineering*, **36**, 4245-4265.

- [12] **Bolshakov, A., Pharr, G. M.,** 1998. Influences of Pile-up on the Measurement of Mechanical Properties by Load and Depth Sensing Indentation Techniques. *Journal of Materials Research*. **13**, 1049-1058.
- [13] **Born, M., Huang, K.,** 1954. *Dynamical Theory of the Crystal Lattices*. Oxford University Press, Oxford.
- [14] **Broughton, J.Q., Abraham, F.F., Bernstein, N., Kaxiras, E.,** 1999. Concurrent coupling of length scales: methodology and application. *Physical Review B*, **60**(4), 2391-2403.
- [15] **Cai, W., de Koning, M., Bulatov, V.V., Yip, S.,** 2000. Minimizing boundary reflections in coupled-domain simulations. *Physical Review Letters*, **85**3213-3216.
- [16] **Chandler, D.,** 1987. *Introduction to Modern Statistical Mechanics*, Oxford University Press, Oxford.
- [17] **Curtarolo, S., Ceder, G.,** 2002. Dynamics of an inhomogeneously coarse grained multiscale system. *Physical Review Letters*, **88** 255504.
- [18] **Curtin, W.A., Miller, R.E.,** 2003. Atomistic/continuum coupling in computational materials science. *Modeling Simul. Mater. Sci. Eng.* **11**, R33-R68.
- [19] **Daw, M.S., Baskes, M.I.,** 1984. Embedded-atom method: derivation and application to impurities, surfaces, and other defects in metals. *Physical Review B*, **29**, 6443-53.
- [20] **Daw, M.S., Foiles, M.S., Baskes, M.I.,** 1993. The embedded-atom method: a review of theory and application. *Matter. Sci. Rep.*, **9**, 251-310.
- [21] **Dennis, J.E., More, J.J.,** 1977. Quasi-Newton methods, motivation and theory. *SIAM Review*, **19**, No.1, 46-89
- [22] **Devloo, P., Oden, J.T., Strouboulis, T.,** 1986. Implementation of an adaptive refinement technique for the SUPG algorithm. *Computer Methods in Applied Mechanics and Engineering*, **61**, 339-358.
- [23] **Diestler, D.J., Wu, Z.B., Zeng, X.C. ,** 2004. An extension of the quasicontinuum treatment of multiscale solid systems to nonzero temperature. *Journal of Chemical Physics*. **121**, 9279-9282.
- [24] **Dove, M.T.,** 1993. *Introduction to lattice dynamics*, Cambridge University Press, London.
- [25] **Dupuy, L.M., Tadmor, E.B., Miller, R.E., Philips, R.,** 2005. Finite-temperature quasicontinuum: molecular dynamics without all the atoms. *Physical Review Letters*, **95**, 060202-1-060202-4.
- [26] **E, W., Huang, Z.,** 2001. Matching conditions in atomistic-continuum modeling of materials. *Physical Review Letters*, **87**, 135501-1-135501-4.

- [27] **Ercolessi, F., Adams, J.**, 1993. Interatomic potentials from 1st-principles calculations-the force-matching method. *Europhysics Letters*, **26**, 583-588.
- [28] **Faber, V., Manteuffel, T.**, 1984. Necessary and Sufficient Conditions for the Existence of a Conjugate Gradient Method. *SIAM J. Numer. Anal.* **21**, 315-339.
- [29] **Fischer-Cripps, A.C.**, 2002. *Nanoindentation*. Springer-Verlag, New York.
- [30] **Foiles, S.M.**, 1994. Evaluation of harmonic methods for calculating the free energy of defects in solids. *Physical Review B*, **49**, 14930-14938.
- [31] **Ghoniem, N.M., Busso, E.B., Kioussis, N., Huang, H.** 2003. Multiscale modeling of nanomechanics and micromechanics:an overview. *Philosophical Magazine A*, **83**, 3475-3528.
- [32] **Gratsch, T., Bathe, K-J.**, 2004. A posteriori error estimation techniques in practical finite element analysis (in press)
- [33] **Hernot, X., Bartier, O., Bekouche, Y., Abdi, R.E., Mauvoisin, G.**, 2006. Influence of penetration depth and mechanical properties on contact radius determination for spherical indentation. *International Journal of Solids and Structures*.**43**, 4136-4153.
- [34] **Hirth, J. P.**, 1992, *Theory of Dislocations*. 2nd edition, Krieger, Malabar, Florida.
- [35] **Hughes, T.J.R.**, 1987. *The Finite Element Method : Linear Static and Dynamic Finite Element Analysis*. Prentice-Hall, Englewood Cliffs, New Jersey.
- [36] **Jarusch, K.F., Kiely, J.D., Houston, J.E., Russell, P.E.**, 2000. Defect-dependent elasticity:nanoindentation as a probe of stress state. *Journal of Materials Research*.**15**, 1693-1701.
- [37] **Jiang, H., Huang, Y., Hwang, K.C.**, 2005. A finite-temperature continuum theory based on interatomic potentials. *Transaction of the ASME*, **127**, 408-416.
- [38] **Johnson, K.L.**, 1985, *Contact Mechanics*, Cambridge University Press, New York.
- [39] **Jones, J.E.**, 1924. On the determination of molecular fields.I. from the variation of the viscosity of a gas with temperature. *Proc. Roy Soc. A*, **106**, 441-462.
- [40] **Li, J., van Vliet, K.J., Zhu, T., Yip, S., Suresh, S.** 2002. Atomistic mechanisms governing elastic limit and incipient plasticity in crystals. *Letters to Nature*, **418**, 307-310.
- [41] **Kachakov, M.**, 1992. Effective elastic properties of cracked solids:critical review of some basic concepts. *Appl. Mech. Rev.*, **45**, 304
- [42] **Kelchner, C.L., Plimpton, S.J., Hamilton, J.C.**, 1998. Dislocation nucleation and defect structure during surface indentation. *Physical review B*, **58**, 11085-11088.
- [43] **Kiely, J.D., Hwang, R.Q., Houston, J.E.**, 1998. Effect of surface steps on the plastic threshold in nanoindentation. *Physical Review Letters*, **164424-4427**.

- [44] **Knap, J., Ortiz, M.**, 2001. An analysis of the quasicontinuum method. *Journal of Mechanics and Physics of Solids*, **49**, 1899-1923.
- [45] **Knap, J., Ortiz, M.**, 2003. Effect of indenter-radius size on Au(001) nanoindentation. *Physical Review Letters*, **90**226102-1.
- [46] **Kohlhoff, S., Cumbach, P., Fscschmeister, H.F.**, 1991. Crack propagation in bcc crystal studied with a combined finite-element and atomistic model. *Philosophical Magazine A*, **64**, 851-878.
- [47] **Qian, D., Wagner, D.J., Liu, W.K.**, 2004 A multiscale projection method for the analysis of acarbon nanotubes. *Computer Methods in Applied Mechanics and Engineering*, **193**.
- [48] **Landman, U., Uedtke, W.D., Nancy, A., Burnham, A., Colton, R.J.**, 1990. Atomistic mechanisms and dynamics of adhesion, nanoindentation, and fracture. *Science*, **248**, 454.
- [49] **LeSar, R., Najafabadi, N., Srolovitz, D.J.**, 1989. Finite-temperature defect properties form free-energy minimization. *Physical Review Letters*, **63**, 624-627.
- [50] **Li, Y.B., Wei, B.Q., Xu, C.L., Liang, J., Wu, D.H.** 1999. Physical properties of Fe80P20 glass-carbon nanotubes composite. *J. Mater. Sci.* **34**, 5281-5284.
- [51] **Lichinchi, M., Lenardi, C., Haupt, J., Vitali, R.**, 1998. Simulation of Berkovich nanoindentation experiments on thin films using finite element method. *Thin Solid Filem*, **333**, 278-286.
- [52] **Liu, B., Huang, Y., Jiang, H., Qu, S., Hwang, K.C.**, 2004. The atomic-scale finite element method. *Computer Methods in Applied Mechanics and Engineering*, **193**, 1849-1846.
- [53] **Liu, W.K., Karpov, E.G., Zhang S., Park, H.S.**, 2004. An introduction to computational nanomechanics and materials. *Computer Methods in Applied Mechanics and Engineering*, **193**, 1849-1846.
- [54] **Lidorikis, E., Bachlechner, M.E., Kalia, R.K., Vashishta, P., Nakano, A., Voyiadjis, G.Z.**, 2001. Coupling Length Scales for Multiscale Atomistic-Continuum Simulations: Atomistically Induced Stress Distributions in Si/Si3N4 Nanopixels. *Physical Review Letters*, **87**, 086104-1-086104-4.
- [55] **Ma, Q., Clarke, D.R.** , 1995. Size dependent hardness of silver single crystals. *Journal of Materials Research*, **10**, 853-863.
- [56] **Matthies, H., Strang, G.**, 1979. The solution of nonlinear finite element equations. *International Journal of Numerical Methods in Engineering*, **14**, 1613-1626.
- [57] **Malvern, L.E.**, 1969. *Introduction to the Mechanics of a Continuous Medium*. Prentice-Hall, Englewood Cliffs, New Jersey.

- [58] **McElhaney, K.W., Vlassak, J.J., Nix, W.D.,** 1998. Determination of indenter tip geometry and indentation contact area for depth-sensing indentation experiments. *Journal of Materials Research*.**13**, 1300-1306.
- [59] **Meng W.J., Tittsworth R.C., Rehn L.E.,** 2000. Mechanical properties and microstructure of TiC/amorphous hydrocarbon nanocomposite coatings. *Thin Solid Films*, **377**, 222-234.
- [60] **Michalske, T.A., Houston, J.E.,** 1998. Dislocation nucleation at nano-scale mechanical contacts. *Acta Mater.*, **46**, 391-396.
- [61] **Milstein, F.,** 1980. Review: theoretical elastic behavior at large strains. *J. of Mater. Sci.*, **15**, 1071-1084.
- [62] **Mishin, Y., Farkas, D., Mehl, D.J., Papaconstantopoulos, D.A.,** 1999. Interatomic potentials for monoatomic metals from experimental data and *ab initio* calculations. *Phys. Rev. B*, **59**, 3393-3407.
- [63] **Miller, R.E., Tadmor, E.B., Ortiz, M.,** 1998. Quasicontinuum simulation of fracture at atomic scale. *Modeling Simul. Mater. Sci. Eng.* **6**, 607-638.
- [64] **Miller, R.E., Tadmor, E.B.,** 2002. The Quasicontinuum method: overview, applications and current directions. *Journal of Computer – Aided Materials Design* **9**, 203-239.
- [65] **Miller, R.E., Shilkrot, L.E., Curtin, W.,** 2004. A coupled atomistics and discrete dislocation plasticity simulation of nanoindentation into single crystal thin films. *Acta Materialia*, **52**, 271-284.
- [66] **Najafabadi, R., Srolovitz, D.J.,** 1995. Evaluation of the accuracy of the free-energy-minimization method. *Physical review B*, **52**, 9229-9241.
- [67] **Nakano, A., Martina, E.B., Kalia, R., Lidorikis, E., Vashishta, P., Voyiadjis, G.Z.,** 2001. Multiscale simulation of nanosystems. *Computing in Science & Engineering*, **July/August**, 56-66.
- [68] **Nix, W.D., Gao, H.,** 1998. Indentation size effects in crystalline materials: a law for strain gradient plasticity. *Journal of Mechanics and Physics of Solids*, **46**, 411-425.
- [69] **Oliver, W.C., Pharr, G.M.,** 1992. An improved technique for determining hardness and elastic modulus using load and displacement sensing indentation experiments. *Journal of Materials Research*, **7**, 1564-1583.
- [70] **Papadopoulos, P., Taylor, R.,** 1992. A mixed formulation for the finite element solution of contact problems. *Computer Method in Applied Mechanics and Engineering* , **94**, 373-389.
- [71] **Pharr, G.M.,** 1998. Measurement of mechanical properties by ultra-low load indentation. *Materials Science and Engineering*, **A235**, 151-159.
- [72] **Picu P.C.,** 2000. Atomistic-continuum simulation of nanoindentation in molybdenum. *J. Comp – Aided Mater. Des.* **7**, 77-87.

- [73] **Polonsky, A., Chang, T.P., Keer, L.M., Sproul, W.D.,** 1998. A study of rolling coating fatigue of bearing steel coated with physical vapor deposition of TiN films, *Wear*, **215**, 191-203
- [74] **Prasanna R., Moorthy S., Ghosh S. and Pagano N.J.,** 2001. Revisiting the Composite Laminate Problem with an Adaptive Multi-Level Computational Scheme, *Composite Science and Technology*, **61**, 1017-1040.
- [75] **Prudhomme, S., Nobile, F., Oden, J.T.,** 2002. Analysis of subdomain-based error estimator for finite element approximations of elliptic problems. TICAM report 02-34, The University of Texas at Austin. To appear in *Numer. Meth. Part D&E*.
- [76] **Rapaport, D.C.,** 1995. *The Art of Molecular Dynamics*. Cambridge university press, New York
- [77] **Rodney, D., Philips, R.,** 1999. Structure and strength of dislocation junctions:an atomic level analysis. *Physical Review Letters*, **82**, 1704-7.
- [78] **Shehadeh, M., Banerjee, S., Lu, G., Kioussis, N., Ghoniem, N.,** 2005. Multiscale Modeling of Dislocation Core Properties of Interfaces, to be submitted to *Phys. Rev. B*.
- [79] **Shenoy, V.B., Miller, R., Tadmor, E.B., Rodney, D., Philips, R., Ortiz, M.,** 1999. An adaptive finite element approach to atomistic-scale mechanics-the quasicontinuum method. *J. Mech. Phys.Solids*, **47**, 611-642.
- [80] **Shenoy, V.B., Miller, R., Tadmor, E.B., Rodney, D., Philips, R., Ortiz, M.,** 1998. Quasicontinuum models of interfacial structure and deformation. *Physical Review Letters*, **80**, 742-745.
- [81] **Shenoy, V.B., Philips, R., Tadmor, E.B., Rodney, D., Ortiz, M.,** 2000. Nucleation of dislocation beneath a plane strain indenter. *J. Mech. Phys. Solids*, **48**, 649-673.
- [82] **Shenoy, V., Shenoy, V., Philips, R.,** 1999. Finite temperature quasicontinuum methods. *Mat. Res. Sec. Symp. Proc.*, **538**, 465-471.
- [83] **Shilkrot, L.E., Curtin, W.A., Miller, R.E.,** 2002. A coupled atomistic/continuum model of defects in solids. *Journal of Mechanics and Physics of Solids*, **50**, 2085-2106.
- [84] **Shilkrot, L.E., Miller, R.E., Curtin, W.A.,** 2002. Coupled atomistic and discrete dislocation plasticity. *Physical review letters*, **89**, 025501-1-025501-4.
- [85] **Shilkrot, L.E., Miller, R.E., Curtin, W.A.,** 2004. Multiscale plasticity modeling: coupled atomistic and discrete dislocation mechanics. *Journal of Mechanics and Physics of Solids*, **52**, 755-787.
- [86] **Soifer, Y.M., Verdyan, A., Kazakevich, M., Rabkin, E.,** 2005. Edge effect during nanoindentation of thin copper films. *Materials Letters*.**59**, 1434-1438.
- [87] **Simo, J.C., Wriggers, P., Taylor, R.T.,** 1985. A perturbed Lagrangian formulation for the finite element solution of contact problems. *Computer Method in Applied Mechanics and Engineering* , **50**, 163-180.

- [88] **Stillinger F.H., Weber T.A.**, 1985. Computer simulation of local order in condensed phases of silicon. *Phys. Rev. B*, **31**, 5262-5271
- [89] **Tadmor, E.B.**, 1996. *The Quasicontinuum Method*. Ph.D. Thesis, Brown University.
- [90] **Tadmor, E.B., Ortiz, M., Philips, R.**, 1996. Quasicontinuum analysis of defects in solids. *Philosophical Magazine A*, **73**, 1529-1563.
- [91] **Tadmor, E.B., Philips, R.**, 1996. Mixed atomistic and continuum models of deformation in solids. *Langmuir*, **12**, 4529-4543.
- [92] **Tadmor, E.B., Miller, R., Philips, R., Ortiz, M.**, 1999. Nanoindentation and incipient plasticity. *J. Matter. Res.*, **14**, 2233-2250.
- [93] **Taig, I.C.**, 1961. Structural analysis by the matrix displacement method. *Report S017*, English Electric Aviation Report, England.
- [94] **Truesdell. C., Noll, W.**, , *Nonlinear field theories* in *Handbuch der Physik* (ed. S.Flügge), Springer-Verlag, Berlin (1965)
- [95] **Toupin, R.A.**, 1962. Elastic Material with couple-stresses. *Arch. Rat. Mech. Anal.*, **11**, 385.
- [96] **Truesdell, C., Toupin, T.A.**, 1960. The classical field theories. In encyclopedia of physics, edited S. Fluegge, Vol III/1, Springer-Verlag, Berlin, Germany.
- [97] **Tymiak, N.I., Keamer, D.E., Bahr, D.F., Wyrobek, T.J., Gergerich, W.W.**, 2001. Plastic strain and strain gradient at very small indentatio depths. *Acta Mater.***49**, 1021-034.
- [98] **Vadalakonda, S., Banerjee, R., Puthcode, A., Mirshams, R.**, 2006. Comparison of incipient plasticity in bcc and fcc metals studied using nanoindentation. *Materials Science and Engineering A*, **426**, 208-213.
- [99] **Wagner, G.J., Liu, W.K.**, 2003. Coupling of atomistic and continuum simulations using a bridging scale decomposition. *J. Computat. Phys.*, **190**, 249-274.
- [100] **Weiner, J.H.**, 1983. *Statistic Mechanics of Elasticity*. Wiley, New York.
- [101] **Zhang, Q., Cagin, T., van Duin, A., William, A.G.**, 2004. Adhesion and nonwetting-wetting transition in the $Al\alpha - Al_2O_3$ interface. *Physical Review B*, **69**, 1-11.
- [102] **Zhang, Q., Qi, Y., Hector, L.G., Cajin, T., William, A.G.**, 2005. Atomic simulations of kinetic friction and its velocity dependence at $Al\alpha - Al_2O_3$ interfaces. *Physical Review B*, **72**, 91-102.
- [103] **Zhou, L., Nanafabadi, R., Srolovitz, D.J.**, 1993. Finite temperature vacancy formation thermodynamics: local harmonic and quasiharmonic studies. *Modeling Simul. Sci. Eng.*, **1**, 539-551.

- [104] **Zhou, S.J., Beazley, D.M., Lomdahl, P.S.,** 1997. Large-scale molecular dynamics simulations of three-dimensional ductile failure. *Physical Review Letters*, **78**, 479-82.
- [105] **Zhu, T., Li, J., van Vliet, K.J., Ogata, S., Yip, S., Suresh, S.,** 2004. Predictive modeling of nanoindentation-induced homogeneous dislocation nucleation in copper. *Journal of Mechanics and Physics of Solids*, **52**, 691-724.
- [106] **Zbib, H.M., Rhee, M., Hirth, J.P.,** 1998. On plastic deformation and the dynamics of 3D dislocations. *Int. J. Mech. Sci.*, **40**, 113-127.
- [107] **Zienkiewicz, O.C.** 1991. *The Finite Element Method*, 4th ed, vol1-2, McGraw-Hill, London.
- [108] **Zienkiewicz, O.C., Zhu, J.Z,** 1987. A simple error estimator and adaptive procedure for practical engineering analysis. *International Journal of Numerical Methods in Engineering*, **24**, 337-357.
- [109] **Zienkiewicz, O.C., Zhu, J.Z,** 1992. The superconvergent patch recovery and a *posteriori* error estimates. Part 1: The recovery technique. *International Journal of Numerical Methods in Engineering*, **33**, 1331-1364.
- [110] **Zimmerman, J.A., Kelchner, C.L., Klein, P.A., Hamilton, J.C., Foiles, S.M.,** 2001. Surface step effects on nanoindentation. *Physical Review Letters*, **87**, 165507.

Vita

Wenming Wang was born in Jiangxi, People's Republic of China, on October 17, 1973. Most of his childhood was spent in the mountains and fields. He entered Zhejiang University, Hangzhou, in 1991 and earned a Bachelor of Science in Civil Engineering degree four years later. He then spent three years at Tsinghua University, Beijing, completing his Master of Science in Civil Engineering degree. Upon graduation, he worked as a structural engineer at the Ninth Research and Design Institute, Shanghai. Leaving China in fall 2002 he enrolled at Louisiana State University to further his education. He is currently a candidate for the degree of Doctor of Philosophy in civil engineering with a minor in mathematics.